Plasmonic Hot-Carrier Optoelectronics

F. Pelayo García de Arquer

ICFO - The Institute of Photonic Sciences
Barcelona, 2014

Plasmonic Hot-Carrier Optoelectronics

F. Pelayo García de Arquer

under the supervision of

Professor Gerasimos Konstantatos

submitted this thesis in partial fulfillment
of the requirements for the degree of

Doctor

by the

Universitat Politècnica de Catalunya
Barcelona, 2014

To my family

Our virtues and our failings are inseparable,
like force and matter.

Nikola Tesla

Acknowledgements

This journey would not have been possible without the help of many people to whom I am thankful. First and foremost, my deepest and most sincere gratitude goes for my supervisor, Gerasimos Konstantatos. His always inspiring brilliance was a continuous motivation. His unconditional confidence, guidance and support throughout this wavy sea, provided me with the required momentum to accomplish this work. I feel honoured to have crossed-paths with you.

I am also indebted to the long list of SPNPers. I would like to thank Luis for his didactic spirit, and for having introduced me to Labview among others. Also for assistance in AFM characterization. We had fun in the E2C3 stage at the Pirinee! To María, thank you for your endless patience in supplying with materials and chemistry teaching. Xiaojie, we still keep your Great Wall posters in the lab. To Arup, his inner peace and immense wisdom, for the pleasure working with him. To Fiona and Silke, thanks for the always enriching scientific discussion and now standardized noon-lunch. I am grateful to David, Dominik (and Luis) for keeping our office a funny place. And Batman! Thank you David for proof-reading this thesis and for your 24/7 supermarket. To Dominik, I will miss the fun and our conversations, I am sure you will end up solving all the low dimensional problems!. Agustín was also a constant support and inspiration throughout this thesis. We had lots of fun when working together. I will keep really fond memories of our kick-off meetings at Foster's and of our brainstorming at the gym terrace. He also shared with me efforts in the work presented in chapter 5. To dope or not to dope, that is the question Alex! I will miss your crazy ideas. Thank you Tania for all the materials you provided, and especially for your always good mood, perspective, and support. Nicky and Yiming, I have learned a lot from you. Guillem and Alba for keeping a good ambient at the group making fun everyday work. I would also like to thank stimulating discussions with Alexander Govorov and Javier García de Abajo.

I am thankful to all the ICFOnians keeping this a bright place. The work of this thesis would certainly not have been possible without the help of NFL people (Luis Enrique,

Javi and Johann), the electronic and the mechanical workshops, especially Xavi. Carlos Dengra and Luis were an ubiquitous asset with endless patience and extreme efficacy. Jonas and Adri, it was fun sharing the corridor with you! I am also grateful to HHRR, KTT, frontdesk, purchase and travel departments.

A mis amigos de Barcelona, gracias por haber edulcorado los ratos fuera del trabajo: Carles, Francina, Igor, Laura, Pablo, Patxi, Quijano, Ricardo, Rodrigo, Sibylle, Taisuke, Valeria, the Italian crew... A Rafel y Lee entre otros, gracias por manternernos hidratados a toda costa.

El trabayu d'esta tesis non hubiera siu posible ensín el continuu sofitu de los mios pas ya de la mi gran familia: el méritu d'esti trabayu tamién ye vuesu. N'especial los mios padres y la mio tida Ysabel. Tamién a Silvia, gracies po la tu ayuda, sofitu, ya ciñu a lo ḷḷargu d'esti viaxe.

F. Pelayo García de Arquer, 19 de payares 2014, Barcelona

Contents

List of Figures

List of Tables

Acronyms and Symbols

AFM Atomic-Force-Microscopy

ALD Atomic-Layer-Deposition

D^* Detectivity

EQE External Quantum Efficiency

FF Fill-factor

FN Fowler-Nordheim

IQE Internal Quantum Efficiency

J_{sc} Short-circuit current density

J_{mpp} Current density at the maximum power point

LWIR Long-Wavelength-Infrared region of the spectrum (750-1400 nm)

MIM Metal-Insulator-Metal

MIR Mid-Infrared region of the spectrum (750-1400 nm)

MSM Metal-Semiconductor-Metal

NIR Near-Infrared region of the spectrum (750-1400 nm)

NEP Noise Equivalent Power

PCE Power Conversion Efficiency

PC Plasmonic Crystal

R Responsivity

SEM Scanning-Electron-Micrograph

SWIR Short-Wavelength Infrared

TAT Trap-Assisted-Tunneling

V_{oc} Open-circuit voltage

V_{mpp} Voltage at the maximum power point

VIS Visible region of the spectrum (380-750 nm)

3D Three-dimensional

Abstract

The detection of light is of central importance in both fundamental science and applied technology. Photodetectors, which aim at transducing optical stimulus into measurable electrical signals, are ubiquitous to modern society, and widespread from home-electronics to more sophisticated applications. Harnessing solar light-energy has the potential to replace current environmentally unfriendly fossil fuels, which is of paramount importance for a sustainable development.

Fostered by the strong interaction of light with metal nanostructures, Plasmonics have seen tremendous advances during the last decades. Unique phenomena such as intense electric field enhancement and localization, plus tunable and high absorption across the visible–infrared region of the spectrum are specially attractive for optoelectronic applications. In that framework, plasmonics have been introduced to improve the performance of photodetectors and solar cells by modulating the absorption in the active semiconductor. Another approach consists instead in harnessing the energetic, hot electrons, that arise after plasmon excitation in the metal. Within this scheme, unlike in semiconductors, light can be absorbed in the tens of nanometer scale and the optoelectronic spectral response tailored by metal-nanostructuring.

Plasmonic hot-electron optoelectronics has seen a very vivid research during the last years. Early progress focused in the field of photocatalysis, where metal nanoparticles where used to extend to the visible the spectral response of high-bandgap semiconductors. Prior to this thesis, no solid-state plasmonic solar cells had been reported. Further sensitization into the infrared was achieved by employing arrays of metallic nano-antennas in a metal-semiconductor Schottky architecture. The fabrication of these devices relied however on small-area and low-throughput lithographies, which complicates the deployment of this technology for photovoltaic and photocatalytic applications. Moreover, their performance remains yet on the low side.

The aim of this thesis is to further contribute to the development of this novel class of devices, with emphasis in photovoltaic and photodetection applications. We start

by identifying the crucial role of the interface on the photovoltaic performance, where we find that surface states hinder energy collection. We show that, by introducing an ultrathin insulating barrier, these defects can be passivated allowing for solar energy harnessing. This comes however at the cost of reduced hot-electron injection. The first part of this thesis is focused on the interface optimization by both inorganic (chapter 3) and organic (chapter 4) approaches. Inorganic passivation schemes allow for high open-circuit voltages and fill-factors, but the mediocre short-circuit current limits device performance. Organic passivation is achieved by the use of self-assembled monolayers (SAMs). By controlling molecule's shape and functionalization both open-circuit voltage and short-circuit current can be tailored, enabling for higher performances and quantum efficiencies that go up to 5%.

In chapter 5 we present a plasmonic crystal architecture to tailor the spectral response of hot-electron plasmonic photodetectors across the visible-near infrared. We identify and exploit the interplay between the different localized and lattice modes in the structure, with responsivities up to 70 mA/W. Notably, this architecture is fabricated by soft-nanoimprint lithography, a low-cost and high-throughput technique, compatible with large-scale manufacturing processes such as roll-to-roll.

We conclude by presenting routes towards more efficient plasmonic hot-electron optoelectronics (chapter 6). We show that, on top of catering for surface passivation, the metal-insulator-semiconductor architecture offers leverage in the design of solar cells and photodetectors. The presence of the insulating layer serves to substantially reduce the dark current, detrimental for open-circuit voltage and device sensitivity, compared to the bare metal-semiconductor counterpart. Projected solar power-conversion efficiencies up to 9% and specific detectivies above 10^{13} Jones can be achieved.

In summary, the results presented in this thesis showcase the potential of plasmonic hot-carrier optoelectronics for photovoltaic and sensing applications. Our findings represent a step forward for the deployment of this novel class of devices, and are also relevant to other areas such as photochemistry.

Resumen

La detección de la luz es de vital importancia, tanto para la ciencia fundamental, como para la tecnología aplicada. Los fotodetectores, cuyo fin es transducir estímulos ópticos en señales eléctricas, son ubicuos en la sociedad moderna, estando presentes en un amplio abanico de dispositivos desde electrónica para el hogar, hasta las aplicaciones más sofisticadas. El aprovechamiento de la energía de la luz solar tiene el potencial de reemplazar las actuales fuentes de combustibles fósiles dañinas para el medio ambiente, lo cuál es de importancia primordial en aras de un desarollo sostenible.

Empujada por la fuerte interacción de la luz con nanoestructuras metálicas, el campo de la plasmónica ha visto tremendos avances a lo largo de las últimas décadas. Fenómenos únicos, tales como el extraodinario aumento en la intensidad y la localización del campo eléctrico, en conjunción con una elevada absorción ajustable a lo largo de el espectro visible e infrarrojo, son especialmente atractivos para aplicaciones optoelectrónicas. En ese contexto, la plasmónica se ha usado con vistas a aumentar el rendimiento de una variedad de dispostivitos optoelectrónicos basándose en el incremento de la absorción en el semiconductor activo. Otra estrategia consiste en el aprovechamiento de los electrones energéticos que aparecen en el metal tras la excitación de un plasmón (comúnmente llamados electrones calientes). Bajo este enfoque, y en contraste con el caso de los materiales semiconductores, la luz puede ser absorbida en la escala nanométrica y la respuesta espectral ajustada según un nanoestrucutrado adecuado.

La optoelectrónica de electrones plasmónicos calientes ha vivido una intensa investigación a lo largo de los últimos años. Los primeros progresos se centraron en el campo de la fotocatálisis, donde nanopartículas metálicas eran utilizadas para extender la respuestra espectral de semiconductores con una elevada banda-prohibida. Antes de esta tesis, ninguna celda solar plasmónica en estado sólido había sido descubierta.

La sensitización hacia el infrarrojo de estos dispositivos se ha llevado a cabo utilizando distribuciones de nano antenas; la fabricación de éstas se ha basado en el empleo de litografías de pequeña área y bajo rendimiento, lo que complica una eventual

implantación de esta tecnología. Además de esto, la eficiencia de dichos dispositivos permanece a un nivel bajo.

El objetivo de esta tesis es profundizar en la contribución a esta nueva clase dispositivos optoelectrónicos, con énfasis en fotovoláica y fotodetección. Comenzamos por la identificación de la vital importancia de la interfaz en la eficiencia fotovoláica, donde encontramos que estados superficiales entorpecen la recolección de energía. Mostramos que, al introducir una capa aislante ultrafina, estos defectos pueden pasivarse permitiendo el aprovechamiento de la energía solar. Ello viene acompañado sin embargo, de una reducción en la inyección de electrones calientes. La primera parte de esta tesis se centra en la optimización de esta interfaz con estrategias inorgánicas (capítulo 3) u orgánicas (capítulo 4). La pasivación inorgánica permite alcanzar una alta tensión en circuito abierto y factor de llenado, pero la moderada corriente de cortocircuito limita la eficiencia de los dispositivos. La pasivación orgánica se lleva a cabo mediante el uso de monocapas moleculares autoensambladas. Al controlar la forma o la funcionalización de estas moléculas, tanto la tensión en circuito abierto como la corriente en cortocircuito pueden ser ajustadas permitiendo mayores rendimentos y eficiencias cuánticas de hasta del 5%.

En el capítulo 5 presentamos una estructura basada en cristáles plasmónicos para ajustar la respuesta espectral de fotodetectores fundamentados en electrones plasmónicos calientes, a lo largo del visible e infrarrojo cercano. En el mismo, identificamos y explotamos la interacción entre los diferentes modos de la estructura (localizados y de malla), con responsividades que van hasta los 70 mA/W. También importante, la fabricación de esta arquitectura se basa en litografía de impresión blanda, una técnica de bajo coste y alto rendimiento, compatible con procesos industriales como la fabricación rollo a rollo.

Concluimos en el capítulo 6 presentando rutas hacia dispositivos activos plasmónicos más eficientes. Mostramos que, además de proveer de la pasivación de estados en la interfaz, la arquitectura metal-aislante-semiconductor ofrece grados de libertad adicionales tanto en el diseño de celdas solares como fotodetectores. La presencia de la capa aislante sirve para reducir sustancialmente la corriente de oscuridad, factor perjudicial tanto para la tensión en circuito abierto como para la sensitividad de los fotodetectores. Nuestros calculos predicen eficiencias en la conversión de energía solar de hasta 9% y detectividades específicas en el rango de 10^{13} Jones.

En resumen, los resultados presentados en esta tesis demuestran el potencial de la optoelectrónica basada en electrones calientes para aplicaciones en fotovoltáica y en fotodetección. Nuestros descubrimientos representan un paso adelante en la compresión

de esta nueva clase de dispositivos, y son también relevantes para otras áreas tales como fotoquímica.

List of publications

This thesis is based on the following publications:

- **F. Pelayo García de Arquer**, and Gerasimos Konstantatos, "Efficiency Estimates for Metal-Insulator-Semiconductor Plasmonic Photovoltaics", *In preparation.*
- **F. Pelayo García de Arquer**, Agustín Mihi and Gerasimos Konstantatos, "Multiband Tunable Large Area Hot Carrier Plasmonic-Crystal Photodetectors", arXiv:1406.2875 (2013).
- **F. Pelayo García de Arquer**, Agustín Mihi and Gerasimos Konstantatos, "Molecular Interfaces for Plasmonic Hot-Electron Photovoltaics", *Nanoscale, accepted.*
- **F. Pelayo García de Arquer**, Agustin Mihi and Gerasimos Konstantatos, "Photoelectric energy conversion of plasmon-generated hot carriers in metal-insulator-semiconductor structures", *ACS Nano*, 7(4), 3581 (2013).

Other publications by the author:

- **F. Pelayo García de Arquer**, Tania Lasamta, Maria Bernechea and Gerasimos Konstantatos, "Sinergetic Plasmo-Electric Performance Enhancement of Colloidal-Quantum-Dots Photodetectors", *in preparation.*
- **F. Pelayo García de Arquer**, Tania Lasamta, Maria Bernechea and Gerasimos Konstantatos, "Tailoring the Electronic Properties of Colloidal-Quantum-Dots in Metal-Semiconductor Nanocomposites for High Performance Photodetectors", *Small, accepted.*
- A. Rath, **F. Pelayo García de Arquer**, Tania Lasanta, Alexandros Stavrinadis, Mara Bernechea, Silke L. Diedehofen and Gerasimos Konstantatos, "Remote trap passivation in colloidal quantum dot bulk nano-heterojunctions and its effect in solution processed solar cells", *Advanced Materials*, 26, 4741-4747 (2014).
- Alexandros Stanivdarnis, A. Rath, **F. Pelayo García de Arquer**, Silke L Diedenhofen, César Magén, Luis Martinez, David So, and Gerasimos Konstan-

tatos, "Heterovalent cation substitutional doping for quantum dot homojunction solar cells", *Nature Communications*, 4, 2981, (2013).

- **F. Pelayo García de Arquer**, Agustin Mihi and Gerasimos Konstantatos, "Photoelectric energy conversion of plasmon-generated hot carriers in metal-insulator-semiconductor structures", *ACS Nano*, 7(4), 3581 (2013).
- Fiona J. Beck, **F. Pelayo García de Arquer** and Gerasimos Konstantatos "Electrical effects of metal nanoparticles embedded in ultra-thin colloidal quantum-dot films" *Applied Physics Letters*, 101, 041103 (2012).
- A. Rath, M. Bernechea, L. Martinez, **F. Pelayo García de Arquer** and G. Konstantatos, "Solution-processed inorganic bulk nano-heterojunctions and their application to solar cells" *Nature Photonics*, 6, 529-534 (2012).
- G. Konstantatos, M. Badioli, L. Gaudreau, J. Osmond, M. Bernechea, **F. Pelayo García de Arquer**, F. Gatti and F.H.L. Koppens, "Hybrid graphene-quantum dot phototransistor with ultrahigh gain" *Nature Nanotechnology*, 7, 363-368 (2012).
- **F. Pelayo García de Arquer**, Fiona J. Beck, Maria Bernechea and Gerasimos Konstantatos "Plasmonic light trapping leads to responsivity increase in colloidal quantum dot photodetectors" *Applied Physics Letters*, 100, 043101 (2012).
- L. Martnez, M. Bernechea, **F. Pelayo García de Arquer** and Gerasimos Konstantatos "Near IR-sensitive, non-toxic, polymer/nanocrystal solar cells employing bismuth sulfide as the electron acceptor", *Advanced Energy Materials*, 23, 1029-1035 (2011).
- **F. Pelayo García de Arquer**, Fiona J. Beck and Gerasimos Konstantatos "Absorption enhancement in solution processed metal-semiconductor nanocomposites", *Opt. Express*, 19, 21038-21049 (2011).
- **F. Pelayo García de Arquer**, Vladimir Volski, Niels Verellen, Guy A.E. Vandenbosch and Victor Moshchalkov "Engineering the input impedance of optical dipole nano antennas: materials geometry and excitation effect", *IEEE transactions on Antennas and Propagation*, 59 (9), 3144, (2011).

1

Introduction

Optoelectronic devices, which aim at transforming light into electricity or vice versa, are nowadays ubiquitous and found in cross-disciplinary applications, from everyday products to more sophisticated technologies: imaging, sensing, spectroscopy, optical communications, renewable energies, lighting, health, food inspection and so on. The functionalities of optoelectronic devices are determined by the interaction of light with their constituent active materials. Underpinned by the advent of silicon and the deployment of the solid-state electronic industry, continuous technological advances have been achieved during the last decades. Here we focus on optical sensing and light-energy harvesting.

The field of plasmonics comprises the study of the interaction of light with free-electrons, typically in metals or highly-doped semiconductors. Under certain conditions, light can efficiently couple to this electron cloud giving rise to remarkable phenomena, such as very intense and confined electromagnetic fields. Plasmons are classified depending on the nature of their resonant behavior. Surface plasmons (SPs), are coherent electron oscillations that are bound to the metal interface and delocalized along its surface. They can be excited externally if an additional momentum is provided to the incident

light, for example, by a grating (Figure 1.1a). On the other hand, localized surface plasmon resonances (LSPRs) appear in nanostructured metals as a consequence of the restoring force exerted by the positive ion-cores left behind upon electron oscillation (Figure 1.1b).

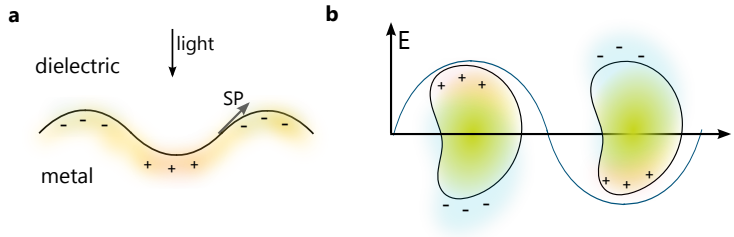

Figure 1.1: Types of plasmons and coupling schemes. (a) Surface plasmons (SPs) can be coupled by periodic corrugations of the metal-dielectric interface that cater for the extra momentum component. (b) Localized plasmons (LSPRs) arise in nanoparticles due to the restoring force existing between the displaced electron cloud and the positive ion cores.

The exceptional light-management capabilities endowed by plasmonic structures include: localization below the diffraction limit, field-intensities that can exceed by orders of magnitude that of the incident light, and a very strong light-matter interaction (via absorption and/or scattering), that can be tailored depending on the metal topology at the nanoscale [1–5]. This is in contrast to semiconductors, where absorption processes are determined instead by the bandgap of the material as electrons are promoted from the valence to the conduction band (Figure 1.2a). Moreover, total absorption in semiconductors typically requires much longer thicknesses (up to the micrometer scale for Si) whereas in properly structured metals this can take place within tens of nanometers [2–6] (Figure 1.2, panels b-d). The combination of these exciting properties with the increasing sophistication of nanofabrication techniques, has led to a very intense research during the last decades; this has resulted in thriving applications in cross-disciplinary fields, from biology to light-energy harvesting, that we briefly review in the next section.

1.1 Plasmonics and its applications

The use of plasmonics has allowed for a great number of advances in a plethora of fields, in view of the aforementioned light-management capabilities that go beyond classical optics. Fields such as biology [7], chemistry [8,9], medicine [10,11], information

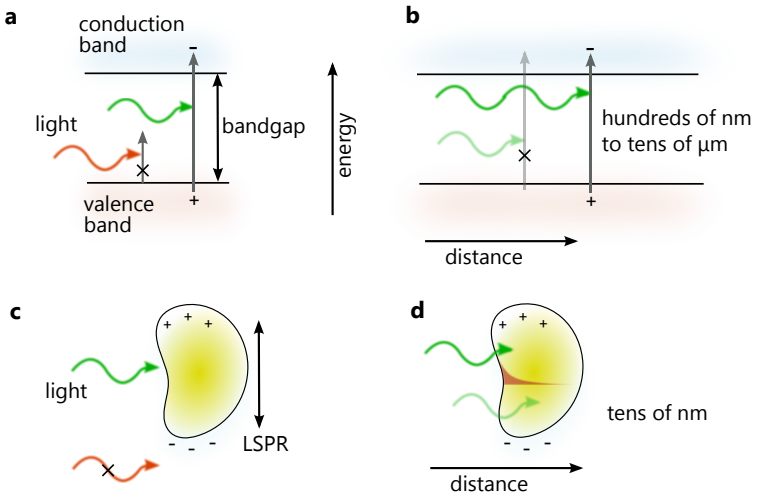

Figure 1.2: Absorption in semiconductors. (a) Only photons with high enough energy (above material's bandgap E_g) can be absorbed. (b) The absorption coefficient quantifies the probability for a photon to get absorbed while traversing the material. For semiconductors, this poses a minimum thickness that ranges from hundreds of nm (e.g. Ge, GaAs) up the micron scale (in the case of indirect bandgap semiconductors such as Si) for full visible absorption. (c) In nanostructured metals, the absorption is determined by the resonant nature of its electrons. (d) Full absorption can take place within tens of nm.

processing and quantum optics [12–14] or energy harvesting [15, 16]. Focusing below the diffraction limit opened the door for the manipulation of entities at the nanoscale, enabling for example, for single molecule spectroscopy or enhanced capabilities for ultra high-density data-storage. In conjunction with the enhanced electromagnetic fields bound to the plasmonic resonances, plasmonic sensors have seen tremendous advances [17]. Much effort has also been devoted during the last decades in order to improve the performance of optoelectronic devices, such as photodetectors and solar cells [15, 18–20], that we review in the next section.

1.1.1 Plasmonics for enhanced optoelectronics

The enhanced electromagnetic fields and light-matter interaction in plasmonic structures, soon attracted the attention of several research groups who aimed at improving the performance of photodetectors and/or solar cells by modulating the absorption in the active semiconductors layers of such devices. Three main mechanisms have been studied for that matter, that are shown in Figure 1.3. The enhanced scattering cross-section of plasmonic structures can be used to (i) improve the light coupling into

the underlying semiconductor and (*ii*) increase the photon path length in the semiconductor so as to enhance the absorption probability. Several groups have successfully reported photocurrent enhancements by using this approach, both for solar cells [21–32] and photodetectors [33–39]. Another interesting approach is to take advantage of the enhanced near-field intensity in the vicinity of plasmonic structures to increase the absorption rate in a neighboring semiconductor. In this case the structures need to be embedded inside the active layer, and often insulating layers are employed as to minimize pure electrical effects. This methodology is more challenging but has nevertheless been reported to improve the performance of a variety of solar cells [40–44]. The last approach consists of guiding and localizing the light into specific areas and locations. It has been proven useful for solar cells [45] and increasingly for photodetectors [46–49], where decoupling optical and electrical areas is interesting for noise minimization.

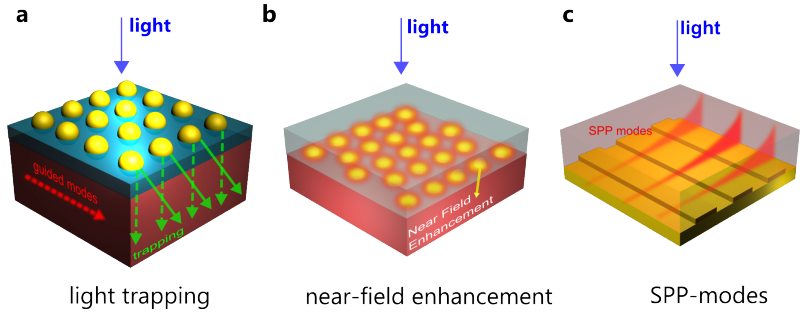

Figure 1.3: Plasmonics for enhanced optoelectronics. The strong light-matter interaction of plasmonic structures has been used to improve the performance of solar cells and photodetectors following different schemes: (a) by light-trapping, or increasing the path length of a photon inside a semiconductor. (b) By taking advantage of the strong near-field enhancement in the vicinity of such structures. If embedded in a semiconductor the net absorption could be increased. (c) By capturing, redirecting and focusing the light to specific locations. This allows to decouple the optical and electrical areas, which is interesting for noise minimization.

In summary, plasmonics has been widely employed to passively enhance the performance in semiconductors by modulating their absorption. The main challenges of this approach are the compatibility of device architecture with optimum plasmonic structuring and overcoming the parasitic absorption that takes place in these metal systems.

1.2 Active photodetection with metals

Photoelectron emission from metals has been known since Hertz's discovery in 1887, and the subsequent Einstein report on the photoelectric effect. If illuminated with high enough energy photons, metal electrons can be excited within the conduction band to eventually escape the metal potential and be emitted into another medium (Figure 1.4a). This phenomenon already found application for photodetection in the early 1900s, with photocathodes, vacuum photodiodes, or photomultiplier and streak camera tubes. This process, also known as internal photoemission, has been actively exploited in metals-semiconductor junctions from the early 1970's, where the electron emission yield (Y) was empirically found by Fowler to depend on the incident photon energy (E) as [50],

$$Y \propto (E - \phi_b)^2 \tag{1.1}$$

where ϕ_b is the resulting Schottky barrier height (Figure 1.4b). This relation was widely used to characterize the barrier, as it determines the spectral response of the photocurrent yield.

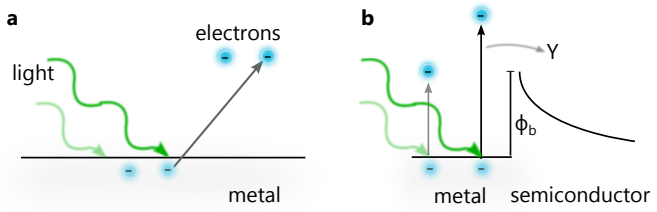

Figure 1.4: Photoelectron emission. (a) If illuminated with high enough energetic photons, metal electrons can excited and eventually escape the metal potential to be emitted into another medium. (b) In metal-semiconductor Schottky junctions, the emission yield is proportional to $(E - \phi_b)^2$.

The strong irruption of plasmonics, and the concomitant ability to tailor metallic nanostructures with nanometric precision, gave rise to the next question: can plasmonically excited electrons also be collected in a similar fashion? If so, this would open up the exciting possibility of a new generation of devices that, with the extraordinary properties offered by plasmonic light-matter interaction, could find application in a

wide range of fields. Preliminary works pointed to this direction [51], the first clear demonstration was reported in 2004 by Tian *et al.* in a photocatalytic system where the obtained action spectrum closely followed plasmonic absorption [52]. In this way, the photocurrent spectrum can be tuned by modifying plasmonic resonances,

$$Y_p \propto Y\alpha(E) \tag{1.2}$$

where $\alpha(E)$ is the plasmonic absorption. The physical mechanism enabling for the collection of plasmonic electrons is called Landau damping, a phenomenon upon which electron plasmas decay by generating electron-hole pairs. These energetic carriers are also referred to as hot-carriers, since they are out of thermal equilibrium with an effective Fermi temperature higher than the lattice. In the remainder of this thesis we will indistinctly use the term hot plasmonic carriers or hot plasmonic electrons to cite them. During the last years, the so-called hot-electron plasmonics has seen tremendous advances [53, 54].

1.3 Thesis objectives

The aim of this thesis is to develop a new class of optoelectronic devices whose functionalities are facilitated from the plasmonic nature of metal absorption. In particular we aim at answering the next questions focused in the areas of photovoltaics and photodetection:

- **Photoelectric energy conversion:** light-energy harvesting is of central importance for sustainable development—photovoltaic renewable energy sources being expected to replace environmentally unfriendly fossil fuels. Can optoelectronic devices be designed so as to exploit plasmonic electrons in a solar cell configuration? If so, how does the physics of these devices compare with standard semiconductor optoelectronics, and how can we tailor their functionalities?

- **Optimization of hot-electron injection yield:** the reported yields for plasmon hot-electron mediated photocurrent generation is still low for practical applications. Could it be possible to optimize hot-electron harvesting architectures to significantly improve this process?

- **Spectral tunability:** one of the main attractive features of active plasmonic optoelectronics is the possibility to geometrically tune the spectral response in such devices. Is it then possible to find a device architecture that, while catering for efficient and tunable photodetection be also compatible with large-scale manufacturing processes?

1.4 Thesis outline

The content of this thesis falls into the next chapters:

- In chapter 2 we introduce and describe the physics behind the generation and collection of plasmonic hot-electrons. We discuss the existent work and present the main challenges prior to this thesis: (i) the demonstration of solid-state active plasmonic solar cells and (ii) the necessity of a device architecture that, compatible with large scale fabrication processes, allows for the exploitation of plasmonic tunability with (iii) compelling performances.
- In chapter 3 we present a metal-semiconductor (MS) Schottky architecture to harvest plasmonic hot-electrons, and identify the crucial role of the MS interface for achieving light energy conversion. We show how the detrimental interface properties can be leveraged by the introduction of a thin insulating passivating layer, and how this affects the associated physical processes.
- In chapter 4 we delve into interface passivation, seeking to further improve device performance. We present the use of self-assembled monolayers (SAMs) to tailor the photovoltaic response of plasmonic solar cells. SAMs allow for much higher efficiencies leading to record power-conversion efficiencies.
- In chapter 5 we introduce plasmonic crystals as an efficient platform for tailoring the optical properties across the visible and near-infrared regions of the spectrum. Unlike in prior reports, we present the implementation of soft-nanoimprint-lithography, a roll-to-roll compatible large-scale manufacturing method, to fabricate highly tunable hot-electron plasmonic sensors. On top of that we report operating conditions leading record performances in the field.
- In chapter 6 we discuss the potential road-map for plasmonic hot-electron applications. We present theoretical performance limits for prototypical devices, and comment on the main opportunities and directions in the field.

2

Plasmonic-Hot Electrons

In the previous chapter we have introduced the benefits offered by plasmonic light-matter interaction, with emphasis in optoelectronic applications where plasmonics have been employed to augment the absorption in semiconducting materials. Electrically active plasmonic devices on the other hand, have remained largely underexplored. This approach, which consists on harvesting highly energetic electrons photogenerated in the metal, benefits from high optical absorption in metals, an effect that has been seen as an intrinsic limitation in other plasmonic applications for enhanced optical absorption in semiconductors or plasmon waveguides [15, 19, 20]. Unlike in semiconductors, where total light absorption takes place in the micrometer scale, the strong light-matter interaction of plasmonic systems allows for the design of quasi perfect and omnidirectional absorbers that are tens of nanometers thick [3–5, 55]. The high degree of spectral tunability enabled by metal nanostructuring goes beyond classical semiconductor band-to-band absorption, which opens the door for new applications. This chapter is organized as follows. First, we describe the fundamental processes behind plasmonic hot-electron generation. We then proceed to introduce and review the main hot-electron harvesting architectures for different applications. The fabrication techniques relevant for hot-electron devices are presented in section 2.3, with emphasis on

fabrication aspects such as throughput, scalability and associated cost. We conclude by outlining current challenges in the novel field of plasmonic hot-electron optoelectronics and by presenting the key objectives of this thesis.

2.1 Hot-electron generation

Metals can efficiently absorb light via: (*i*) intraband transitions from filled to empty states in the conduction band, (*ii*) interband transitions and (iii) the excitation of plasmons. Once excited, plasmons can loose their energy either radiatively (by emitting a photon) or non-radiatively, by generating an electron-hole pair within the metal conduction band (Figure 2.1). This process, so-called Landau damping, results in the generation of a hot-electron population, with a temperature exceeding that of the lattice and an energy dictated by the plasmonic resonance. The hot-electron generation efficiency is thus determined from branching ratio between non-radiative and radiative channels. A minimum re-radiation is therefore a pre-requisite for efficient hot-electron generation. The efficiency of the Landau damping mechanism, as well as the associated dynamics, strongly depend on factors such as size, shape, material and environment [56–58]. Typically, sizes smaller than 30 nm are required for more efficient non-radiative decay. Once excited, the hot-electron, out-of-equilibrium population, thermalizes at a given effective temperature distribution, that could be described by Fermi–or approximated by Maxwell-Boltzmann–statistics, via electron-electron scattering. These events typically take place within hundreds of femptoseconds [59]. Concurrently, heat is dissipated into the lattice by electron-phonon inelastic scattering within 3-5 ps [57]. The lifetime of out-of-equilibrium electrons in metals is also energy dependent, and inversely proportional to $(E - E_F)^2$ [60].

To harvest the hot-electron population, one must collect the excited electrons before thermalization. This means that electrons, which are only driven by their thermal motion, need to reach the metal interface in a fast timescale and retaining high enough kinetic energy so they can be extracted (Figure 2.2). The electron emission distribution is therefore important to describe this process. Although the Fowler-DuBridge theory for electron photoemission from metals assumes that electrons are emitted isotropically [50, 61], several reports indicate that the distribution of hot-electrons in the momentum space for nanostructured materials is not trivial, and depends on factors such as the crystal structure and field intensity [62–65]. As they move, excited electrons can undergo several scattering events with other free-electrons in the metal. In these inelastic collisions, the total momentum has to be conserved, resulting in the redistribution of the kinetic energy among the involved charges. The average distance traveled

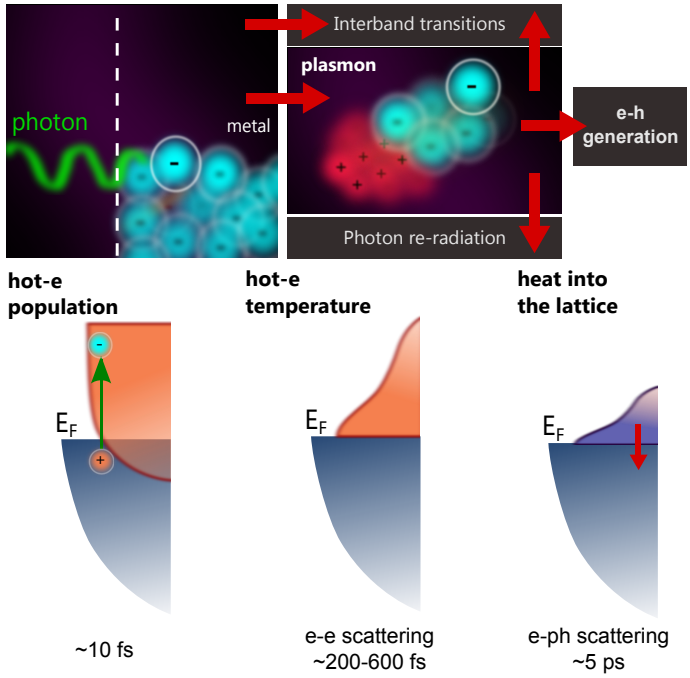

Figure 2.1: Plasmonic damping and hot-electron generation. Metals can absorb light either by: (i) intraband transitions from filled to empty states in the conduction band, (ii) interband transitions and (iii) plasmon excitation. Excited plasmons will loss their energy either radiatively or by exciting an electron-hole pair within the metal conduction band. This generates a hot-electron population with an energy dictated by the plasmonic resonance (in the femptosecond time-scale). The hot-electron, out-of-equilibrium population, establishes an effective Fermi-temperature by electron-electron scattering within hundreds of femptoseconds. Heat is be dissipated into the lattice by electron-phonon inelastic scattering within 3-5 ps [57].

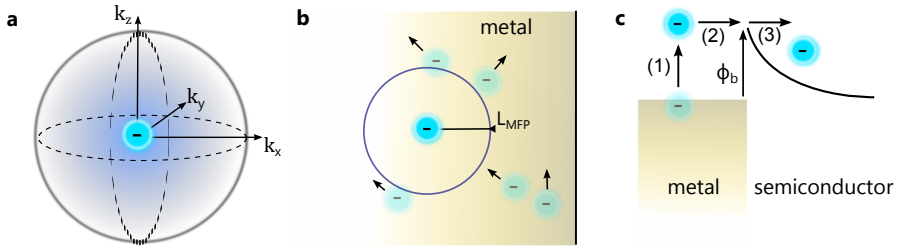

Figure 2.2: Hot-electron physics. (a) Thermally-excited electrons will move with a momentum $\mathbf{k} = k_x\mathbf{x} + k_y\mathbf{y} + kz\mathbf{z}$. The distribution of hot-electron emission in the momentum space is not trivial and depends on factors such as crystal structure and field intensity. (b) While in motion, excited electrons can undergo scattering events with other free-electrons in the metal. In this inelastic process the momentum is maintained and the kinetic energy distributed. An electron can statistically move collision-free within a distance L_{MFP}, so-called electron mean free path. (c) Three-step model to describe hot-electron injection over a Schottky barrier. (1) electron excitation, (2) transport to the interface and (3) tunneling over a barrier of height ϕ_b.

by an electron before electron and phonon scattering result in thermalization is the so-called electron mean free path (L_{MFP}). This quantity depends both on the material properties and on the electron energy [66], approximately following a $(E - E_F)^{-2}$ behavior. A simple, three-step model to qualitatively describe the processes involved in hot-electron injection over, for example, a Schottky barrier, is shown in 2.2c as formulated by Spicer *et al.* [67]. After electrons are excited (1), the ones arriving at the interface (2), with enough kinetic energy can tunnel to the semiconductor (3). Depending on the application, different architectures that harvest plasmonic hot-electrons have been used that we review in the following section.

2.2 Hot-electron harvesting architectures

The first evidences of hot-electron injection were reported in the field of photocatalysis [51, 52], seeking to extend the TiO_2photoanode response (limited by the bandgap of the material at 3.2 eV) into the visible. Within this approach, illuminated metal nanoparticles that are adsorbed onto the TiO_2, inject hot-electrons in the anode and get replenished by a liquid electrolyte (Figure 2.3a). The observation of these phenomena gave rise to subsequent increasing activity in the field of plasmonic photocatalysis [9, 41, 53, 68–85]. The application of plasmonic hot-electrons for photovoltaic applications was not reported until 2009, where in an analogue to a dye-sensitized configuration (Figure 2.3b), Chen et al took advantage of electron injection from gold nanoparticles to ZnO [86]. In this architecture plasmonic electron-hole pairs are split

and collected by electron transport layers (such as TiO_2or ZnO) and the electrolyte. In view of the some undesirable properties of liquid electrolytes for practical purposes, *viz.* electrode corrosion, leakage and degradation, solid state alternative materials, such as Spiro-OMeTad have also been explored [87]. In parallel, Wang *et al.* reported the visible sensitization of TiO_2solar cells where no hole-transport material, but a transparent counter electrode, was used, and suggested the possibility of energy harvesting in a metal-semiconductor only plasmonic solar cell [88]. Prior to this thesis all plasmonic hot-electron energy harvesting schemes relied on the use of photocatalytic or dye-sensitized devices.

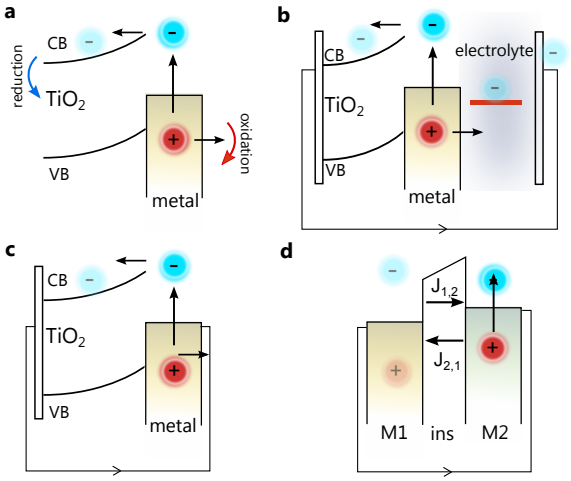

Figure 2.3: Hot-electron harvesting architectures. (a) Photocatalytic devices can take advantage of plasmonic hot-electrons by collecting electrons and holes, respectively, for reduction and oxidation processes. (b) In a dye-sensitized architecture a photocurrent can be obtained when energetic electrons from the metal are injected into the TiO_2while being replenished by the surrounding electrolyte. (c) In a Schottky metal-semiconductor (MS) diode, the structure allows the plasmonic electrode to act as a cathode, emitting hot electrons into the semiconductor (for example TiO_2, ZnO or Si). (d) A metal-insulator-metal (MIM) architecture can produce a net photocurrent provided the injection between electrodes is not balanced.

The simplest architecture to harvest plasmonic hot electrons is the metal-semiconductor (MS) Schottky junction (Figure 2.3c). In this approach, energetic electrons can be collected from the metal electrode provided they arrive to the interface with enough kinetic energy to overcome the existing barrier (ϕ_b). The built-in field that exists in the semiconductor aids the injected electron to recirculate and recombine with a hole in the counter electrode thus generating a plasmonic photocurrent. Due to its apparent conceptual and fabrication simplicity [89], several works made use of this architecture to report hot-electron plasmonic sensors in a Schottky diode or metal-insulator-metal

configuration [64, 90–98]. Among them, the work of Knight *et al.* set the ground for tunable plasmonic sensing, correlating the spectral response of the photocurrent with the plasmon resonance of metallic nano-antennas of different lengths. Despite the large number of works utilizing this architecture, in none of them was hot-electron photovoltaic response reported.

Another strategy to harvest hot-electrons is through the metal-insulator-metal (MIM) structure (Figure 2.3d). This scheme consists of two metal electrodes separated by an insulating layer. Electron injection can occur for barriers thin enough or under the presence of bias [99–101]. This architecture, adopted from the rectenna concept in the GHz and THz regimes [102], have so far suffered from low experimental efficiencies due to the presence of oxide insulating barriers which, on the nanometre scale and with shallow electron affinities, reduce hot-carrier injection [99, 101].

A major aspect that needs to be considered is the fabrication compatibility of these devices with the nanostructuring required for spectral tunability. Large-scale, low-cost manufacturing processes, are a requisite for photocatalytic and photovoltaic applications, but so far fabrication methods have consisted of low-throughput and costly methods. In the next section we review the main fabrication techniques employed in the literature for plasmonic hot-carrier devices.

2.3 Fabrication techniques for hot-electron devices

The fabrication of hot-electron devices relies on current techniques employed for plasmonic architectures. Proper metal nanostructuring schemes are thus required in order to precisely manipulate light interaction, which demands features be in the range of tens of nanometers. Most nano fabrication techniques can typically fall into two large categories, depending on the methodology and scale-sequence utilized during the process. Those are top-down and bottom-up methods. The first one encompasses large-scale patterning of down to nanoscale features, whereas the second relies on the sequential structuring from nano or atomic scale entities to create more complex architectures. Mainly driven by the semiconductor and IC industry, the use photolithography has been mastered and standardized. This technique relies on the use of an opaque mask that define exposure areas for a light-sensitive polymer (photoresist). Upon illumination, the physical properties of the polymer will change resulting in a patterned photoresist that can be employed in subsequent fabrication steps. Two main subclasses of photolithography exist depending on how the photomask is placed with respect to the resist: contact and projection printing. In the first one the mask physically contacts the resists, and allows features to be down to the μm scale. Projection printing, which

is more sophisticated, combines the photomask with UV lenses allowing to achieve resolution of few tens of nanometers at the wafer scale (see table 2.1). Despite the high throughput and the satisfaction of the fabrication criteria for metallic nanostructures, the machinery required is extremely expensive, where state of the art equipment would cost over 10M$ for example [103]. This approach is thus mainly utilized for ICs and CPU chip fabrication. The fabrication of most plasmonic structures, and in particular of hot-electron plasmonic IR-sensitized sensors, have relied to date on either electron beam (EBL), or focused ion beam (FIB) lithographies. EBL is based on the use of an accelerated electron beam that focuses on an electron-sensitive resist. Due to the high energy of the impinging, accelerated electrons, the resolution is well beyond the diffraction limit, mainly limited by resist processing. In spite of the great resolution capabilities offered by this technique, it is an expensive and multi-step process with a very low throughput thus incompatible with mass-production. FIB relies on the use of an accelerated ion beam. Within this approach metallic atoms are readily removed from the film by heavy-mass ion collisions. The same drawbacks hold however for this technique.

Soft-lithography was introduced first by Bain and Whitesides [104]. It relies on the use of a polymer stamp to imprint a solution of molecules onto a substrate. It requires inexpensive materials and equipment presenting itself as a low cost and high throughput technique. Following this methodology Nano-imprint lithography (NIL) utilizes a hard mold to imprint an elastomer polymer for nanoscale patterning. Patterns can be transferred to the resist with minimum local deformation, allowing features to be in the sub-10 nm range [105]. It holds the potential to surpass the aforementioned issues of both photolithograpy, EBL and FIB, for it combines high resolution with low cost, large throughput and large scale, and is compatible with already established manufacturing processes such as roll-to-roll. Another technique that combines being high throughput and low cost is the use of solution processable schemes for device fabrication. Metallic nanoparticles, or more complex shaped structures such as nanorods, tetrapods and platelets among others, can be synthesized in solution for device fabrication. Despite its potential, it has remained largely unexplored for plasmonic-hot electron devices beyond the visible regime (table 2.1).

In summary, all research related to plasmonic hot electron devices has relied on the use of metallic nanoparticles or randomly textured films for visible light sensitization, or on complex, expensive and low throughput techniques for extended spectral response. The lack of a platform capable of attaining spectral selectivity while meeting realistic fabrication criteria for large scale manufacturing is still a major impediment for the full exploitation of optoelectronic active plasmonic sensors.

Table 2.1: Summary of fabrication techniques for plasmonic devices. Adapted from [105]

Fabrication Technique	Minimum Feature Size	Throughput	Cost	Regime	Refs.
Photolithography (contact)	1μm	high	high	NIR	-
Photolithography (projection)	tens of nm	high	high	VIS-NIR	[6]
Electron beam lithography	5 nm	low	high	VIS-NIR	[92, 106, 107] [64, 101, 108]
Focused ion beam lithography	5-20 nm	low	high	VIS-NIR	[98]
Soft-lithography	tens of nm	high	low	VIS-NIR	-
Nano-imprint lithography	<10 nm	high	low	VIS-NIR	-
Solution processable routes	1 nm	high	low	VIS-NIR[1]	[52, 70, 72] [73, 79, 87]
Electrodeposition or metal coalescence	30 nm	high	low	VIS	[71, 94] [81, 85]

2.4 Figures of merit

In this section we briefly outline the main figures of merit of optoelectronic devices for both photodetection and photovoltaic applications.

Photodetectors

An optoelectronic photodetector is characterized for transducing an optical stimulus into an electrical signal. One stand-alone figure of merit to quantify the electrical response of the detector is the responsivity (R). This quantity reflects how much electrical current is obtained per incident optical power and is measured in amperes (or volts) per watt. Responsivity can be translated into another figure, the external quantum efficiency (EQE), that yields the number of photogenerated electrons collected per incident photon. This quantity lies within the $[0, 100\%]$ interval unless multiplication gain mechanisms take place. The internal quantum efficiency (IQE) is subtly different, as it reflects instead how many electrons are collected per absorbed photon. In the absence of illumination a photodetector is characterized by its dark current, which

should be minimized to lower power consumption and associated noise processes. The sensitivity, or the minimum optical power that a detector can discern, is expressed by the noise equivalent power density (NEP), that combines both responsivity and noise spectral power density S_n. Another, more complete figure of merit to qualify the performance of photodetectors is the so-called specific detectivity (D^*). Unlike NEP, D^* also accounts for device area and bandwidth, allowing cross-comparison between different families of devices. These photodetector figures of merit are summarized in table 2.2.

Table 2.2: Photodetector figures of merit.

Name	Expression	Units	Definition
Responsivity (R)	$I_{ph}(\lambda)/P_{inc}$	A/W	Photocurrent per incident optical power
EQE	$hcR/(\lambda q)$	-	Electron ratio to to incoming photon rate
IQE	EQE/$a(\lambda)$	-	Electron ratio to to absorbed photons $a(\lambda)$
Dark current (I_d)		A	Current without illumination
NEP	S_n/R	W/Hz$^{1/2}$	Noise equivalent power power. S_n is the noise spectral power density
Normalized detectivity ($D^\star$)	$\sqrt{A_d B}/NEP$	Jones (cm Hz$^{1/2}$/W)	Detector's sensitivity normalized to area A_d and bandwidth B.

Photovoltaic devices

In order for a solar cell to deliver power into a load, it must simultaneously sustain a voltage and deliver current while illuminated (Figure 2.4). The voltage at open-circuit conditions is called the open-circuit voltage (V_{oc}), while the current at short-circuit conditions short-circuit current (J_{sc}). Maximum power throughput occurs at the point (V_{mpp}, J_{mpp}). The fill factor (FF) quantifies how well a solar cell takes advantage of V_{oc} and J_{sc}, and calculated as the ratio of maximum power with their product. It ranges between 0 and 1, with 1 corresponding to the ideal case. These figures of merit are

also summarized in table 2.3. The spectral response of solar cells is characterized by the EQE and IQE measured at short-circuit conditions.

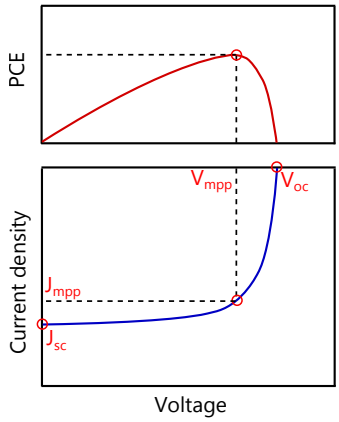

Figure 2.4: Solar cell operation and figures of merit. In order to be able to deliver power, a solar cell must sustain a voltage while delivering current. The voltage at open-circuit conditions is called open-circuit voltage (V_{oc}) and the current at short-circuit conditions short-circuit current (J_{sc}). Maximum power throughput occurs at the point (V_{mpp}, J_{mpp}). The fill factor (FF), is the ratio of maximum attainable power with the product V_{oc} J_{sc}.

Table 2.3: Figures of merit of photovoltaic devices.

Name	Expression	Units	Definition
Open-circuit voltage (V_{oc})		V	
Short-circuit current (J_{sc})		A	
V_{mpp}		V	Voltage at maximum power point
J_{mpp}		A	Current at maximum power point
Fill Factor (FF)	$V_{mpp}J_{mpp}/V_{oc}J_{sc}$		
PCE	$V_{oc}J_{sc}\mathrm{FF}/P_{inc}$		Power-conversion efficiency

2.5 Prior art in hot-electron optoelectronics

In this chapter we have introduced the main physics of plasmonic hot-electron generation. Despite the increasing amount of research in plasmonic hot-electrons for sensing and energy harvesting applications, most of the efforts have focused in the area of photocatalysis. Prior to this thesis the state of the art in hot-electron optoelectronics

could be summarized as follows:

- **Photocatalytic devices:** the first demonstration of active plasmonic devices dates back to the work of Tian *et al.* at 2004 [52]. This started a very active research in the field, which relied on the use of metal nanoparticles or electrodeposited architectures to extend the response of wide-bandgap semiconductors in the visible [109]. At 2010 sensitization into the near-infrared was reported by Nishijima and coworkers following an EBL fabrication procedure [106].

- **Schottky diodes:** early demonstration of active surface plasmon detection dates back to 2009 by using MIM waveguides or nanowires or Schottky junctions [90,91]. In 2011 Knight *et al.* correlated the plasmonic properties of optical nanoantennas, such as length and polarization, with the hot-electron spectral response [107]. The responsivity of these devices was rather low, on the order of few μA/W, and fabricated by EBL. In none of these devices a photovoltaic response was reported.

2.6 Challenges in hot-electron optoelectronics

Based on the prior art in hot-electron optoelectrons, this aim of this thesis was to accomplish the next challenges:

- **Demonstration of a plasmonic Schottky solar cell:** active plasmonic devices for light energy harvesting have relied so far in a dye-sensitized like architecture. Herein we explore the option of building a more robust, all-solid state metal-semiconductor solar cell, where photoexcited carriers are derived from the plasmonic excitation of the metal electrode.

- **Active control over photovoltaic figures of merit:** the unconventional physics of plasmonic solar cells leave an open question. Can figures of merit such as open-circuit voltage and short-circuit current be tailored to optimize the overall power conversion efficiency?

- **Large scale and tunable fabrication scheme:** one the most appealing opportunities endowed by the plasmon generation is the possibility to tailor the spectral photoresponse of hot-electron devices for specific applications. We have seen however that, as to this point, all reports have relied on the use of low throughput and costly fabrication techniques. In this thesis we examine novel plasmonic photodetector architectures which on top of a high degree of tunability are compatible with large scale manufacturing processes.

- **Compelling performance:** despite the great and rapid achievements in plasmonic hot-electron photodetection, reported device performances are still orders of magnitude far from current established technologies [18, 110, 111]. Advancing the performance of hot-electron devices is therefore of paramount importance for this technology to be commercially employed.

3

Plasmonic Hot-Electron Photovoltaics

Photovoltaic devices that exploit plasmonic hot-electrons have relied so far on a dye-sensitized architecture. A more robust and straightforward approach for hot-electron harvesting is the Schottky metal-semiconductor junction. Despite the intense research in the field, Schottky solar cells that take advantage of plasmonically generated carriers have never been reported hitherto. In this chapter we identify the crucial role of the interface in a Schottky junction to demonstrate for the first time active plasmonic Schottky solar cells. First, the plasmo-electric effect is demonstrated with quantum efficiencies up to 4%, but in the absence of photovoltaic effect. In the next section, surface states at the semiconductor-metal interface are identified to pin the semiconductor Fermi level, leading to the eventual reduction or suppression of V_{oc}. To surmount the detrimental effect of these states we report the use of an ultrathin inorganic layer that enable their passivation thus recovering V_{oc} and producing a photovoltaic effect. The introduction of this passivation layer results however in a strong modification of hot-carrier injection mechanisms, and comes accompanied by a reduced hot-carrier injection efficiency and J_{sc}. The presented passivation scheme is then optimized for higher J_{sc} while sustaining V_{oc}, yielding a maximum PCE = 0.03%. The spectral harnessing potential is assessed for different metals, which result in a joint modification of the

plasmonic and electronic properties of the devices. Hot-carrier injection and transport mechanisms are finally proposed that account for the observed differences.

3.1 Plasmonic photoelectric conversion

As introduced in the previous chapter, two conditions need to be simultaneously satisfied in order to harvest plasmonic hot-electrons: (*i*) efficient incident light to plasmon coupling structure, that must be compatible with a given device architecture, and (*ii*) the presence of a static electric that separates plasmonically generated electron-hole pairs before thermal relaxation. The first condition calls for a proper metal nanostructuring, that can couple efficiently incident light to plasmons. The fabrication method should ideally be compatible with large-scale manufacturing processes, a requisite for light energy harvesting applications. Metal-semiconductor Schottky junctions are the most straightforward platform for hot-electron collection. The optoelectronic properties of these junctions depend on the selection their metal and semiconductor constituents.

Device architecture: TiO_2 was chosen as a well known, earth-abundant and wide-bandgap semiconducting material, widely used as a transparent (3.2 eV bandgap) electron transport layer in photovoltaic and photocatalytic applications. Subwavelength textured substrates made of TiO_2 nanocrystals can be easily fabricated via a solution-processed route, by –for example– spin casting a TiO_2 paste of nanoparticles of a given size. A corrugated metal layer, enabling light-plasmon coupling, can be then obtained by simply evaporating a metal layer on top of these textured substrates. In the Schottky configuration the metal serves a two-fold purpose: it provides with a source of plasmonic hot-electrons and also acts as the anode for the extraction of holes. The final device architecture is depicted in Figure 3.1. Light illuminates the metal-semiconductor interface through a transparent conductive oxide (TCO) and a TiO_2 layer.

Photocurrent generation: Electron-hole pairs are generated in the textured electrode, a fraction of which will separate once energetic electrons are injected into the TiO_2 to recirculate until they reach the TCO to close the circuit recombining with an available hole. The texturing of the interface was characterized with atomic-force microscopy (AFM) measurements (Fig 3.1b), and shows features up to 90 nm in height. This serves as an efficient platform for plasmon excitation with an resonant absorption up to 70% at 450 nm (Figure 3.1c) that yields a hot-electron photocurrent, with a

maximum EQE of 4% at resonance. The shape of the spectral profile is in agreement with the plasmonic absorption of the textured electrode. Flat control references on the other hand do not exhibit plasmon excitation or photoresponse below the bandgap of the semiconductor(Figure 3.1d-f). This showcases the feasibility of our structure for active plasmonic sensing, yet it still does not allow for energy conversion.

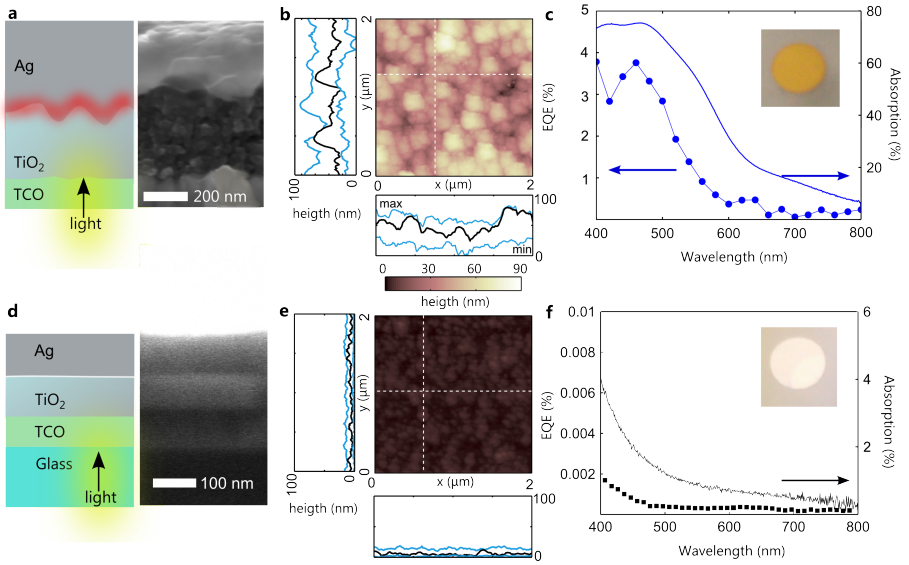

Figure 3.1: Photoelectric conversion in active plasmonic devices. (a) The proposed architecture consists of a TiO_2 layer deposited on top a transparent conductive oxide. (b) The roughness of the TiO_2, was characterized with AFM measurements, with a height in the range between 10 and 100 nm. (c) The top-deposited Ag electrode follows TiO_2 corrugation thus enabling plasmon excitation. This is confirmed both by visual inspection (inset, different color metal films) and absorption measurements. The obtained EQE correlates well with the plasmonic absorption and reaches up to 4% at resonance. (d-e) Flat reference devices show on the other hand no appreciable photoelectric transduction in the visible due to the lack of plasmonic excitation.

In this section we have demonstrated that TiO_2-Ag Schottky junctions can be used for active plasmonic sensors. However, photoelectric energy conversion requires the simultaneous supply of current and voltage. In the next section we identify metal-semiconductor interface states as the origin of V_{oc} suppression, and introduce mechanisms to passivate these defects that enable plasmonically active Schottky junctions to operate as photovoltaic devices.

3.2 Interfaces and photovoltaic effect

Metal-semiconductor junctions are perhaps one of the most studied systems in solid state electronics. Because of their apparent simplicity, simple models were elaborated in the early 1900 that rely on the characteristics of the bulk metal and semiconductor. A metal can be electronically described by its workfunction ($q\phi_m$), and a bulk semiconductor by its bandgap E_g, electron affinity $q\chi_{sc}$ and doping nature $q\phi_n$. Once in intimate contact, charge will redistribute until thermal equilibrium is achieved equalizing the Fermi level across the junction. The final barrier height for an ideal system would be given by,

$$q\phi_b = q(\phi_m - \chi_{sc}) \tag{3.1}$$

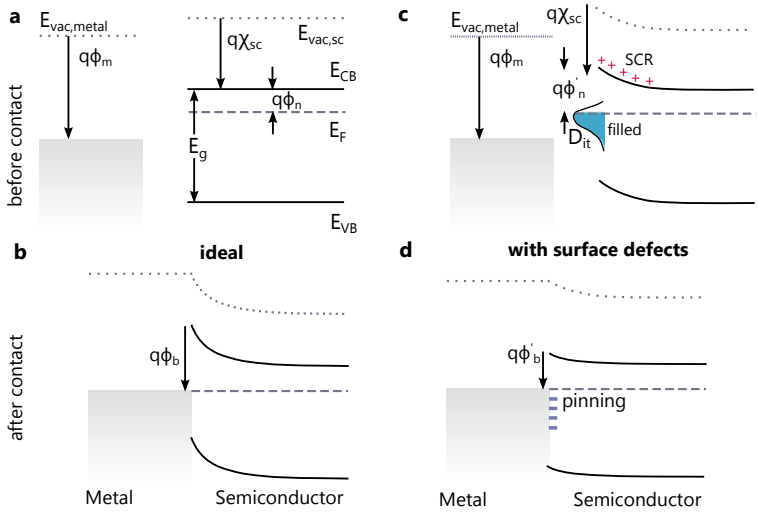

Figure 3.2: Schottky junctions and Fermi level pinning. (a-b) Ideal case of a Schottky diode formation. A semiconductor layer is characterized by its bandgap E_g, electron affinity $q\chi_{sc}$ and doping character $q\phi_n$. The metal electrode by its workfunction $q\phi_m$. (b) Upon intimate contact and thermal equilibration a barrier $q\phi_b = q(\phi_m - \chi_{sc}$ will appear. (c-d) The presence of surface states in the semiconductor will result in the creation of a space charge region in the semiconductor and a corresponding pinning of the Fermi level. As a consequence of this the Schottky barrier after contact $q\phi'_b$ might be reduced or eventually canceled.

This would yield, in an ideal case, an approximate $q\phi_b = q\phi_{Ag} - \chi_{TiO_2} \approx 0.6eV$ if applied to a TiO_2-Ag junction. This value is in reality lowered both by image force

screening effects and by the presence of interfacial states. Considering therefore, the TiO_2 and Ag bulk properties alone, do not suffice to precisely describe the system. Instead, the electrical properties of Schottky-junctions are often governed by the metal-semiconductor interface, where the periodic character of crystals is interrupted resulting in the presence of dangling bonds, different exposed facets, off-stoichiometry products and unknown surface adsorbates. These defects introduce a set of trap-states across the bandgap of the semiconductor, and will result in the modification of the electrostatic properties at the interface. In a picture where traps are acceptor states (typical for an n-type material such as TiO_2), this will result in the donation of electrons from the crystal lattice to these sites and in the subsequent formation of a positively charged region, that pins the Fermi level at the surface of the material (see Figure 3.2). The presence of surface states can therefore substantially lower the *a priori* expected barrier height, or even result in its eventual cancellation.

We took the view that the expected open-circuit value in our TiO_2-Ag architecture was hindered by the presence of interfacial states leading to Fermi level pinning. As the ideal barrier height in this configuration should be approximately 0.5 eV, we were encouraged that a proper passivation would enable for active, hot-electron, plasmonic photovoltaic devices.

Passivation of the interface: one approach to passivate interface states is to introduce thin barriers capable of repairing dangling bonds and providing excess carriers which fill trap states. Alumina (Al_2O_3) barriers have been widely used to reduce recombination in dye sensitized and silicon solar cells [112–115]. The deposition of alumina over these materials can significantly lower the density of interface acceptor states due to the termination of dangling bonds and the high density of negative charges inherent to this material [115]. We thus turned our attention to a metal-insulator-semiconductor (MIS) structure, where we deposited an ultrathin layer, 1 nm thick, of Al_2O_3 on top of TiO_2, with a view to reduce the density of surface states and form a junction that can support open-circuit voltage. To do this, we relied on the use of thermal atomic layer deposition (ALD), because of its ability to produce continuous conformal films with controllable thicknesses at the atomic scale at low processing temperatures (80 °C) [116]. In the absence of the Al_2O_3 layer, current-voltage characteristics under simulated solar illumination (AM 1.5G), show very high photocurrent yet no photovoltaic effect (Figure 3.3a,c). Without a protective barrier, the Ag-TiO_2 interface states result in Fermi level pinning and a dramatically reduced built-in potential (Figure 3.3, panel e). The presence of the Al_2O_3 layer caters for surface passivation thus allowing the presence of an open-circuit voltage (Figure 3.3b,d). To further corroborate the origin of open-

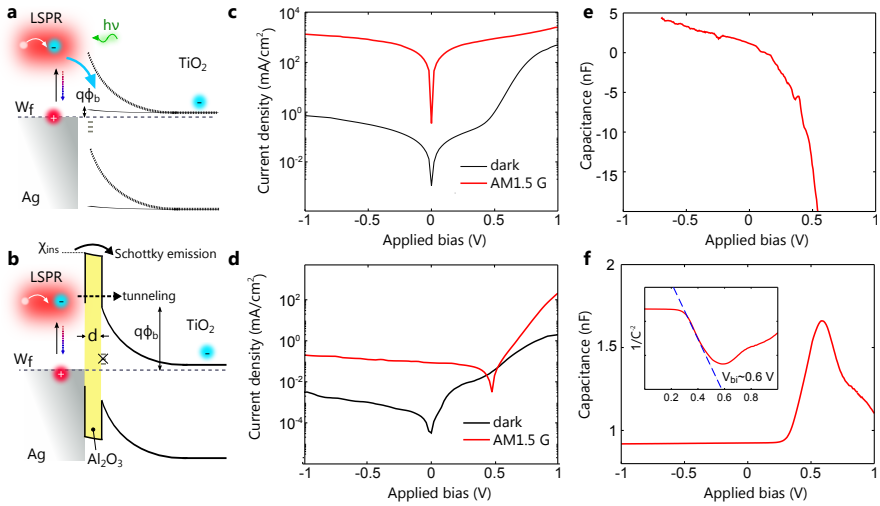

Figure 3.3: Interface passivation and hot-electron photovoltaics. Plasmons excited by an incoming photon drive the creation of an electron-hole pair, which can be split by the built-in field at the interface. Non-passivated interfaces (a) contain traps that can result in Fermi level pinning deteriorating the junction from the ideal case (solid versus dashed lines respectively). This results in a suppression of open-circuit voltage (V_{oc}) and no power conversion efficiency (PCE) (c). Passivation of the interface states prevents pinning (b). Depending on the energy of the excited electrons they can tunnel to the TiO_2 or undergo Schottky emission over the barrier. The height of the barrier is determined by the difference of the metal work-function ($W_f = q\phi_m$) and the insulator electron affinity (χ_{ins}) (d) current-voltage characteristic in dark and under simulated AM1.5G solar illumination of a typical passivated device with 1 nm of alumina. Capacitance-voltage spectroscopy of not passivated devices (e) and passivated devices (f) revealing the appearance of a built-in potential (Mott-Schottky analysis shown in the inset).

circuit-voltage and the effect of Al_2O_3 passivation, we performed capacitance-voltage spectroscopy of these devices (panels e-f). Without the insulating layer, the built-in field vanishes resulting in open-circuit voltage cancellation. The inclusion of the Al_2O_3 layer (Figure 3.3f) leads however to built-in potentials that are on the order of 600 mV (see Mott-Schottky plot in the inset). Note that this value can be higher than the ideal value as it comprises both the Schottky barrier (ϕ_b) and the dipole shift induced by the insulator. In the current structure, electron-hole pairs derived from plasmon damping are split when, depending on their energy, electrons tunnel through or are emitted over the insulating barrier. Hot-carriers generated in the metal that are transferred to the titania rapidly thermalize to the conduction band. Current-voltage characteristics of a typical device with 1 nm of Al_2O_3 barrier are shown in Figure 3.3d, in dark and under AM1.5G simulated illumination, demonstrating the ability of plasmonic MIS devices to harvest solar energy and convert it to electricity. To experimentally assess the contri-

bution of plasmonic hot-electrons in the total PCE, we also performed measurements under various filtering conditions to reduce photon absorption from the TiO_2 phase in the devices. In doing so we found that the contribution from the visible region (below TiO_2 bandgap) is in the range of 80% of J_{sc} (Figure 3.4). This is in agreement with the expected contribution to the total J_{sc} estimated contribution from the EQE region above 380 nm (Figure 3.5).

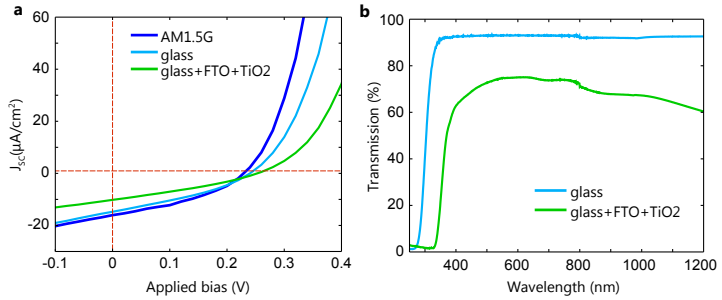

Figure 3.4: Isolating TiO_2 contribution from solar cell performance. (a) Current-voltage characteristics under simulated solar irradiance AM1.5G of a TiO_2/Al_2O_3(1 nm)/Ag sample without filtering, and removing different parts of the UV spectrum. (b) Transmission spectra of the different filters used to remove TiO_2 contribution.

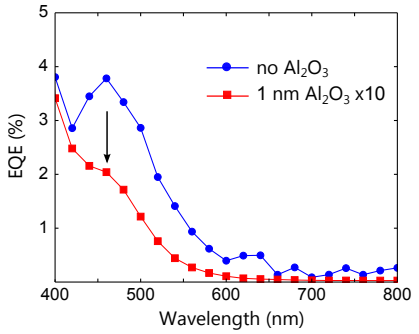

Figure 3.5: Effect of Al_2O_3 passivation on quantum efficiency. The passivation of interface states hindering the photovoltaic performance of hot-electron devices results in a substantial reduction of the injection efficiency from the metal electrode as a consequence of the alumina barrier.

Impact on the injection yield: the achievement of V_{oc} is followed by a reduction in J_{sc}, that drops from around $400\mu Acm^{-2}$ to $40\mu Acm^{-2}$. It is evident then that the alumina layer, responsible for surface passivation, is also modifying hot-electron injection from the metal electrode. We verified the reduced EQE of these devices compared with the one obtained in the absence of Al_2O_3 (Figure 3.5). The injection

efficiency drops from a 4% peak value to 0.2%. This confirms that the insulator layer is dramatically reducing the emission and tunnelling probability, and necessitates further optimization to alleviate this current drop while sustaining reasonable values of V_{oc}. We then sought to optimize our device structure by taking advantage of the atomic layer resolution of the ALD technique to build Al_2O_3 layers of different thicknesses with a view to minimizing the length of the barrier yet preserving its beneficial passivation features. This is presented in the section that follows.

3.2.1 MIS optimization

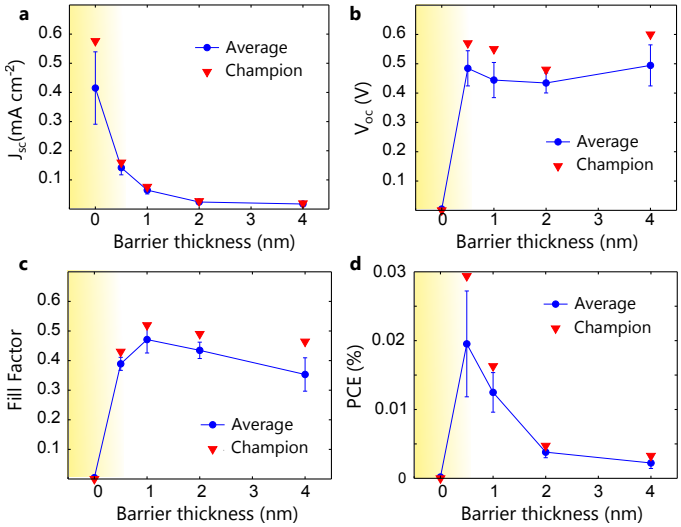

Figure 3.6: Interface optimization statistics. (a) Short-circuit current (J_{sc}), (b) Fill-Factor (FF), (c) open-circuit voltage (V_{oc}) and (d) power conversion efficiency (PCE) for different Al_2O_3 thicknesses (d). Error bars correspond to the standard deviation. Statistics calculated for at least 5 similar devices. Champion values for each parameter are also shown (triangle marker). A maximum PCE of 0.029% is found for d=0.5 nm.

The influence of the insulator layer thickness d on the photovoltaic figures of merit of our devices is shown in Figure 3.6. As expected, the short circuit current density (Figure 3.6a) increases with decreasing d, indicative of a more efficient transfer of the excited hot electrons to the semiconductor. It reaches a maximum in the absence of the Al_2O_3 barrier, but as previously discussed, at this point Fermi-level pinning results in tiny or null V_{oc} and no net PCE. The fill-factor is maximum at $d = 1$ nm. Thicker alumina films yield higher series resistance and marginal decrease in FF [117]. Thinner barriers are more prone to back-recombination of the injected carriers which also partially decrease FF. The open-circuit voltage does not significantly change with

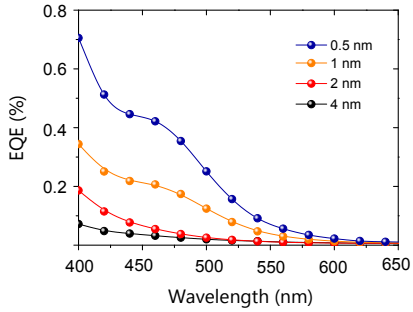

Figure 3.7: Quantum efficiency as a function of d. As the alumina thickness d increases, the photocurrent contribution from the plasmon resonance of the Ag electrode is drastically reduced. For thicknesses below 2 nm the amount of hot-electrons than can tunnel to TiO_2 increase exponentially yielding a maximum EQE of 0.4% at the plasmon resonance for $d = 0.5$ nm.

thickness variation. As a consequence, the dependence of PCE with thickness is mainly correlated with J_{sc}, provided there is no Fermi-level pinning. A maximum value of PCE = 0.029% is obtained for $d = 0.5$ nm devices, with J_{sc} of 0.14 $mAcm^{-2}$, V_{oc} of 0.48 V and fill-factor of 0.46.

The EQE of MIS devices for different alumina thicknesses is shown in Figure 3.7. As the alumina thickness decreases the contribution from the Ag plasmon resonance becomes more prominent and reaches its maximum, of around 0.45%, for $d = 0.5$ nm. Increasing values of d result however in a drastic reduction of EQE and a vanishing plasmon contribution due to the exponential decrease of the tunnelling probability with barrier thickness.

3.2.2 Influence of the metal: Au-based MIS devices

The spectral harnessing potential of the plasmonic MIS structures can be exploited by the choice of the metal and/or geometry. Changing the metal electrode will both modify the electrical and optical properties of the devices: different metal workfunctions will result in different band alignments; the shifted plasmon resonance, arising from the different metal properties, will also yield to a different hot-electron distribution and dynamics. This has immediate implications from a physics and device-design point of view. We sought to experimentally assess these differences by studying Au-based MIS devices. Similar to the case of Ag-based devices, in the absence of Al_2O_3 Fermi level pinning limits the photovoltaic performance due to the lack of an open-circuit voltage. The introduction of Al_2O_3 allows for the recovery of a built-in potential (Figure 3.8) in the range of 200-300 mV.

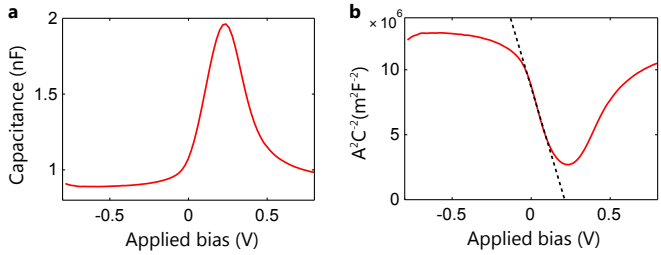

Figure 3.8: Capacitance-voltage and built-in potential of Au devices. (a) Capacitance-voltage of a TiO_2/Al_2O_3/Au device for an alumina thickness of 1 nm. (b) The Mott-Schottky analysis reveals a built-in field of 200 mV.

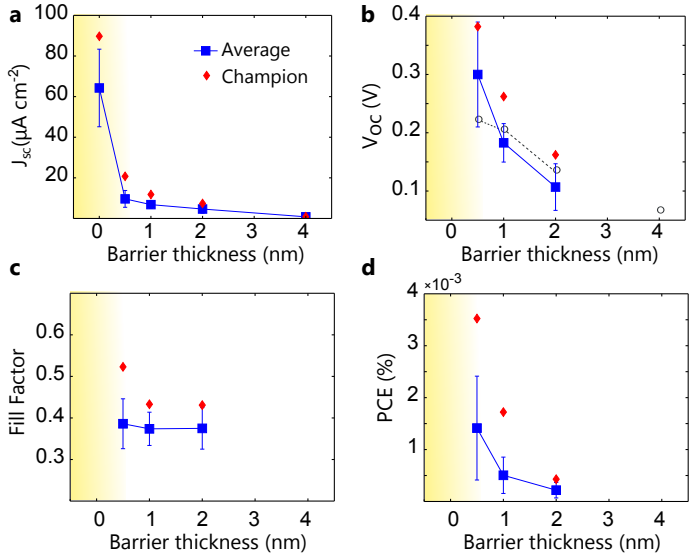

Figure 3.9: Interface optimization statistics for Au devices. (a) Short-circuit current (J_{sc}) and (b) open-circuit voltage (V_{oc}). Also plotted (dashed line) $\ln(J_{sc}/J_d + 1)$, showcasing the origin of the varying V_{oc} dependence with d. (c) Fill-Factor (FF) and (d) power conversion efficiency (PCE) for different Al_2O_3 thicknesses (d). Error bars correspond to the standard deviation. Statistics calculated for at least 5 similar devices. Champion values for each parameter are also shown (diamond marker). For $d = 4$ nm the tunnelling current is negligible and the subsequent parameters omitted in the plots.

Interface optimization: we proceeded then to study the effect the thickness of the alumina layer has in the photovoltaic performance of Au-MIS devices (Figure 3.9). Short-circuit currents (Figure 3.9a) are lower than for Ag electrodes (around one order of magnitude) but follow a similar trend with Al_2O_3 thickness. Interestingly, open-circuit voltages vary between 0.1V and 0.4V, while being in general lower than the ones obtained for silver. This is attributed to the lower built-in potentials (Figure 3.9b) for gold samples. The $V_{oc} - d$ trend is ascribed to a different functional dependence of J_d (dark saturation current) and J_{sc} with d, as the V_{oc} scales with $\ln(J_{sc}/J_d + 1)$. This is indeed, as illustrated in the inset, the case for Au samples, pointing towards different transport mechanisms for thermally excited (dark current) and photogenerated carriers. The fill-factor is not varying significantly with d. The overall trend of efficiency with thickness is similar to that of Ag devices, although it is evident that both the electronic properties and the plasmo-electric conversion performance of devices with gold electrodes are different. In the next section we will further analyze these differences and elucidate the underlying responsible mechanisms.

3.2.3 MIS photodiodes

Besides the photovoltaic regime, Schottky photodiodes can also be operated under reverse bias conditions for sensing applications. The application of a voltage would results in a band alignment modification across the device (see for example Figure 3.10), making a useful tool in understanding the underlying physics of the plasmo-electric conversion process. Having this in mind we sought to investigate the difference of Ag and Au MIS devices at different bias conditions. The EQE of the devices at short-circuit, with -0.5V and -1V biases is shown in Figure 3.10b-c. To preclude possible midgap states in the titania as a source of visible photosensitization in these devices, we also fabricated devices in which the metal has been replaced by a transparent conductive oxide of ITO.

Reverse bias operation: the application of increasing reverse voltages in Ag devices results in a subtle increase of efficiency that tends to saturate for -1V. This suggest that in this configuration, the modification of the potential distribution across the device has little effect on the injection of hot-carriers from the metal electrode. The tiny variation at 400 nm also points towards an almost fully depleted TiO_2 layer that does not benefit from any further band-bending. A maximum EQE of 0.64% is obtained at the plasmon resonance under 1V reverse bias. Au MIS devices, on the other hand, show a remarkably different behavior (Fig 3.10c). The EQE under short-circuit conditions is much lower than that for silver devices (0.025% versus 0.42% at resonance), yet with

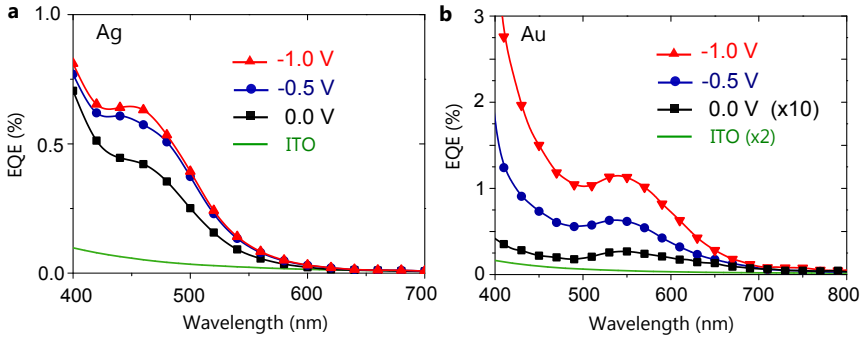

Figure 3.10: Photodiode performance of hot-electron MIS devices. (a) Ag devices show a weak reverse bias dependence. A maximum EQE of 0.64% is obtained at the plasmon resonance under 1V revers bias (b) Au devices, on the other hand, are highly sensitive to the application of reverse biases as the EQE increases from 0.025% at short-circuit condition to 1.15% under the presence of -1V. The EQE of devices where the top metal electrode has been replaced by an ITO transparent conductive oxide is shown to eliminate possible midgap states in the titania as the source of visible photosensitization.

increasing reverse bias the EQE drastically increases to 0.61% and 1.15% for -0.5V and -1V. This clearly supports the idea that the hot-electron injection process is affected in this case by the modification of the electrostatic potential, in stark contrast to the case of Ag MIS devices. From a device point of view these findings suggest that Au MIS devices are better candidates for sensing (as quantum efficiency and responsivity increase with reverse bias), whereas Ag MIS devices are more suited to photovoltaic applications.

Once further evidence of the differences in the plasmo-electric conversion process of Au and Ag devices were found, we intended to obtain deeper understanding on the underlying mechanisms that are responsible for that. In the next section we describe the hot-electron injection and transport mechanisms in both configurations and propose a framework to account for the aforementioned differences.

3.3 Electronic transport in Ag/Au MIS devices

Herein we investigate the possible transport mechanisms that could account for the observed disparity in Ag and Au EQEs and their dependence with bias. The main relevant injection processes in MIS systems will be first introduced. On the basis of the experimental evidence we will finally postulate by elimination the most plausible transport channels for the hot-electron population into the semiconductor.

3.3.1 Transport mechanisms in MIS junctions

Depending on the nature of electron transport within a material, different current-voltage characteristics, temperature dependence or influence of the insulator in MIS devices can be observed (see Figure 3.11 and appendix B).

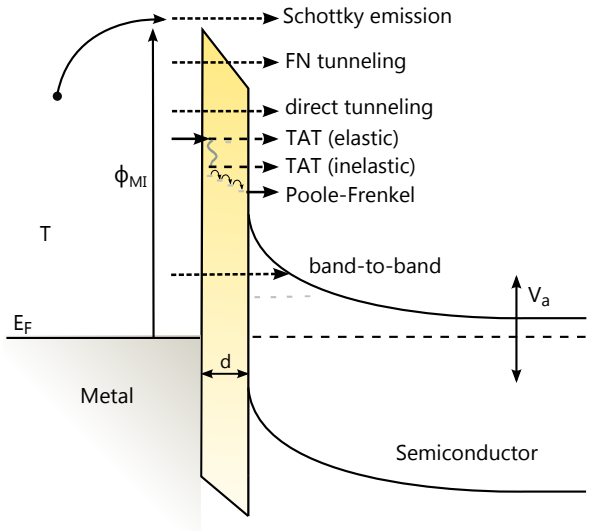

Figure 3.11: Tunnelling processes in MIS junctions. The different tunnelling processes in MIS junctions give rise to different electron transport characteristics, that can be inspected via current-voltage and or temperature spectroscopy, and with the influence of structural parameters such as barrier width (d).

Electron injection

Electron injection through a potential barrier occurs for energetic electrons that strike the interface with enough momentum to overcome the energy barrier. An accurate description will depend on the quantum tunnelling probability for each state, and on the population distribution and kinetics. In a general case it is given by,

$$J_{inj} = \int_0^\infty q v_\perp(E) N(E) f(E) T(E) dE \tag{3.2}$$

where $v_\perp$ is the carrier velocity transversal to the interface, $N(E)$ is the density of states,

$f(E)$ the energetic distribution and $T(E)$ the transmission coefficient. The transmission probability is calculated by solving the Schrödinger equation for a given barrier profile and typically applying the Wentzel-Kramers-Brillouin (WKB) approximation. Different types of tunnelling mechanisms will exist depending on the barrier profile and carrier density of states.

Tunnelling currents

To assess the possible transport mechanisms that determine the observed different hot-electron plasmoelectric effects (see Figure 3.11) we summarize in table 3.1 the dependence of J on T, V and barrier thickness d for different processes (for a more detailed description please see appendix B).

Table 3.1: Transport mechanisms in MIS junctions.

	Temperature (T)	Bias (V)	Thickness (d)
Fowler-Nordheim	none	$V^2 \exp(-b/V)$	$exp(-cd)$
Direct tunnelling	-	-	$exp(-cd)$
Poole-Frankel	$exp(-a/T)$	$exp(bV^{1/2})$	$exp(-cd^{1/2})$
trap-assisted (TAT)			
Schottky emission	$T^{-2}exp(-a/T)$	$exp(bV^{1/2})$	$exp(-cd^{1/2})$

3.3.2 Proposed transport mechanisms

Some considerations need to be taken into account before applying the aforepresented models. From a material's perspective, defects in the insulating layer, such as pinholes, would result in deviations in the observed currents and a different effective barrier height. Although for the thicknesses studied here the alumina films are expected to be continuous [116], imperfections for the thinnest barriers (0.5 nm) could introduce deviations. To account for that we measure several devices to allow for statistical analysis. From a fundamental point of view, the plasmonically generated hot-electron population will span along E_F and $E_F + \hbar\omega_p$, with a distribution that changes over time until all excited pairs relax by *e–e* or *e–ph* scattering. Since both the energy profile and the temporal evolution of this population are still subjects of intense debate in the community, full quantitative descriptions of hot-electron injection are still not within reach. In order to simplify, we assume in our case the broadly accepted picture an uniform distribution within $[E_F, E_F + \hbar\omega_p]$ (refs. [101,107,118,119]). Excited electrons in this interval with an energy excess of ΔE_γ over the Fermi level, must overcome an

effective barrier height of $\phi_\gamma = \phi_{MI} - \Delta E_\gamma$. Given this complexity, herein we aim at discovering the most relevant injection mechanisms for each MIS configuration.

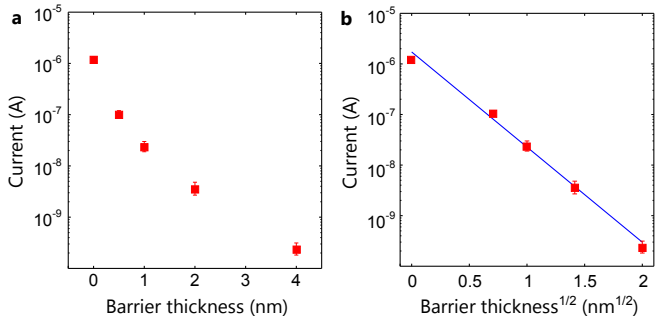

Figure 3.12: Study of transport in Ag MIS devices as a function of d. (a) $\ln J$ vs. d plot. The best linear fit yields a goodness of fit value of $\chi_{gf} = 0.90$ (b) In the case of $\ln J$ vs. $d^{1/2}$ the fit is considerably improved yielding $\chi_{gf} = 0.99$. This points towards the exclusion of Fowler-Nordheim tunnelling as the main injection mechanism.

Ag-based MIS diodes: Figure 3.12 illustrates the dependence of the photogenerated current as a function of the insulator thickness d. By inspecting the behavior of J with d we can differentiate between Fowler-Nordheim tunnelling and other types of transport. To do so we plot $\ln J$ vs d (panel a) and $d^{1/2}$ (panel b). Based on the obtained linear fits ($\chi_{gf} = 0.99$ vs. $\chi_{gf} = 0.90$ goodness of fit), we infer that FN is not the main tunnelling mechanism contributing to the photoelectric conversion process. Instead, either Schottky emission or trap-assisted-tunnelling (TAT) will be the dominant processes. In order to discern between them, temperature spectroscopy studies would be required (see table 3.1). The intrinsic temperature-dependence of the electronic transport through TiO_2 difficults however to differentiate these processes with this technique [120, 121]. We thus conclude that the injection of the plasmonic hot-electron population takes place *via* a combination of Schottky emission and TAT.

Au-based MIS diodes: the identification of the main hot-electron tunnelling mechanism in Au MIS devices is more evident. The photocurrent dependence with barrier thickness can be fitted by a Fowler-Nordheim process (see Figure 3.13), whereas the application of alternative models do not fit accurately follow the experimental data. A Fowler-Nordheim plot (Figure 3.13b) also show the expected $\ln(J)$ vs. $1/V$ linear behaviour. We can therefore conclude that the dominant transport mechanism underlying hot-electron injection in Au-based MIS devices is FN tunnelling. This is also in agreement with the observed strong bias dependence (Figure 3.10) as opposed to Ag-based MIS devices.

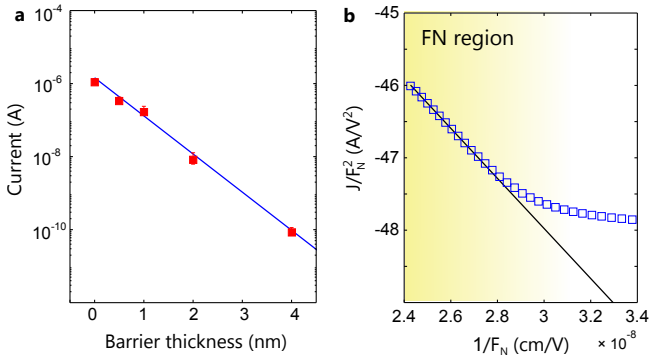

Figure 3.13: Study of transport in Au MIS devices as a function of d and applied bias for $d = 0.5$ nm. (a) $\ln J$ vs. d plot. The best linear fit yields a goodness of fit of $\chi_{gf} = 0.99$. In the case of $\ln J$ vs. $d^{1/2}$ the fidelity of the fit is considerably reduced to $\chi_{gf} = 0.84$. This suggest that Fowler-Nordheim assisted tunnelling is the main injection mechanism for Au MIS devices. (b) A Fowler-Nordheim plot reveals field-emission as the dominant tunnelling mechanism (linear region).

3.4 Conclusions

In this chapter we have introduced the use of a Schottky architecture to harvest plasmonic hot electrons. Quantum efficiencies of 4% could be achieved at resonance, but in the absence of a photovoltaic response. The crucial role of the metal-semiconductor interface for light energy harvesting applications was identified; a passivation scheme based on the atomically controlled deposition of alumina layers, resulting in a MIS structure, was demonstrated. This allows for the simultaneous achievement of J_{sc} and V_{oc}, enabling for the first time the conversion of solar energy to electricity in this architecture. The presence of the alumina layer was shown to modify hot-electron injection. By optimizing the thickness of the insulator layer a modest, yet proof-of-concept maximum PCE of 0.03% was demonstrated. The spectral tunability potential of plasmonic hot-electron devices was assessed by the use of different metals (Ag and Au), that display different plasmon resonances. The choice of metal has been shown to affect not only the optical properties of the structures but also the electrical. Different hot-electron injection mechanisms through the alumina layer were identified in the cases of Au and Ag. We found evidence supporting that tunnelling of hot-electrons in Ag-based MIS devices is mainly assisted by Schottky emission and trap-assisted-tunnelling. In Au-based devices, the primary transport mechanism is attributed to Fowler-Nordheim tunnelling.

4

Molecular Interfaces for Plasmonic Hot-Electron Photovoltaics

In the previous chapter we showcased the critical role of the metal-semiconductor interface for the photovoltaic performance of plasmonic hot electron devices. The inclusion of an ultrathin Al_2O_3 insulator layer allowed for the achievement of high V_{oc} and FF, prerequisites for energy harvesting, yielding to the demonstration of active plasmonic solar cells. This came however, with a reduction in J_{sc}, and an overall mediocre PCE. Moreover, this inorganic based approach limits the roadmap of plasmonic hot-electron solar cells for it does not allow the simultaneous control over V_{oc} and J_{sc}, an important step required in exploiting the exotic physics of these devices towards reaching higher performance. Instead, a more versatile approach can be envisaged through the exploitation of molecular species in self assembled monolayers [122]. Molecules, unlike inorganic high bandgap semiconductors, possess a plurality of structural parameters that can be tuned in these systems: the length of the molecule, the conjugated or aliphatic character and the end-functional groups that serve to strongly bind on a given surface and passivate electronic defect states [86, 122–129]. Not to exclude also their solution processability which is a significantly lower cost manufacturing process

compared to atomic layer deposition. In this chapter we exploit the unique properties of self-assembled monolayers (SAMs) of molecular species in order to tune the electronic properties of the molecular interface in a plasmonic hot-electron photovoltaic device. This may lead to a drastic improvement in hot-carrier injection and the simultaneously control of J_{sc} and V_{oc}. We demonstrate that the photovoltaic performance of hot-electron devices can be modified in a twofold manner, by either adjusting the molecular length or their head-functionalization to control J_{sc}. In addition, the manipulation of the dipole of the molecules that constitute the SAM act to leverage V_{oc} . A maximum PCE of 0.11%, over a three-fold improvement compared to Al_2O_3, is reported, with high open-circuit voltages and EQEs in excess of 5% at the plasmon resonance peak.

4.1 Device structure

The solar cell structure is shown in Figure 4.1a. Briefly, a titanium dioxide nanocrystalline film electron transport layer is deposited on top of a transparent conductive oxide. The cross sectional scanning electron micrograph (SEM) reveals that the Ag follows TiO_2 corrugations, of the order of 10-80 nm, and enables the coupling of incident light to Ag plasmonic resonances. As shown in the previous chapter, for untreated, bare TiO_2 films, the presence of surface states due to the existence of dangling bonds and off-stoichiometry defects results in a charge localization and a modification of the surface potential that prevents the formation of a built-in potential in the eventual contact with the metal electrode (Figure 4.1b) [130]. In this section we present the use of SAM as a mean to passivate the TiO_2 surface. For that purpose we select a set of molecules with compatible functional groups to build-up a SAM over its surface (Figure 4.1c) [125,131,132]. We chose carboxylic acid (R-COOH) functionalized molecules, a commonly used binding group to TiO_2 [133–135].

SAM adsorption: the adsorption of an oleic acid (OA) ($C_{18}H_{36}O_2$) SAM to the TiO_2 has been monitored with Fourier Transform Infrared spectroscopy (FTIR) by looking at the different vibrational characteristic of the molecules (see Figure 4.2). The difference in the symmetric and asymmetric stretching frequencies of the deprotonated carboxyl group has been reported to depend on the -COOH binding mode [133]. In our case this difference, on the order of 100 cm^{-1}, suggests a bidendate chelating binding mode of COOH to TiO_2. In this way the majority of $C_{18}H_{36}O_2$ molecules will bind to a Ti atom in the TiO_2 slab. After substrate functionalization the most critical step in the fabrication of SAMs junctions is the deposition of the top electrode, as

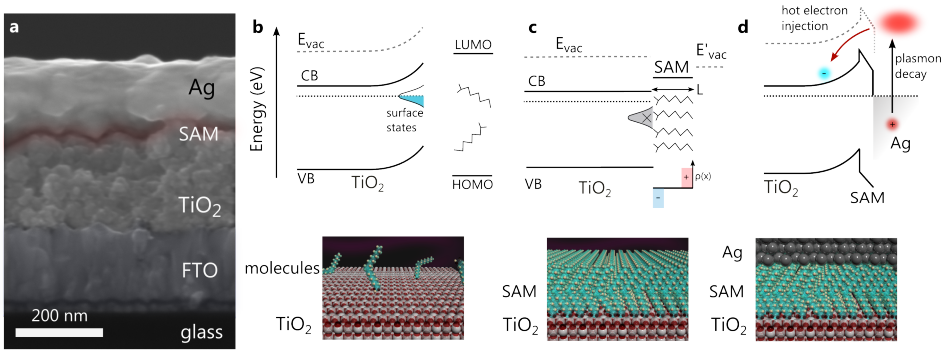

Figure 4.1: Molecular interfaces for plasmonic hot electron photovoltaics. (a) Cross-sectional SEM of a plasmonic hot-electron solar cell, comprising a transparent conductive bottom electrode, a high bandgap semiconductor layer (TiO_2) which is covered by a molecular self-assembled monolayer (SAM). An Ag electrode is used to harvest the hot-electrons generated by plasmonic damping. Without the presence of the SAM (b) TiO_2 defect states create a space charge region which would result in Fermi level pinning and no photovoltaic effect would result upon contact. The SAM caters for the passivation of these detrimental states and the simultaneous control over the interface conformation and charge distribution. (d) This ultimately allows for the control over the photovoltaic figures of merit of the plasmonic hot-electron devices.

it can compromise the integrity of the underlying molecular layer. The influence of the deposition conditions has been widely studied in other systems [123, 136–139], reporting soft electrode transfer or indirect evaporation as the less harming methods of metal deposition onto the SAM. In our case, we have found that direct metal evaporation is capable of maintaining the quality SAMs for low enough deposition rates and temperatures (see appendix A for more details). In order to assess the integrity of the OA-metal buried interface we first cross-compared the molecule vibrational modes of a TiO_2-SAM before and after the deposition of 3 nm of Ag measured by FTIR in an attenuated total refelection configuration [137]. The coincidence of the characteristic stretching frequencies for COO-, CH_2 and CH_3 suggest that the SAM has not been substantially modified after electrode deposition. The bridging mode of the SAM constituent molecules remains bidendate chelating (Figure 4.2). This point was further confirmed for the final device structure by comparing the FTIR spectra of a bare TiO_2-OA device with the signatures obtained by plasmon-enhanced Raman spectroscopy measurements once the final electrode thickness had been deposited (Figure 4.3a). The coincidence of the (CH_3) and (CH_2) stretching frequencies in both cases indicates that the molecular backbone and exposed end has not been altered. The potential presence pinholes within the SAM could not be quantified due to the intrinsic roughness and grain size of the TiO_2 substrates employed for our solar cells, which are on the order of

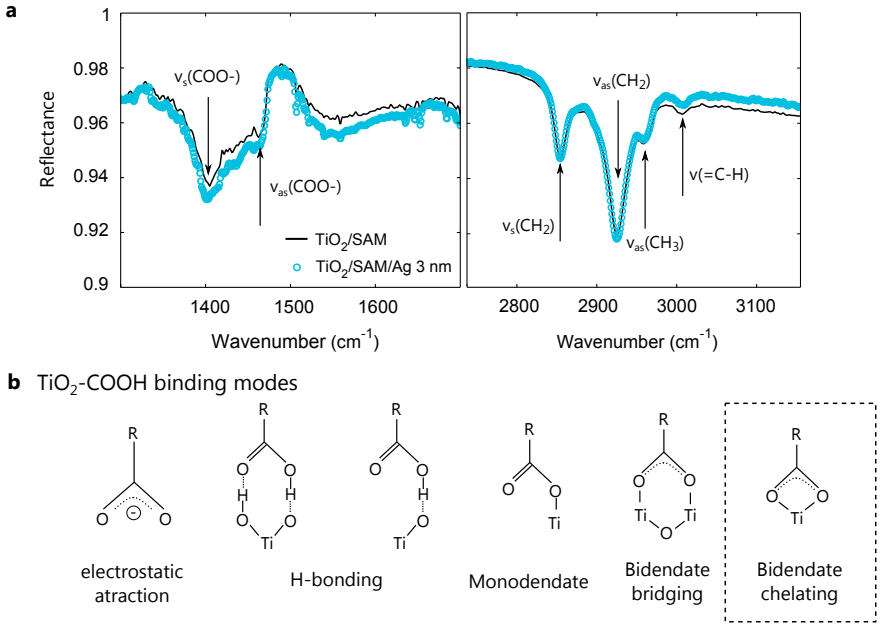

Figure 4.2: Bridging mode and integrity of SAM after metal deposition. (a) FTIR reflectance spectra of a TiO_2/SAM sample before (solid line) and after (circle marked dots) the deposition of an ultrathin Ag layer (3 nm). (b) Possible molecule binding modes. The difference in the symmetric and asymmetric stretching frequencies of the deprotonated carboxyl group (of the order of 100 cm^{-1}) suggest a bidendate chelating binding mode of COOH to TiO_2 [133]. In this way each $C_{18}H_{36}O_2$ molecule will bind to a Ti atom in the TiO_2.

80 nm. Even in the presence of SAM defects, the electronic properties of the interface can be dominated by the properties of the SAM provided those defects are scarce and small enough [**?**]. The systematic correlation observed between SAM properties such as length and dipole with the figures of merit of our solar cells reported along the subsequent sections suggests that the presence of pinholes do not dominate or limit the performance.

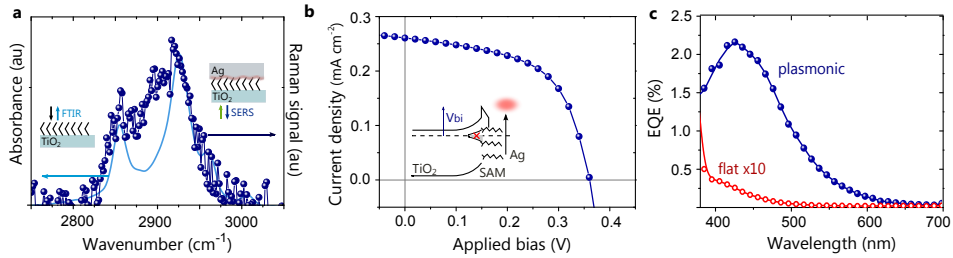

Figure 4.3: Molecular interfaces to passivate interfacial states. (a) Vibrational signatures of the grafted oleic acid ($C_{18}H_{36}O_2$) self-assembled monolayer (SAM) before and after the final metal electrode deposition. (b) Current-voltage characteristics under simulated solar illumination AM 1.5G showcasing the photovoltaic performance of these devices due to midgap states passivation. (c) The EQE of these devices illustrates that the dominant photocurrent generation mechanism is the injection of plasmonic hot electrons from the Ag metal electrode.

Photovoltaic response: the photovoltaic performance of a representative OA device is shown in Figure 4.3b, yielding a V_{oc} of 0.36V. The average power conversion efficiency of these devices is 0.05%, whereas alumina devices show an average PCE of 0.02% for the optimized configuration. The superior performance of this approach stems from the higher J_{sc} (0.264±0.03 versus 0.14 mAcm^{-2}) of these devices and points towards a more efficient hot-electron injection from the plasmonic electrode. The EQE for an OA representative device is shown in Figure 4.3c. The spectral response is dominated by the plasmonic character of the textured electrode with a maximum value of 2.1% at resonance. The flat unpatterned control reference shows on the other hand no significant contribution in the visible region of the spectrum.

4.2 Molecular length to control hot-electron injection

Once the ability of the SAMs to passivate detrimental interfacial states, which lead to photovoltaic response in TiO_2-metal plasmonic structures, has been demonstrated, we

proceed to study the effects of the SAM on the electronic properties and hot-electron injection mechanisms. For this purpose we chose a set of carboxyl aliphatic chains of different lengths with the form of R-COOH, in such a way that the number of carbons and saturation of the R chain is modified. The COOH functional group binds to the TiO_2 surface as illustrated for the OA case, exposing the unfunctionalized methyl end to the Ag metal electrode. The adhesion of the different SAMs to the TiO_2 was verified by FTIR for all molecules (see Figure 4.4). The thickness of the resulting SAM modifies charge transport and injection across the nanoscopic junctions, thus offering the possibility to modulate hot-electron injection efficiency (i_{eff}) (Figure 4.5b). The EQE for the different molecules is shown in Figure 4.5c, demonstrating the correlation of the injection efficiency with the length of the molecules. The longest molecules (such as stearic acid, with 18 carbons and an approximate length of 22Å) yield the lowest EQEs, around 2%, whilst the maximum EQE (in excess of 5%) is reached with the shortest length molecule (valeric acid (VA), 5 carbons and approximately 6Å). The same trend is observed for the short-circuit current (Figure 4.5d), which increases from 0.26 $mAcm^{-2}$ to 0.44 $mAcm^{-2}$ (average values). A maximum PCE of 0.10% and J_{sc} = 0.50 $mAcm^{-2}$ are obtained for VA. The relevant figures of merit of this set of devices are shown in table 4.1. The EQE for an Au electrode with the same SAM is also shown in Figure 4.6, showcasing the different contribution in the spectrum from the Au plasmonic resonance and over an order of magnitude improvement compared to the best inorganic interfaces [130].

Table 4.1: Average photovoltaic figures of merit for aliphatic carboxylic acids. Errors represent standard deviations. The maximum PCE is 0.10% for valeric acid.

	Stearic acid	Oleic acid	Caprylic acid	Valeric acid
J_{sc} ($mAcm^{-2}$)	0.257 ± 0.01	0.264 ± 0.03	0.391 ± 0.04	0.440 ± 0.03
V_{oc} (V)	0.28 ± 0.02	0.34 ± 0.02	0.33 ± 0.03	0.41 ± 0.03
FF	0.53 ± 0.02	0.54 ± 0.04	0.44 ± 0.01	0.47 ± 0.02
PCE (%)	0.042 ± 0.004	0.050 ± 0.006	0.056 ± 0.005	0.083 ± 0.005

Based on table 4.1, there is a correlation between the molecular length and the V_{oc}. The observed trend would be *a priori* unexpected as the dipole moment of the molecules, dominated by the COOH functionality, is very similar in all cases (around $2.9D$). This trend could be accounted for by a different packing, orientation and/or density of the molecules within the SAM as a consequence of differences in steric hindrance. The complexity of the nanostructured interface does not allow for facile characterization of those effects, and further characterization would be required to fully elucidate the

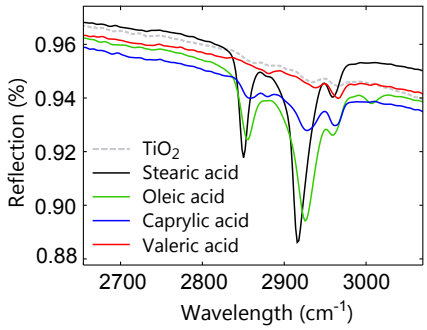

Figure 4.4: Bridging of alkanoic acids of different lengths to TiO_2. CH_x and C−H stretching frequencies of studied carboxylic acid aliphatic chains after incubation with TiO_2 substrates.

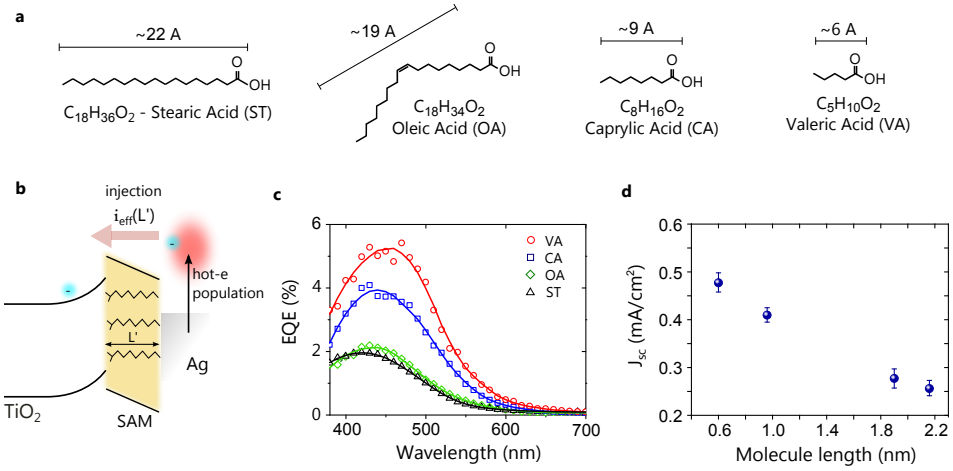

Figure 4.5: Molecular length to control hot-electron injection efficiency. (a) The length of the SAM constituent molecules will determine its thickness, and can therefore be controlled by selecting a proper set of molecules. As a consequence, the hot-electron injection efficiency (b) is expected to change as the Ag-TiO_2 distance diminishes. The EQE increases as the length of the SAM decreases, from 18C (stearic acid) to 5C (valeric acid) yielding a maximum value beyond 5%. (c). This is correlated with the increase in short-circuit current (d), from 0.25 up to 0.475 $mAcm^{-2}$.

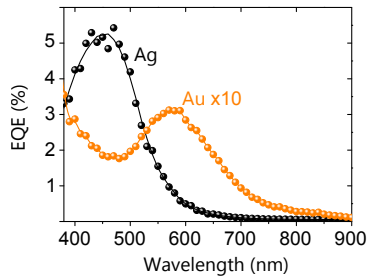

Figure 4.6: Molecular length to control hot-electron injection efficiency. EQE for silver and gold devices over a valeric acid SAM-TiO_2 substrate. The EQE of gold has been rescaled for clarity.

observed phenomena. In order to simplify these considerations, we move to SAMs composed of structurally similar conjugated molecules.

4.3 Molecular dipoles to control open-circuit voltage

To get further insights into the ability of the SAM to modify the open-circuit voltage in hot-electron solar cells, we chose to study a set of molecules with fixed structural parameters but different chemical functionalities (HOOC-C6H4-X), such that their dipole moment can be tuned independent of their length, by the selection of different functional species at both molecular ends. The electrostatic potential induced by the molecule's dipole results in a local modification of the charges across the interfaces and the vacuum level, thus enabling for the nanoscale control over the band alignment and electrostatic fields along the interface (see Figure 4.7a). In this way we can expect the barrier and the injection to be dominated by the dipole moment as described in equation 4.1,

$$qV_{oc} = W_{Ag} - (\xi_{sc} + qV_n - q\phi_{SAM}) \tag{4.1}$$

Where W_{Ag} is the metal workfunction, ξ_{sc} is the semiconductor electron affinity, qV_n is the energy difference from the Fermi to the semiconductor conduction band and $q\phi_{SAM}$ is the contribution from the SAM. The latter can be further written as,

$$q\phi_{SAM} = \frac{N\mu\cos(\theta)}{\epsilon_0\epsilon_r} \tag{4.2}$$

and depends on the surface density of dipoles (N), their magnitude (μ) and orientation angle (θ). Therefore, the open-circuit voltage can be increased by selecting a set of molecules such that, once attached to the TiO_2, may lower the local vacuum level in the other end (i.e. a negative dipole moment), resulting in an increase of the net barrier after contact [140, 141]. The results are shown in Figure 4.7b. Conjugated molecules with lower dipole moments (benzoic acid and 4-mercaptobenzoic acid) yield consistently lower open-circuit voltages (0.26V and 0.32V respectively). Molecules with higher dipole moments, such as 4-aminobenzoic (ABA) acid and 4-hydroxybenzoic acid (HBA) yield on the other hand higher V_{oc} . There is a linear dependence of the obtained V_{oc} with individual molecules dipole moment, suggesting that both the density of dipoles and orientation angle is similar in these SAMs. The rate of change of V_{oc} with dipole moment, calculated from the best linear fit, yields a value of 104 mV/D. A maximum PCE of 0.11% with a V_{oc} of 0.56V is obtained for HBA. The relevant figures of merit of this set of devices are summarized in table 4.2.

Table 4.2: Average photovoltaic figures of merit for conjugated carboxylic acids: 4-mercaptobenzoic acid (MBA), 4-aminobenzoic acid (ABA), benzoic acid (BA), and 4-hydroxybenzoic acid (HBA). Errors represent standard deviations. The maximum PCE is 0.11% for HBA.

	BA	MBA	ABA	HBA
J_{sc} (mAcm^{-2})	0.268 ± 0.020	0.320 ± 0.020	0.440 ± 0.040	0.484 ± 0.035
V_{oc} (V)	0.273 ± 0.040	0.249 ± 0.020	0.253 ± 0.020	0.357 ± 0.030
FF	0.46 ± 0.06	0.27 ± 0.03	0.42 ± 0.03	0.53 ± 0.03
PCE (%)	0.035 ± 0.008	0.023 ± 0.004	0.043 ± 0.008	0.091 ± 0.010

In addition to the control of the open-circuit voltage in these devices, through the SAM interface modification an additional feature of simultaneous control over the hot electron injection process and subsequently of J_{sc} has been identified. Figure 4.7c shows the EQE peak (maximum EQE at resonance) dependence on the chemical species of the molecules that face the metal electrode. Different moieties lead to an increase in EQE from 2.6% (MBA) up to 4.5% (HBA), corresponding to 0.273±0.040 to 0.440±0.03 mAcm^{-2}. This reveals a trend of increasing EQE with the binding energy of the exposed chemisorbed functional groups to the Ag electrode [142]. We hypothesize that

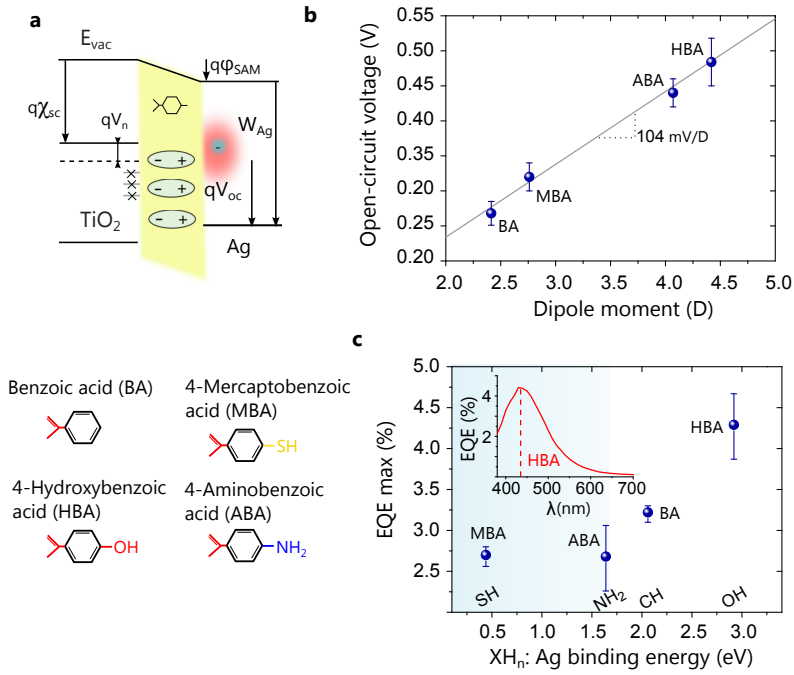

Figure 4.7: Molecular dipoles to control open-circuit voltage.(a) The electrostatic potential of the SAM can modify the local vacuum level also changing the effective barrier after contact. The resulting open-circuit voltage can therefore be tuned by selecting molecules of different dipole moments. (b) There is a clear correlation of the V_{oc} with molecule's dipole, which enables the linear control of the V_{oc} with a rate of 104 mV/D. (c) The injection efficiency can also be controlled by modifying the functional group chemisorbed to the metal electrode.

this can be attributed to a different SAM/Ag interface morphology due to the different interaction of the exposed moieties with the evaporated metal atoms [143–146]. On the other hand, a stronger interaction of the metal with the SAM, might result in a higher density of tunneling states therefore promoting hot-electron injection [147]. Further understanding of this functionality–provided for example by time-of-flight secondary ion mass and x-ray photoelectron spectroscopies, in combination with quantum chemical simulations–would open exciting possibilities in controlling hot-electron injection for active plasmonic devices.

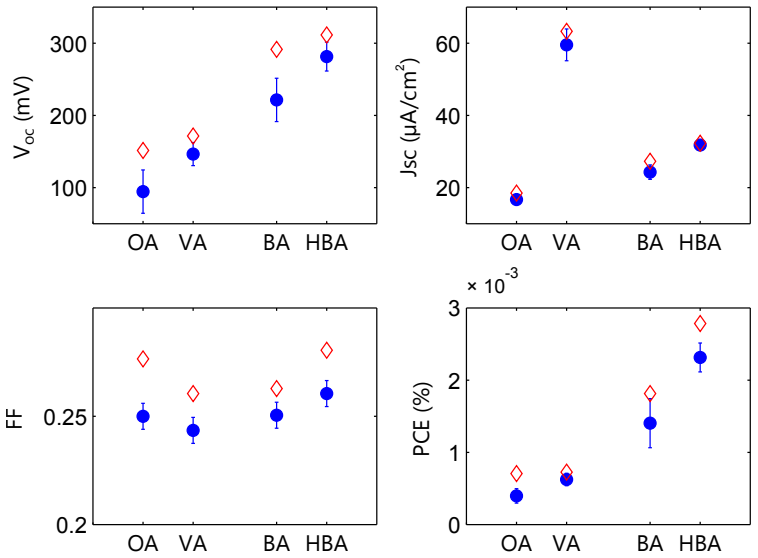

Figure 4.8: Summary of Au devices performance. Statistics for the relevant photovoltaic figures of merit of a set of molecules with Au electrodes. The trends discussed in the main text (i.e. change of J_{sc} and V_{oc} with molecule parameters) are conserved in the case of gold, although the overall performance is lower due to the lower J_{sc} associated with the molecule barrier [130].

We note that the aforementioned trends in solar cell performance are also maintained for the case of gold electrodes (see Figure 4.8), thus enabling molecular interfacial control as a promising generic tool for hot-electron plasmonic optoelectronics.

4.4 Conclusions

In summary, we have shown that SAMs make a versatile platform to tune the metal-semiconductor interface in order to improve the photovoltaic response of plasmonic hot-electron solar cells. Molecular linkers can serve to passivate localized midgap states

that are detrimental to the photovoltaic performance of these devices also offer a powerful set of extra functionalities to tune the optoelectronic properties that go beyond the capabilities provided by inorganic layers. We have shown that the injection efficiency can be tailored by morphological or electrochemical factors: either the length or the chemical moiety of the SAM/metal interface can be used to modulate the EQE. By doing so, we report the highest J_{sc} and EQE (over 5%) in solid state plasmonic hot-electron solar cells. We have also shown that, on top of the ability to improve and control electron injection, SAMs allow for the concurrent tuning and optimization of the open-circuit voltage by selecting a set of molecules with a proper dipole moment (at a rate of 100mV/D). This allows for the simultaneous achievement of high open-circuit voltages (0.56V) and fill-factors (0.58) and record photovoltaic power-conversion efficiencies of 0.11%. This approach, together with a wider spectral plasmonic response, can lead to higher PCE in the future.

The use of molecular layers to modify interfacial properties also opens up exciting avenues for hot-electron photodetection, where the height of the Schottky barrier, which is the ultimate limiting factor determining up to what extent IR light could be harvested [108, 148], can now be tailored to specific values. Further functionalities could be envisioned by studying the interaction of the metal hot electron population with particular molecular linkers to exploit coherent and/or even resonant resonant transport [118, 149–151], which might find application in molecular electronics [152].

5

Hot-Carrier Plasmonic Crystal Photodetectors

The possibility to fabricate hot carrier based devices with tailored spectral response, is exciting for solar energy harvesting [85, 87, 106, 130, 153], and for visible or infrared detection [85, 94, 99, 107, 108, 130, 154]. However, the fabrication of these devices has so far relied on nanoparticles [154], nanoantennas [101, 107] or gratings [108] to excite either localized or surface plasmons. Such metallic nanostructures are fabricated with costly and time-consuming lithographic processes, which greatly limit their potential for large-area, high-throughput manufacturing, required for realistic applications. In order to fully exploit hot electron based optoelectronics, a platform capable of combining the exotic spectral capabilities provided by plasmonic systems with large scale manufacturing and high performance has yet to be achieved. In this chapter we present the first implementation of a large-area, low-cost quasi-3D plasmonic crystal (PC) for hot electron photodetection, showcasing multiband selectivity in the VIS-NIR and unprecedented responsivities up to 70 mA/W. The PC facilitates the excitation of a wide variety of propagating, localized and hybrid plasmon resonances, which ultimately decay in the hot carriers exploited herein. Our fabrication strategy, which relies on

soft nano-imprinting lithography (NIL) [155], paves the way for the implementation of plasmonic hot-electron technology at a large-scale for a vast variety of optoelectronic devices. The chapter is organized as follows. First, the NIL fabrication scheme together with our proposed plasmonic crystal architecture is introduced. The next sections comprise the demonstration of the spectral tunability offered by our architecture and the analysis of its origin. We conclude by evaluating the optoelectronic performance of our PC hot-electron device for sensing.

5.1 Plasmonic crystal structure

For plasmonic excitation in metals the momentum mismatch between the bound surface plasmon and the free propagating incoming photon has to be taken into account [156]. This additional momentum can be provided by scattering of nanoparticles, a prism or a diffraction grating. The latter configuration is advantageous since the periodicity of the architecture determines the frequencies at which surface plasmon polaritons (SPPs) are excited, irrespective of the plasmon frequency of the metal [157,158]. This is the case of the plasmonic crystals, in reference to their dielectric counterparts (photonic crystals): metallic architectures with periodically organized motifs [159]. Plasmonic crystals can sustain a wide variety of plasmonic resonances (propagating and localized) that can further couple with each other to produce strong hybrid resonances [160,161]. In this chapter we seek to exploit the complex and design-dependent dispersion relation of the plasmonic crystal architecture to fabricate a tunable and broad band multispectral VIS-NIR hot-electron based large-area photodetector.

Device fabrication: the plasmonic crystal structures were fabricated following a soft nano-imprinting lithography technique. This method allows for a facile integration with large scale manufacturing processes, such as roll-to-roll [105]. The fabrication process is depicted in Figure 5.1. A polydimethylsiloxane mold (PDMS, 10:1 Sylgard 184), replicating a square array pattern from a silicon wafer (AMO gratings), was used as "printing stamp". A UV photocurable epoxy (SU8, Microchem), was spin-cast on top of ITO-coated substrates (Stuttgart University) to make 500 nm thick films. Samples were wetted with ethanol and imprinted with the PDMS stamp. Patterned resists were UV cured after imprinting to improve their mechanical stability ($\lambda = 360$ nm, 15 min), through a spatial mask defining squared imprinted regions of 9 mm^2. Once the resists were exposed and developed, 40 nm of ITO are sputtered onto the substrates using an AJA sputtering system without masking, so the sputtered ITO is electrically connected to the commercial ITO coated substrate. Finally, a 90 min annealing step at 200°Cis

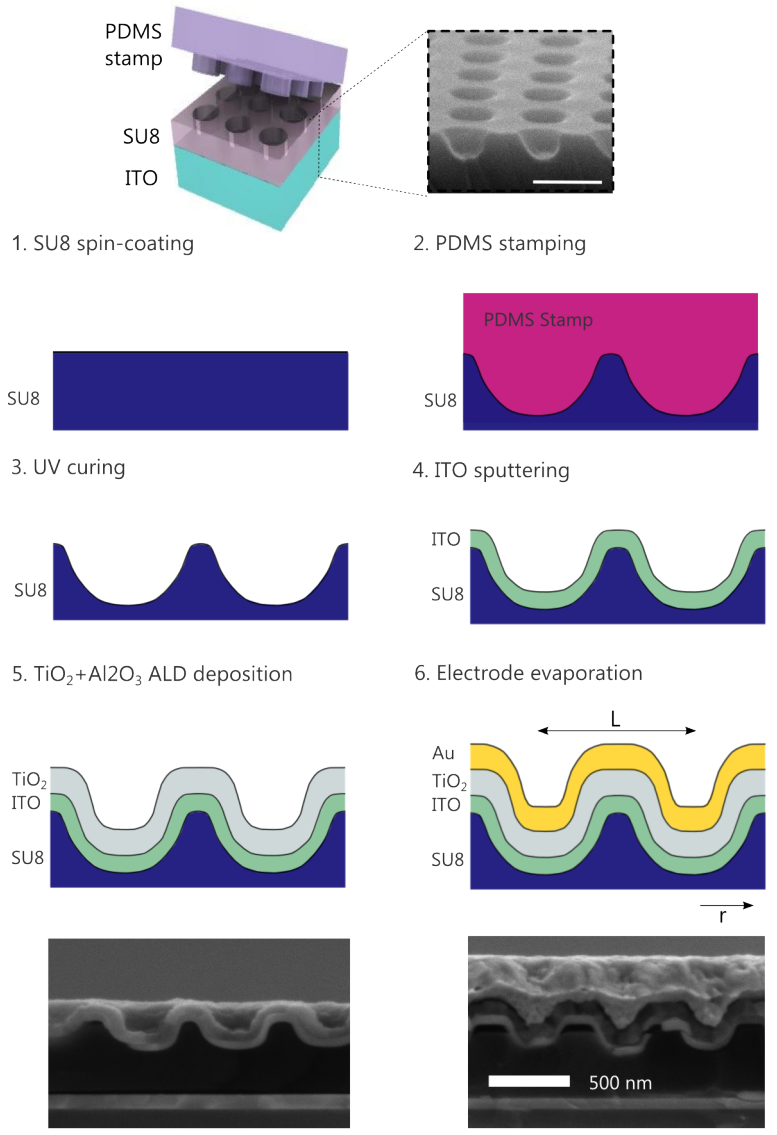

Figure 5.1: Plasmonic crystal NIL fabrication process. A commercial stamp with predefined lattice parameter, radius and pillar depth is used to shape a SU8 elastomer. The resist is baked to attain mechanical stability before the deposition of the subsequent material layer processes: (1) sputtering of ITO, (2) ALD deposition of TiO_2 and Al_2O_3, (3) Au evaporation. SEM cross-sectional images are shown for the last two processing steps.

carried out under inert atmosphere to improve the conductivity of ITO. On top of these substrates, devices are built by first depositing 60-80 nm of TiO_2 and 0.5 nm of Al_2O_3 (via atomic layer deposition, for detailed parameters see appendix A. The top metal electrode consists of 200 nm of evaporated gold.

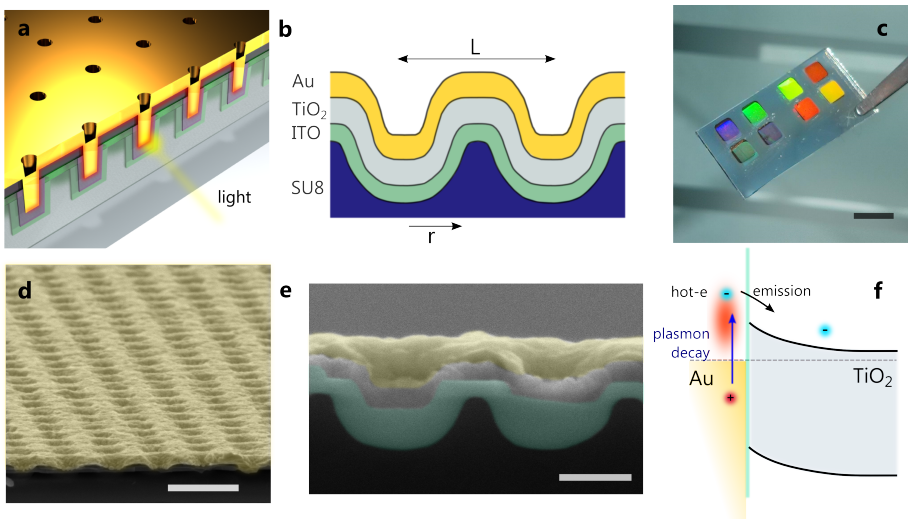

Figure 5.2: Device architecture and principle of operation. (a) Representation of the plasmonic crystal photodetector. Light impinges from the bottom (ITO/glass) exciting resonant modes responsible for the hot electron generation. (b) Schematic of the device architecture: a square array of cylindrical voids in photoresist is coated with 40nm of ITO, followed by 60 nm of TiO_2 and 150 nm of Au. Different geometries are fabricated varying both lattice parameter (L) and / or the cylinder radius (r). (c) Photograph of a substrate containing eight 9 mm^2 devices; the reflected colors are indicative of the nanostructured metal electrodes. Scale bar is 1 cm. (d) 45°angle view SEM image of the periodic arrays. Scale bar is 2 μm. (e) Cross sectional SEM artificially colored to portray the different layers of the architecture. Scale bar 400 nm. (f) Schematic representation of the photocurrent generation process after light excitation: hot electrons derived from plasmonic damping are emitted over the Au/ TiO_2 Schottky barrier into the TiO_2 conduction band.

Device architecture: the resulting plasmonic crystal photodetector is represented in Figure 5.2. Large-area, 9 mm^2 devices with different geometric characteristics were fabricated (see photograph in Figure 5.2c). Different intense colors are observable with the naked eye, as a result of the different resonances of the crystals. Their optical properties can be precisely tuned with the lattice parameter (L), radius (r), cylinder depth or TiO_2 thickness. A SEM image (45°angle) of the metal film (Figure 5.2d) illustrates the periodic arrangement of the plasmonic crystal. The constituting ITO, TiO_2 and Au layers of the architecture can be distinguished in the cross-sectional SEM

image in Figure 5.2e. The optoelectronic operation of the photodetector is based on the interaction of the corrugated metal film with incident light. Photons impinging from the ITO side (Figure 5.2a) excite several plasmonic resonant modes in the metal, which ultimately result in the creation of electron-hole pairs in the metal through Landau damping (Figure 5.2f). This rising hot electron population can then be collected by the Schottky barrier at the Au-TiO_2 interface, resulting in a photocurrent ultimately dictated by the plasmonic crystal resonances. [107]

5.2 Multispectral response

We herein evaluate the spectral response of the responsivity at short-circuit conditions for different plasmonic crystal structural parameters (Figure 5.3). The top panel corresponds to $L = 550$ nm and $r = 200$ nm. Two overlapping resonances provide a broader peak in the 500 to 700 nm region. Less intense features appear at 750 and 900 nm. This is in contrast with the observed responsivity spectra for randomly textured Au electrodes, solely dictated by material properties, and that of the flat references. As the optical properties of the plasmonic crystal are strongly influenced by r and L, we intended to observe a different spectral response when changing these parameters. Photodetectors with different lattice parameters (450 nm and 550 nm) and/or radius (200 nm and 150 nm) were fabricated using NIL stamps with predefined features. Reducing the cylinder radius by 50 nm already results in a noteworthy modification of the responsivity spectrum (Figure 5.3b), enhancing NIR features and shifting resonances in the visible. This demonstrates the impact a tiny variation in r has on the spectral response. The modification of the lattice parameter is also expected to strongly modify the available modes. Reducing L from 550 nm to 450 nm results in a reconfiguration of the spectral response. A general shift towards shorter wavelengths is obtained for the three main resonances, consequence of the larger wave-vectors provided by the lattice. The impact of the PC architecture over the responsivity spectrum showcases the suitability of this platform for tailored photodetection, since both the number of resonances, their intensities and positions can be modified across the VIS-NIR. This is, to our knowledge, the first demonstration of a solid state plasmonic photodetector compatible with large-scale manufacturing processes.

To gain insight into the underlying mechanisms that give rise to this multiresonant response, the optical absorption of a nanostructured device ($r = 150$nm, $L = 450$nm and 60nm of TiO_2) was calculated with FDTD simulations (see appendix A for simulation details) and compared to the experimental responsivity. The simulated absorption faithfully reproduces the measured responsivity spectrum, matching the position of the

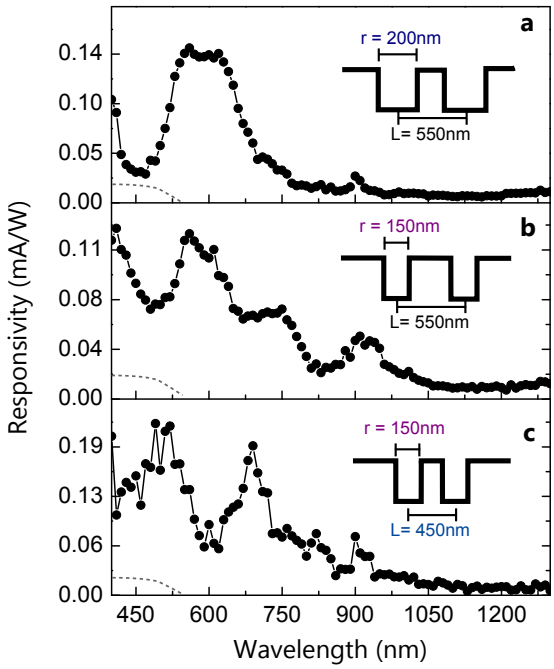

Figure 5.3: Experimental responsivity of a plasmonic crystal based photodetectors for different structural parameters measured at short circuit conditions: (a) $r = 200$ nm and $L = 550$ nm; (b) $r = 150$ nm and $L = 550$ nm and (c) $r = 150$ nm and $L = 450$ nm. The spectral selectivity, number of resonances, their intensities and positions can be modified with these parameters. Flat references are shown for comparison (grey-dashed line).

515 nm, 714 nm and 886 nm resonances (Figure 5.4a). Inspection of the field intensity profiles associated to these resonances can provide information about the nature of the plasmonic modes that are excited within the structure (Figure 5.4b-c, top). Absorption rate profiles, relevant to hot-electron generation (Figure 5.4b-c bottom), can give insights on the contribution of each mode to the resulting photocurrent (Figure 5.4b-c, bottom).

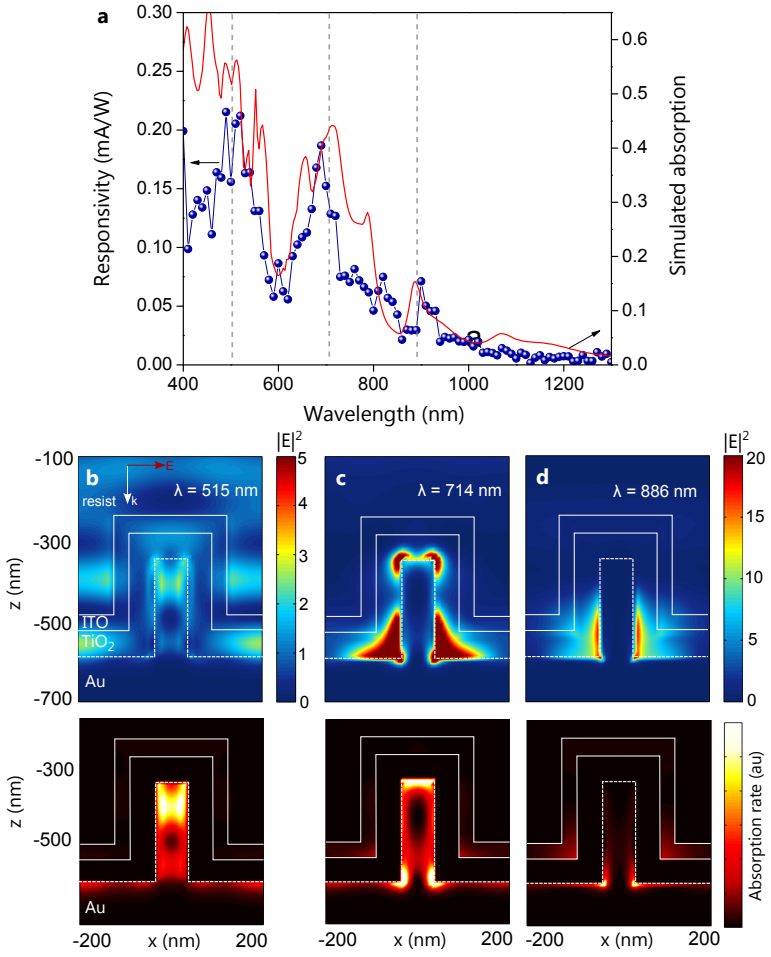

Figure 5.4: Responsivity spectra and its correlation with the optical response of the plasmonic crystal. (a) Responsivity (scattered points) versus the FDTD simulated absorption in the gold (red line). The electric field distribution (top) and absorption rate (bottom) within the plasmonic architecture at (b) λ_1= 515 nm (c) λ_2 = 714 nm and (d) λ_3 = 886nm illustrating the different nature of the resonances, from Mie-Bragg (b) to Localized- Bragg (c) to Bragg SPP (d) modes.

λ_1 = 515 nm: the electric field (Figure 5.4b, top) spreads within the TiO_2 layer,

the photoresist and penetrates into the metal plate and cylinder. The corresponding absorption is found within the volume of the gold pillar (Figure 5.4b, bottom). The electric field profile in this case suggests a complex interplay between the plasmons excited by the grating periodicity and the bulk absorption of the Au pillars (the interband transition in gold starts at 2.4 eV) [161]. In this frequency range, light can penetrate within the gold cylinder (an architecture with $r = 150$nm has an Au cylinder with 50 nm radius, considering the ITO and TiO_2 coatings), allowing the excitation of lossy modes inside the cylinder. The divergence of simulated absorption and experimental responsivity below 450 nm can be ascribed to a less efficient hot-electron injection from the pillar-core compared to its surface [162,163], as the electron mean free path is of the order of 15-20 nm for these wavelengths. Gold interband transitions, relevant for this frequency range, are also known to be less efficient in hot-electron injection due to the depth of Au *d*-band levels [163, 164].

$\lambda_2 = 714$ nm: this longer wavelength resonance (Figure 5.4c) presents on the other hand an electric field distribution strongly bound to the Au/TiO_2 interface. High intensity nodes are identified at the base and at the top of the metal pillar, suggestive of SPP interference leading to very high localization.

$\lambda_3 = 886$ nm: for this resonance, the field is more concentrated along the vertical facets of the metal cylinder. It is important to note that the corresponding spatial distribution of the absorbed photons is more intense at the interface with the titanium dioxide for the latter two plasmonic resonances, thus facilitating the injection of the hot electrons into the oxide due to the proximity with the interface.

5.3 Mode hybridization and tunability

In this section we study in detail how the different structural parameters of the PC affect its spectral response. By inspecting the influence of the lattice parameter we clarify the origin of the different resonances, differentiating between localized, surface, and hybrid modes. The effect of the radius, pillar depth, and semiconductor material and thickness is also analyzed.

5.3.1 Influence of the lattice parameter

A deeper insight in the physical origin of the three resonances described before can be obtained by comparing the evolution of the 2D absorption map (wavelength versus lattice parameter L) when modifying different aspects of the plasmonic crystal structure (Figure 5.5). These 2D maps help identify the plasmonic modes that depend only on

the diffraction condition imposed by the lattice parameter, therefore called Bragg SPP modes, the ones that are L-invariant, and the regions where both modes are coupled [160, 161, 165]. Several of these 2D diagrams are analyzed in what follows. Firstly, the effect of the ITO absorption towards longer wavelengths is revealed when the 2D absorption map is computed, considering only the real part of the refractive index of the conductive oxide (Figure 5.5a-b). When the losses in the ITO are disregarded, the optical response of the architecture extends deeper into the NIR region with increasing lattice parameter. Secondly, a simplified architecture is considered, removing the glass, resist and ITO scaffold, which only leaves a bare gold-titania periodic interface (Figure 5.5c). The number of plasmonic modes is in this case dramatically reduced, implying that many of the modes are excited from the multilayered grating architecture that constitutes our plasmonic crystal. The different corrugated interfaces (resist-ITO, ITO-TiO_2, TiO_2-Au) effectively provide several subsequent gratings of similar center to center distances, but different radii, refractive indexes and fill factors, launching different SPPs.

Finally, we intend to distinguish between the horizontal, L-independent bands observed together with the clear Bragg-SPPs. The first correspond to localized plasmons and will depend on the gold nano-pillar geometry. The latter are associated with delocalized propagative waves along the metal-semiconductor interface. When both modes overlap, strong absorption enhancement and broadening is observed, as is the case of the point $(L,) = (500\text{nm}, 714\text{nm})$. The excitation channels derived from a pure photonic grating on a flat metal film are depicted in Figure 5.5d. In this configuration, only Bragg-SPPs modes can be excited. The absence of intense resonances underlines the crucial role of the metal nanostructuring that cater for strongly localized modes as described elsewhere [166]. The light incoupling mechanisms of our PC can be understood in a simplified picture as the interaction of individual metallic (Figure 5.5b) and dielectric (Figure 5.5d) gratings. The interplay between localized and Bragg plasmons has been reported to greatly modify the mode distribution and to enhance the resulting oscillator strength [160,161]. Such hybridization is also evident from the spatial field profile shown in Figure 5.4b. Intense Bragg-SPP modes dominate above 800 nm, and the coupling of those with the localized modes appearing at the edges of the metallic cylinders give rise to strong enhancement. The origin of λ_2 and λ_3 resonances is therefore respectively attributed to the interaction of Bragg and localized plasmon modes (Figure 5.4c) and to propagative modes (Figure 5.4d).

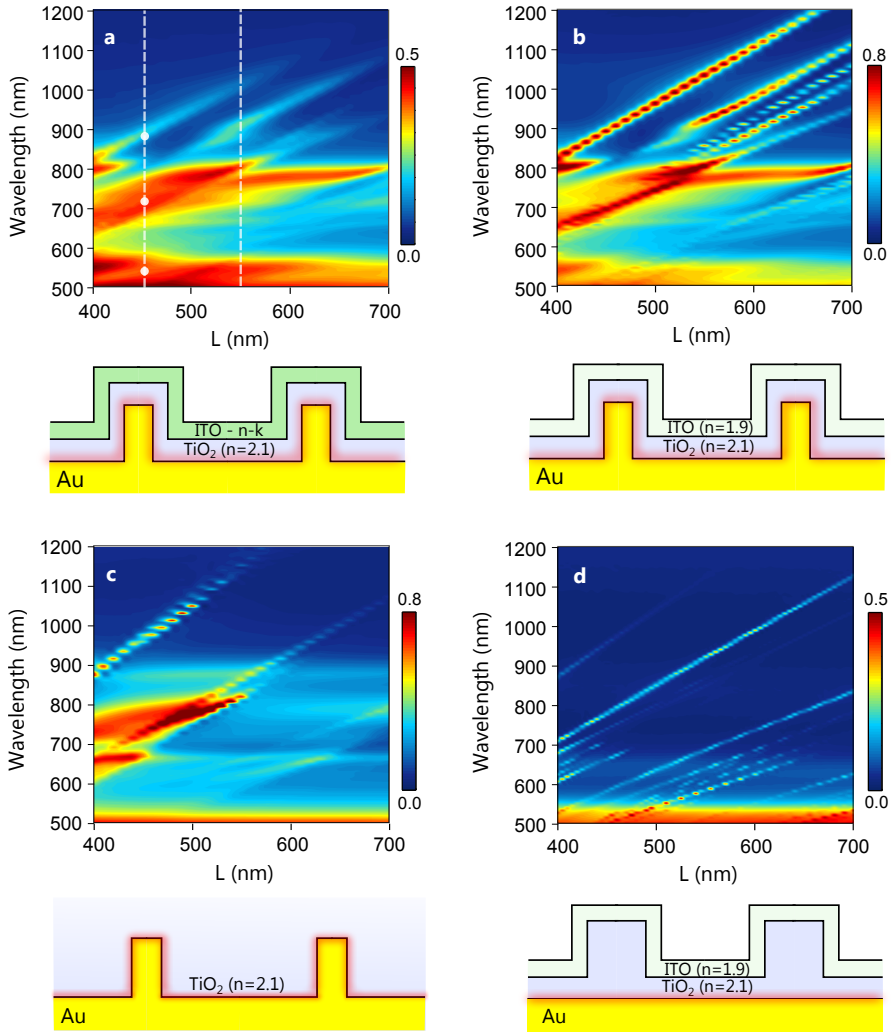

Figure 5.5: Analysis of the spectral response of the plasmonic crystal based photodetectors. Simulated absorption in Au with varying lattice parameter of a structure with $r = 150$nm (a) considering the complex refractive index of ITO, (b) a non absorbing ITO, (c) TiO_2 Au corrugated interface and (d) a dielectric (TiO_2 - ITO) array on top of a flat Au film. Vertical dashed lines indicate two of the lattice parameters employed to fabricate the devices from Figure 5.3. The white dots represent the points where the field profiles are shown in Figure 5.4. Modes at the metal can be excited either by coupling to SPPs with a dielectric grating (panel d), a metallic grating (panel c) and the resulting interaction of both (panel b).

5.3.2 Localized, propagative, and hybrid modes

To underpin the description of the plasmonic and photonic properties of the plasmonic crystal structure, we turn now our attention to the angle dependence of the absorption in the metal. Modifying the illumination angle results in the coupling to different diffraction orders, offering thus a richer description of the mode interaction. The simulated absorption as a function of the in-plane momentum component $k_{||} = k_0 \sin(\theta)$ is presented in Figure 5.6 for a configuration $L = 450$ nm, $r = 150$ nm and $t = 60$ nm of TiO_2. The $k_{||} = 0$ slice corresponds to normal illumination as shown in Figure 5.5b. The Bragg-nature of the mode at 900 nm is clearly illustrated. This correspond to a 4-fold degenerate mode, resulting from the in phase-interaction of different propagating modes. The band between 700 nm and 850 nm is especially interesting. The coupling and coherent interaction of grating-mediated and localized surface plasmons result in the appearance of intense spots and anti-crossing features. Higher energy propagative modes interact with different localized resonances, from 1000 nm to 700 nm, as $k_{||}$ varies from 0.2 to normal incidence. As it was previously suggested, the observed resonance at 714 nm is the result of the interplay of propagative modes with localized resonances in gold nanopillars. For shorter wavelengths the bulk, interband absorption of gold becomes the dominant absorption mechanism. Yet, hot-electron photocurrent is only monitored once it overlaps with the different grating orders, which further supports the observed differences in total absorption and responsivity below 550 nm (Figure 5.5a). This feature confirms earlier theoretical predictions, and evidences the lower efficiency of interband transitions for plasmonic hot-electron harvesting [163].

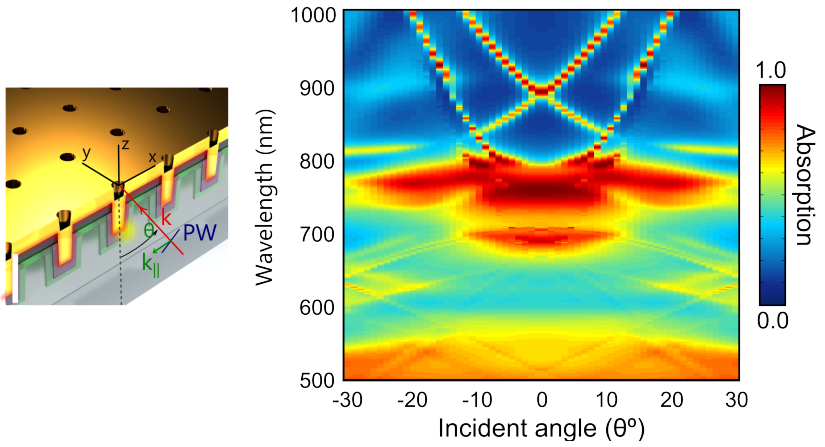

Figure 5.6: Dispersion relation of a plasmonic crystal sample with $L = 450$ nm and $r = 150$ nm. The in plane, $k_{||}$ component of the incident momentum, is changed by varying the angle θ. The absorption spectrum changes as different modes are excited.

A theoretical framework to account for the observed mode interaction, and that would allow for further *ab initio* design considerations can be adopted from previous works that describe the light scattering by particle arrays [157]. In such a formulation, the induced electrical dipole in the structure can be written as,

$$\mathbf{p} = \frac{1}{1/\alpha_E - G(\mathbf{k}_{||})}\mathbf{E}_{ext} \tag{5.1}$$

where α_E is a tensor describing the interaction of a particular element with the electric field, and G is a function of the lattice that is minimized when the structure is resonant with the excitation. In this way, the properties of the individual particles and their associated localized resonances (α_E), are separated from those of the lattice $G(\mathbf{k}_{||})$. Strong light-matter interaction occurs when either $1/\alpha_E$, $G(\mathbf{k}_{||})$, or the sum of both are in resonance. The additional degrees of freedom provided by the plasmonic crystal architecture offer thus a versatile platform to tailor individual resonances and mode hybridization for particular applications.

5.3.3 Influence of pillar and coating properties

Further structural parameters can be employed as a leverage to tune the spectral response of this architecture in the VIS-NIR range. Modifying design parameters, such as stamp pillar height and radius can substantially affect the resulting modes and their interaction (Figure 5.7). Other material parameters, such as the selected semiconductor and its thickness, can be used to further tune the PC response (Figure 5.8).

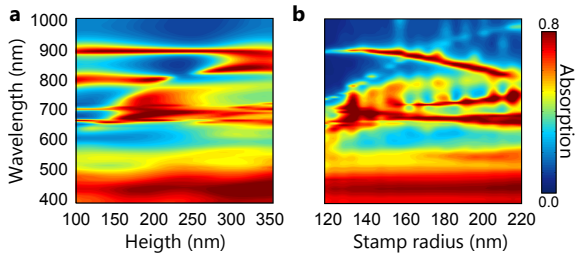

Figure 5.7: Influence of Au pillar heigth and radius on the plasmonic crystal optical properties. Variation of the simulated absorption in Au as a function of imprinted pillar height (a) and radius (b) for $L = 450$ nm and $t = 60$ nm.

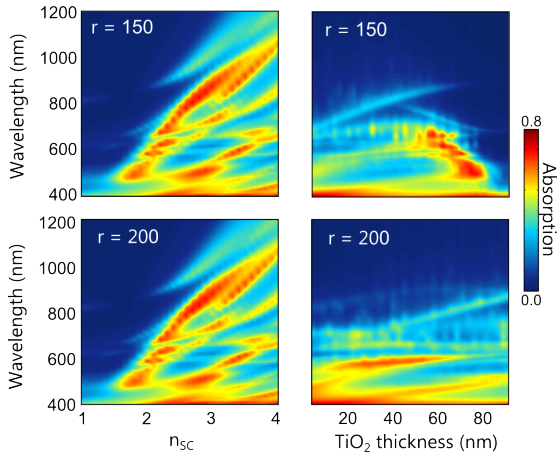

Figure 5.8: Influence of semiconductor refractive index and thickness on the optical properties of plasmonic crystal photodetectors. Simulated absorption in the Au as a function of semiconductor refractive index (top left) and and thickness (top right) for an imprinted cylinder radii $r = 150$nm (top) and $r = 200$nm (bottom). TiO_2 layer thickness limits the metal cylinder radius and modifies the position and intensity of propagating and localized resonances. The plasmon resonances are very sensitive to the coating's refractive index (right column), showcasing the importance of a proper semiconductor election for hot-electron device applications.

Pillar height: tweaking the pillar height, for example, affects the position of the 700 nm and 800 nm resonances since it is expected to modify the pillar localized resonance and the subsequent hybrid mode. The 900 nm resonance remains however invariant, as it is solely determined by the lattice parameter.

Pillar radius: the behavior with stamp radius (Figure 5.7b) is more complex, as not only does the local geometry change but also the gratings' filling fraction. As a consequence, the spectral response of the plasmonic crystal is modified. The variation of the stamp cylinder radius results in a slight blue-shift of the 900 nm resonance, and in a modification of the position and intensity of the hybrid resonances in the 600-800 nm window. These changes are attributed to the resulting different metallic pillars (as the ITO and TiO_2 thicknesses were kept constant) obtained by increasing the diameter of the initial cylinders.

Semiconductor optical properties and thickness: the variation of the optical response of the plasmonic crystal with the refractive index and thickness of the semiconducting oxide layer is shown in (Figure 5.8). The refractive index of the active semiconductor is found to play a crucial role for efficient light coupling across the VIS-NIR. This dependence is dictated by the optical properties of the underlying ITO layer

and the semiconductor thickness, which support propagative modes within the TiO_2 slab. The strong influence with this parameter offers also interesting opportunities for active plasmonic sensing applications, where small changes in the refractive index could be electrically monitored. An extra degree of freedom in the design is the thickness of the TiO_2 layer. Its modification influences both the available modes that can propagate, and the filling fraction and radius of the top metal layer. For the refractive index of compact, anatase TiO_2, ($n \simeq 2.1$), the optimum semiconductor thicknesses lie in the 60-80 nm interval.

5.4 Optoelectronic performance

In this section the optoelectronic characteristics of these structures operating as photodetectors are presented. The dark currentvoltage response, indicative of a Schottky junction between Au and TiO_2, is shown in Figure 5.9a. Despite the high-tunability offered by our plasmonic crystal architecture, responsivities at short-circuit conditions are still low for practical applications, a common drawback for plasmonic-hot electron devices. The application of a reverse bias to the Au/TiO_2 junction however allows leveraging the low injection yield, as the associated decrease in the barrier height favors an increasingly efficient hot-electron injection. The device responsivity as a function of reverse bias is shown in Figure 5.10 for different illumination wavelengths. We observe that absolute values are indeed increasing by orders of magnitude when the Schottky junction for increasing reverse bias. The sharp increase in photoconversion efficiency with applied voltage is ascribed to the strong Al_2O_3/TiO_2 barrier modulation, that promotes the injection of hot-electrons [101, 130]. As the reverse voltage increases, a higher fraction of the excited population can tunnel and the responsivity increases. This process saturates once most of the hot-electrons are injected. A similar behavior was also recently observed in MIM hot-electron devices [101]. Noticeably, both responsivity onset and saturation biases depend on the energy of the excitation $\hbar\omega$, as depicted for 406 nm, 640 nm and 900 nm illuminations. The hot electron population will be distributed along E_f and $E_f + \hbar\omega$ [162]. Consequently, higher energy excitations are expected to produce responsivity onsets and saturations at lower voltages, whereas less energetic excited populations would require higher operation voltages. This trend is experimentally confirmed in our case, where both the onset and saturation voltage clearly depend on the illumination wavelength. To further corroborate this picture, we compared the observed trends in responsivity with a qualitative theoretical model that takes into account hot-electron injection through the bias-modified Au-Al_2O_3-TiO_2 barrier (Figure 5.9b). Our model takes into consideration the tunnel probability as a function of bias for an energy dependent, hot-electron population, at the metal-alumina

interface. A good qualitative agreement is obtained with respect to the experimentally measured behavior. A full description of the model can be found in appendix C.

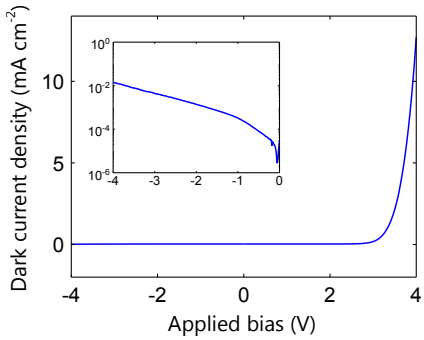

Figure 5.9: Dark current voltage characteristics of a Au-TiO_2 plasmonic crystal representative device depicting the Schottky junction established between the Au and the TiO_2 substrate. In the inset the dark current at reverse bias is shown in logarithmic scale for clarity.

Efficiency estimates: the situation of low performance at short-circuit conditions can therefore be overcome by operating the devices under reverse bias. In the saturation regime, responsivities as high as 70 mA/W are within reach for the hybrid modes, being ultimately limited by the absorption of the plasmonic structure, the hot-electron distribution and emission. This is, to our knowledge, the highest responsivity reported to date for plasmonic hot-carrier devices, and serves to showcase the potential application of electrically active plasmonic devices for photodetection. The corresponding external quantum efficiency in this case is 12%. The internal quantum efficiency can be estimated from the EQE by considering the absorption in the metal layer. This can be done with the aid of numerical simulations, since the absorbing character of ITO requires the separation of different contributions at each wavelength in the ITO. Total absorption measurements and the corresponding simulated profiles are shown in Figure 5.11. The absorption was calculated as $1-R-T$. Reflectance was measured using an Agilent 660 FTIR attached to a microscope with a 4X objective (NA 0.1) and a spatial mask. The experimental absorption was then reproduced with FDTD simulations. An accurate estimation of the IQE is highly challenging, since tiny deviations between measured and simulated values can affect the calculation. An interval is however given, whose limits are calculated from the most pessimistic (all experimental absorption takes place in gold) to the most optimistic (absorption in the gold taken from simulations) situations. This would yield an IQE estimation between 17% and 30%. In the same way the IQE can be calculated for other wavelengths. The IQE at 406 nm ranges from 6.04% to

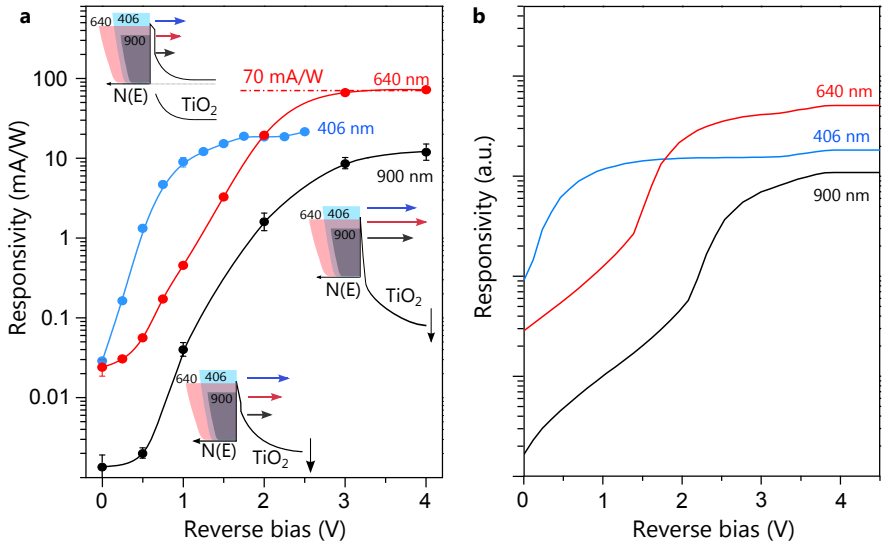

Figure 5.10: Device optoelectronic performance. (a) Responsivity as a function of applied reverse bias for a representative device (r=150nm, L=450nm) at three different illumination wavelengths. Negatively biasing the junction results in a prominent increase of responsivity as a higher fraction of the hot electron population is able to tunnel through the Al_2O_3/TiO_2 barrier. Depending on the illumination energy different responsivity onsets and saturation voltages are obtained, as the tunneling probability increases for lower energies with increasing bias. A maximum R = 70 mA/W is obtained for 640 nm illumination at 4V reverse bias. (b) Proposed model to describe hot-electron injection for different reverse biases (see appendix C). The responsivity saturates once the lowering of the potential barrier allows for the tunneling of the majority of excited states.

8.65%, and the one associated to 900 nm from 2.71% to 8.15%. EQE and IQE values are summarized in table 5.1. The sensitivity of the devices is characterized with the specific detectivity D^*, where the noise spectral density was estimated as $S_n = \sqrt{2qI_d}$ (shot-noise limit). Under the optimum operation conditions this yields a D^* of $3.3 \cdot 10^{10}$ Jones. The maximum hot electron excitation, injection efficiency and sensitivity is thus obtained when Bragg and localized modes interact.

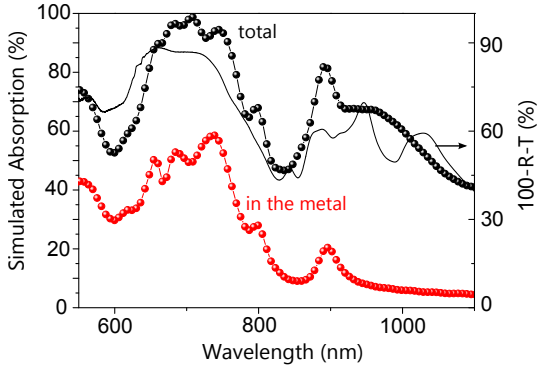

Figure 5.11: IQE estimation. Simulated absorption in the photodetector architecture (calculated as 100-R, black dotted line) versus simulated absorption in the gold layer (red dotted line). The value of 100-R measured in an actual device is presented in solid line for comparison (right axis). The estimated IQE lies between 17% and 30%, if the total experimental absorption (which comprises the absorption in the metal plus the residual one in the ITO) or only the simulated absorption in the metal is considered.

Table 5.1: Performance of PC sensors for different illumination wavelengths

λ(nm)	R (mA/W)	EQE (%)	IQE (%)	D^* (Jones)
406	19	5.8	6.0 - 8.6	$9.1 \cdot 10^9$
640	70	12.0	17.0 - 30.0	$3.3 \cdot 10^{10}$
900	11	1.6	2.7 - 8.1	$5.3 \cdot 10^9$

The temporal response of the devices is shown in Figure 5.12a, where the photocurrent is shown under pulsed illumination. The decay is in the tens of ms range ($\sim$ 100 ms), is currently limited by the RC constant of the devices, in view of their large area footprint (9 mm^2) and high TiO_2 resistivity. Further improvements can be readily achieved via appropriate geometric designs. We also characterized the dynamic response of the plasmonic crystal devices by monitoring the generated photocurrent at different power intensities (Figure 5.12b). There is a clear linear response with irradiance, which suggests that within the collected electrons there are no non-linear processes involved (at least to an experimentally appreciable extent), such as for example the collection

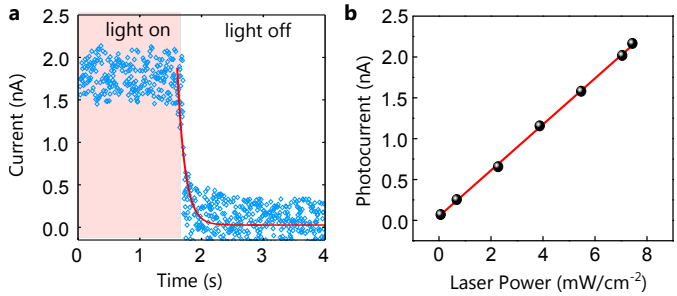

Figure 5.12: Temporal and dynamic response. (a) Time trace of a representative device at short-circuit conditions. The decay is fitted with a single 125 ms exponential, in excellent agreement with the extracted RC constant of the device (the measured $C = 5$ nF and $R = 25$ MΩ at the same conditions yield a $\tau = RC$ of 125 ms). (b) Obtained photocurrent at short circuit conditions as a function of incident laser power for 635 nm illumination.

of secondary excited electrons.

5.5 Conclusions

In this chapter we have presented a robust and novel architecture for multispectral, visible-infrared photodetection, based on hot-electron injection from plasmonic crystals. Our approach is not only interesting from a photonics point of view, due to the rich optical response of the plasmonic crystals, but also from a practical point of view. Unlike prior hot-electron devices, we make use of soft-NIL, a fabrication technique compatible with large area manufacturing processes. Moreover, our device architecture has reached responsivities up to 70 mA/W and IQEs up to 30% when operated at reverse bias. Combined with the large scale compatible fabrication, this enables the use of this technology for practical, out of the lab, applications. Improvements in responsivities can be expected by further controlling hot electron emission and collection directions, shown to increase the collection efficiency of hot electrons in other systems, and by geometry optimization. Other areas such as photovoltaics or photocatalysis [53,85] can benefit from this approach, as large area and infrared sensitization can respectively result in reduced fabrication costs and increased efficiencies. Further development will rely on the challenging task of finding specific plasmonic crystal designs capable of extending the photoconversion process into the SWIR and mid-infrared regions. The active exploitation of plasmonic non linear effects also offers an interesting route to be explored [13,167], as it could find applications in up-conversion detection for enhanced IR sensing.

6

Prospects for Hot-Electron Optoelectronics

In this chapter we theoretically explore a roadmap for next generation plasmonic hot-electron optoelectronic devices. We first analyze the projected performance of plasmonic solar cells and demonstrate how the use of a MIS architecture can circumvent current predicted limitations [119]. The presence of a thin insulating layer can serve not only to passivate surface defects and control V_{oc} and J_{sc} in the case of SAM devices, but also act as a leverage to the performance-limiting thermionic dark current. Based on that we demonstrate that MIS plasmonic solar cells can outperform best MS predictions for a given choice of materials over a factor of three. We then apply our model to estimate the performance of MS and MIS photodetectors. As it has been outlined in chapters 2 and 4, the presence of a Schottky barrier sets a cut-off energy for hot-electron harvesting. Lowering this barrier would promote more efficient electron injection, but also, on the other hand, result in elevated dark currents. We explore this trade-off in sensitivity and suggest the use of an insulating barrier as a means to extend detectivities into the infrared region. We will conclude by presenting an outlook on future directions for hot-electron optoelectronics, with emphasis on the use of novel plasmonic materials, such as degenerate semiconductors, and on structures maximizing hot-electron emission.

6.1 Photovoltaic applications

The outstanding light-matter interaction of plasmonic nanostructures makes them ideal candidates for light-energy harvesting. Fostered by the advances in plasmonic hot-electron photodetectors, few theoretical frameworks that explore the potential of those devices for solar harnessing have been reported [118, 119]. Unlike in traditional photovoltaics, which rely on semiconductor absorbers, the photosensitization in this new class of devices arises as a consequence of plasmonic absorption and hot-electron injection (chapters 2 and 3). White *et al.* predicted a maximum PCE up to 8% [118] for Schottky plasmonic cell, assuming perfect absorption in the metal but overlooking electron transport from the metal to the MS interface. Recently, Leenheer *et al.* presented a more restricted scenario where, by including hot-electron emission dynamics the predicted PCE ranged between 1% and 10% [119]. The elevated dark current attributed to the thermionic emission process was found in the latter to be a limiting factor for the V_{mpp}; high Schottky barriers ($\phi_b > 0.7$ eV) were required at the expense of the number of injected carriers. In what follows, we present theoretical performance predictions based on upgraded versions of the two aforementioned models, and also propose a third description matching experimentally realistic conditions for the metal-semiconductor interface. The optimum operating conditions and main limitations are then discussed. In order to estimate the PCE both photocurrent and dark-current bias dependence need to quantified as,

$$PCE(\%) = \frac{|J_{ph} + J_d|V}{P_{inc} \times 100} \tag{6.1}$$

The dark current can be split into its thermionic (J_{th}), majority carrier, and diffusion (J_{diff}), minority carrier components,

$$J_d = J_{th} + J_d \tag{6.2}$$

where,

$$J_{th} = A^* T^2 e^{-\phi_b/V_t}(e^{V_a/V_t} - 1) \tag{6.3}$$

$$J_{diff} = q\frac{D_e n_i^2}{N_d L_h}(e^{V_a/V_t} - 1) \tag{6.4}$$

A^* is the material-dependent modified Richardson constant, which ranges from ~ 30 to 120 A/cm^2/K^2. $V_t = kT/q$ is the thermal potential, D_h the diffusion coefficient, n_i and N_d respectively the intrinsic and majority carrier concentrations, and L_h the diffusion length. In a Schottky diode, the dark current is dominated by the thermionic emission component, which corresponds to the injection of majority carriers between the metal and the semiconductor. In practice, J_{th} greatly limits the maximum obtainable open-circuit potential due to the elevated dark current [168]. J_{diff} describes on the other hand the diffusion of the excess, minority-carriers from the depletion region to the electrodes. The photocurrent can be split into different processes, and obtained as,

$$J_{ph}(V_a) = q\int \varphi(\lambda)\eta_{abs}(\lambda)\eta_t(\lambda)\eta_i(\lambda, V_a)d\lambda \tag{6.5}$$

where $\varphi(\lambda)$ is the incident flux, $\eta_{abs}(\lambda)$ represents the process upon which an incident photon generates an electron-hole pair, and $\eta_t(\lambda)$ and $\eta_i(\lambda, V_a)$ describe respectively the process of hot-electron transport and injection to the neighboring semiconductor. The differences in the models which have been reported to date [118,119], arise from a different description of the latter processes. The introduction of momentum considerations defines a narrow electron-escape-cone (determined by the emission angles which allow sufficient momentum to transverse the interface, as described in chapter 2) in $\eta_t(\lambda)$, showing a drastic reduction in the maximum PCE, which is lowered from 8% to 1%. This condition is however often relaxed due to the existence of surface imperfections, poly-crystalline domains or small feature sizes. Moreover, the suitability of the

generalized Fowler theory, on which ref. [119] relies upon, has been recently questioned for nanostructured metals [64]. The conceptual differences of these models are depicted in Figure 6.1. The most optimistic, absolute upper bound for performance, (panel a) corresponds to a system where all photons are absorbed, converted into electrons and injected once at the interface in case they retain enough energy to surpass the barrier (or equivalently, that all the energy corresponds to the momentum perpendicular to the interface). This approach could nevertheless be valid to describe extremely thin metal films, nanoparticles or nanostructures with features on the order of 20 nm or fully embedded in a semiconductor, where hot-electron injection processes are predicted to be more efficient [64, 119, 169, 170]. The electron transport is assumed to be perfect in this model, and material properties such as the electron mean-free-path or the field distribution inside the metal were not taken into account. As a compromise between this and the model of Leenheer *et al.*, we consider a scenario where an emission cone is defined as a function of L_{MFP} and the decay length of the field intensity inside the metal. Hot-electrons that reach the interface without collision events and enough energy, are assumed to tunnel regardless of the momentum component perpendicular to the interface. This could be driven by surface features or defects which, by breaking the traslational invariance, result in wider emission cones. Our proposed model would collapse to the one proposed by White *et al.* for nanostructures small enough with respect to the mean-free-path.

The material-dependent emission cone is defined as,

$$\theta_{max}(z, \lambda) = \arccos\left(z / L_{MFP}(\lambda)\right) \tag{6.6}$$

provided $z < L_{MFP}$ (otherwise θ_{max} is assumed to be zero), where z is the distance to the interface. The collection of hot-electrons can be enhanced for properly nanostructured interfaces where more directions would have been accessible. An analytical expression for L_{MFP} was adopted from [119]. The overall transport efficiency can be computed by including the field intensity profile and integrating along z.

$$\eta_t(\lambda) = \frac{\alpha(\lambda)}{\pi} \int_0^\infty \theta_{max}(z, \lambda) \exp\left(-\alpha(\lambda) z\right) dz \tag{6.7}$$

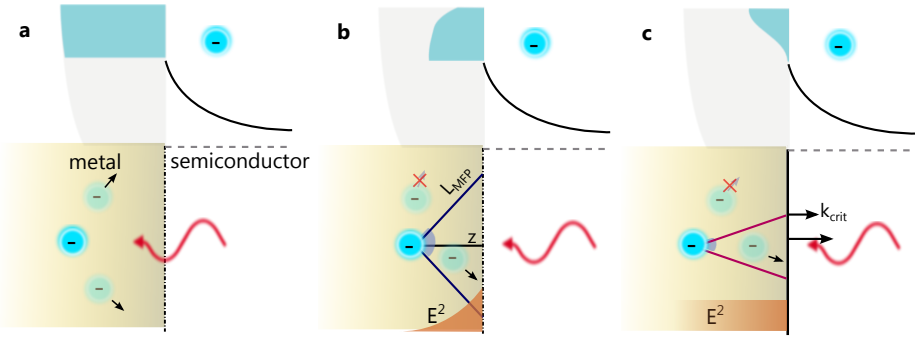

Figure 6.1: Models for hot-electron transport to the metal-semiconductor interface. (a) The simplest scenario corresponds to a system where all electrons with energies above the Schottky barrier height are injected, regardless of their initial position or direction. This could be the situation of ultrathin metallic nanostructures with features smaller than L_{MFP}. (b) If the electron mean-free-path is considered, only a fraction of the energetic electrons will be able to reach the interface before a collision event. This defines an effective emission cone narrower for higher energies. The majority of the carriers will be however generated in the vicinity of the interface, following an $\exp(-\alpha z)$ dependence. (c) A more restricted approach consists of introducing a cut-off emission angle, corresponding to the minimum momentum (k_{crit}) required to surpass the barrier. This would be the case of a perfectly flat and single-crystalline metal.

The situation depicted in Figure 6.1c corresponds to the most restrictive scenario. The electron emission cone is defined in this case as,

$$\theta_{max}(\lambda) = \arccos\left(\frac{k_{crit}}{k}\right) = \arccos\left(\sqrt{\frac{E_F + \phi_b}{E_F + \hbar\omega}}\right) \tag{6.8}$$

where k_{crit} is the minimum momentum component required to overpass the barrier. The total transport efficiency can then be written as,

$$\eta_t(\lambda) = \int_0^{\theta_{max}} \sin(\theta) d\theta \int_0^{\infty} dz \exp\left(-\frac{z}{L_{MFP}(\lambda)\cos(\theta)}\right) \sin(\theta)\beta_E(z) \tag{6.9}$$

where $\beta_E(z)$ represents the field intensity distribution along the z direction, which Leenheer *et al.* considered to be uniform for thin enough films [119]. In all cases

we consider a uniform distribution of the hot-electron population between E_F and $E_F + \hbar\omega$, and an injection efficiency, $\eta_i(\lambda, V_a)$ described by the modelled barrier and the tunnelling probability described in appendix B. Unlike prior reports our model also includes the modification of the semiconductor band-bending with applied bias, which effectively reduces the amount of hot-electrons that can tunnel as the forward bias increases. As a result of this, fill-factors will be lowered with respect to bias-independent descriptions.

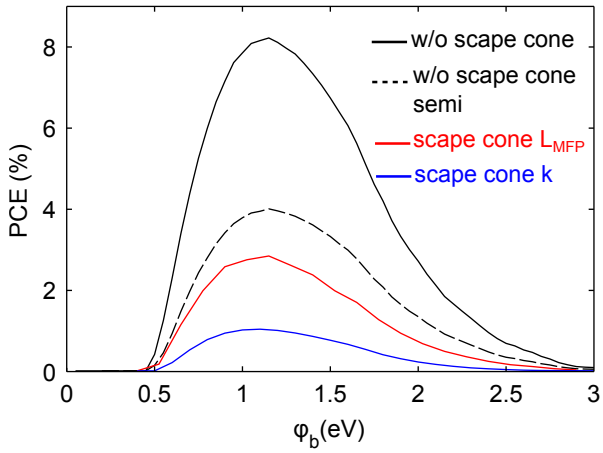

Figure 6.2: PCE as a function of ϕ_b for different models: without emission cone restriction [118], assuming an isotropic emission and a single planar interface only half of the emitted electrons reach the semiconductor. Under the restriction imposed by L_{MFP} and decay length, and under the restriction dictated by parallel momentum conservation [119].

The power-conversion-efficiency of TiO_2-metal plasmonic Schottky solar cells, as calculated by these models is presented in Figure 6.2 as a function of the barrier height. In all cases a threshold barrier, around 500 meV, is required in order to sustain an open-circuit voltage. This is a consequence of the elevated dark current posed by thermionic emission. The maximum PCE is maximum for ϕ_b within the 1-1.4 eV interval, and ranges from 1% (in agreement with ref. [119]) to 8%. If material restrictions are included, the maximum PCE drops to 2.7% for a single quasi-planar interface. The wide range of obtainable PCEs showcases the paramount importance of a proper nanostructure design for an efficient operation of plasmonic hot-electron solar cells. In the remainder of this chapter we will focus on exploring the upper limits for PCE, and for that follow the most optimistic scenario. The relevant photovoltaic figures of merit are shown in Figure 6.3, together with the current-voltage trace of the champion device. In Figure 6.2 it can be seen how the photocurrent moderately decreases with forward bias, dominating the total current J until thermionic emission takes over. Figure 6.3b shows

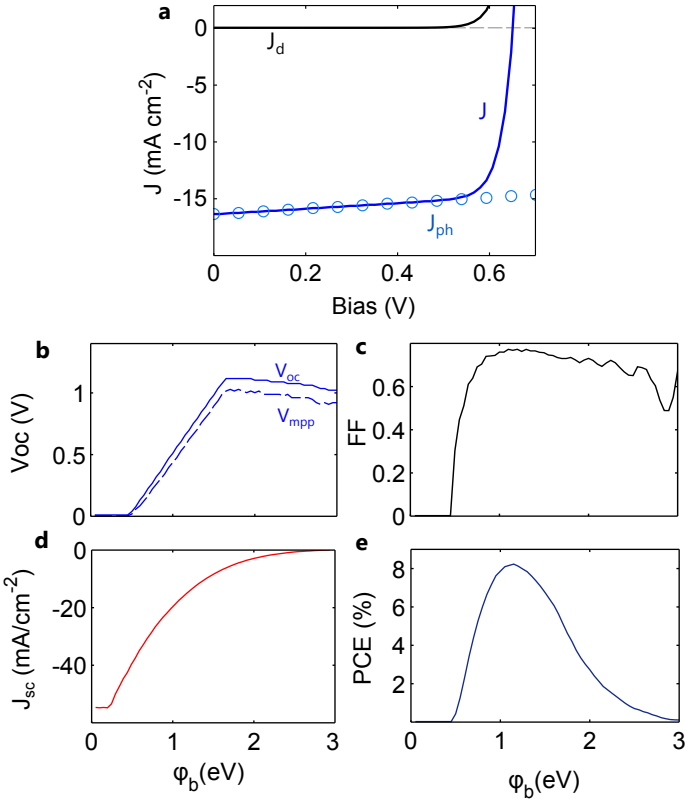

Figure 6.3: Predicted J-V characteristics and figures of merit. (a) Current-voltage trace for the best performing configuration ($\phi_b = 1.15$ eV). The dark-current onset determines the maximum V_{oc}. (b) V_{oc} and V_{mpp}, (c) FF, (d) J and (e) PCE, as a function of ϕ.

the dependence of V_{oc} and V_{mpp} with ϕ_b. A minimum barrier of 0.5 V is needed in order to allow for an open-circuit-voltage, and a difference of around 600 meV between ϕ_b and V_{mpp}. This hinders the photovoltaic response for low barriers. The fill-factor (panel c) rapidly rises until its maximum, and softly decreases after 1 eV. J_{sc} (panel e) continuously decreases with increasing barrier-height, establishing a trade-off for optimum PCE (panel d). It is clear that, besides electron emission considerations, the elevated thermionic dark current is constraining higher PCE yields. In what follows we discuss the benefits of the MIS architecture to leverage these limitations.

6.1.1 MIS performance estimates

In MS Schottky diode, the maximum barrier height for neat interfaces is given by $\phi_b = \chi_{sc} - E_{f,m}$. Therefore for a given choice of materials, the resulting barrier might not suffice to sustain a high V_{oc}, limiting the performance of the plasmonic solar cell. This limitation is a consequence of the elevated thermionic dark current. This situation can change, however, for a MIS configuration. The presence of the insulating barrier, can effectively reduce the tunnelling rate of majority carriers and also reshape the potential distribution across the cell. The thermionic component of the current follows the law,

$$J_{th} = P_h A^* T^2 e^{-\phi_b'/V_t}(e^{qV_{sc}/V_t} - 1) \tag{6.10}$$

In a MIS structure, with an insulator of appropriate electron affinity and thickness, the thermionic component can be much smaller than its MS counterpart [168]. This is mainly because of: (i) the tunneling probability P_h, typically expressed as $e^{-\chi_{ins}^{1/2} d}$ [171], (ii) the modified barrier height ϕ_b' and (iii), the smaller potential drop V_{sc} in the semiconductor, for a given a applied bias V_a. Its value depends on the voltage divider established by the insulator and the semiconductor (see appendix C). The situation for minority carriers will remain the same, as described in equation 6.4. As it was shown in chapter 3, the introduction of the barrier will also notoriously affect the amount of injected current. A trade-off therefore exists between reduced dark current (with the associated increase in V_{oc} and an efficient injection). In Figure 6.4 we present, for a fixed, neat Ag-Insulator-TiO_2 junction, the relevant figures of merit for different insulator thicknesses and electron affinities. Upon the introduction of very thin insulating barriers the short-circuit current drops for shallower electron affinities and thicker layers (panel

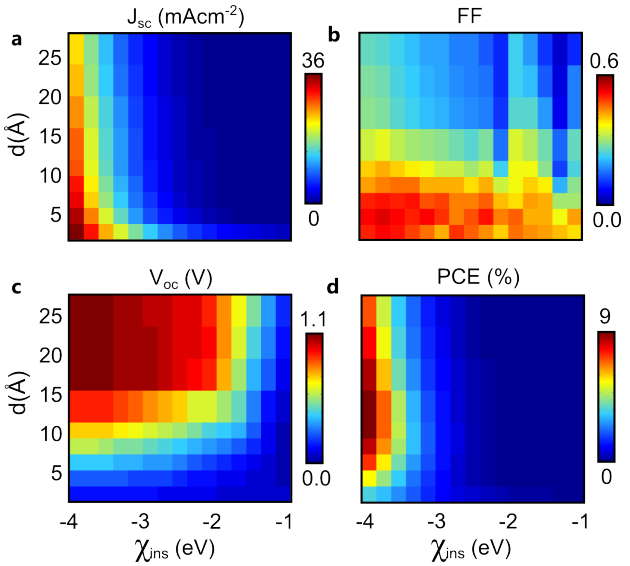

Figure 6.4: J_{sc}, V_{oc}, **FF and PCE as a function of** d **and** χ_{ins} **for a TiO$_2$-I-Ag junction.** (a) Short-circuit current, (b) fill-factor, (c) open-circuit voltage and (d) PCE. An increase from 2.3% (MS configuration) to 9% can be obtained by an appropriate choice of the insulating material thickness and electron affinity.

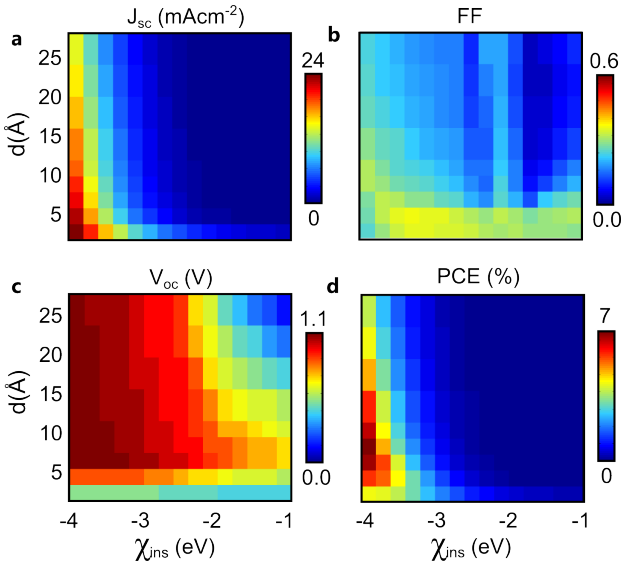

Figure 6.5: J_{sc}, V_{oc}, **FF and PCE as a function of** d **and** χ_{ins} **for a TiO$_2$-I-Au junction.** (a) Short-circuit current, (b) fill-factor, (c) open-circuit voltage and (d) PCE. A moderate decrease 7.138% (MS configuration) to 6.95% is obtained in this case. The performance in this scenario is limited by the drastic reduction in FF.

a). On the other hand, the obtained V_{oc} can be dramatically increased, from 0.13 V (in the absence of the barrier, where $\phi_b = 0.6$ eV), to up to 1.1 V. This is a consequence of the reduction in the thermionic emission component of the dark current. For insulators thick enough (above 1.5 nm), the dark current is instead limited by diffusion allowing for a much higher open-circuit voltage. Shallower electron affinities also reduce the dark current but the diminishing of the photocurrent is more prominent. As a consequence of this trade-off between V_{oc} and J_{sc}, a hot-spot exists where optimum efficiency is reached, corresponding to a PCE of 9%, over a three-fold increase compared to the MS counterpart. The challenge is to identify insulating materials with the adequate characteristics. Given the range of thicknesses and electron χ_{ins} [172], organic molecules appear to promising route to boost solar cell's performance.

In Figure 6.5 we present the same study, for a fixed, neat Au-Insulator-TiO_2 junction. In this case however, the presence of the insulating layer does not increase the net PCE but result in a moderate decrease (from 7.14% to 6.95%). This can be explained by the high V_{oc} in the starting MS configuration, where the barrier height was $\phi = 0.9$ eV, greater than in the silver case. Thus, the insulating layer does not substantially improve this figure of merit but reduces J_{sc} and FF. This suggests that the use of the MIS architecture is in particular adept for low barrier MS Schottky diodes. We note that this would be the case for neat interfaces, absent of electronic defects. As we have seen in chapters 3 and 4, surface imperfections and trap states often dominate the electrical response and the use of insulator interface layers in general improves the device performance over the MS counterparts.

6.2 Photodetection

Along this chapter we have discussed the importance of the Schottky barrier height for hot-electron plasmonic light-energy harvesting. We have shown that a trade-off exists between the dark current and the injection efficiency. In this section we discuss the effect of this trade-off on the performance of hot-electron photodetectors. The compromise between dark-current, associated noise, and responsivity, results in an optimum range of operation (or maximized D^*) in the $\phi_b - \lambda$ space. In order to evaluate the specific detectivity, the noise spectral density has to be calculated. In the remainder of the chapter we assume a shot-noise limited detectivity, where S_n is given by,

$$S_n = \sqrt{2qI_d} \tag{6.11}$$

q being the elementary charge and I_d the dark current. This election guarantees a conservative estimation for the sensitivity, since other sources, such as background-limit or Johnson noise are less intense [173, 174]. The dark current can be modelled as described in eq. 6.2. The calculated EQE, R, J_d, and D^* are shown in Figure 6.6, as a function of ϕ_b for different reverse bias. The EQE dependence with energy (or λ) and ϕ_b reflects the cut-off imposed by the Schottky barrier. As demonstrated in the previous chapter, the application of a reverse bias can increase the injection efficiency (panels a and b), and extends the response into longer wavelengths. The dark current is depicted in panel c, being limited by recombination and diffusion. As the barrier height is increased the thermionic component rapidly decreases. The resulting D^* is shown in panel d. For a given wavelength of interest, an optimum ϕ_b exists. D^* up to 10^{14} Jones can be achieved in the VIS-NIR regime for barrier heights on the order of $0.8 - 1$ eV. Under reverse bias conditions the sensitivity can be extended well into the MWIR and LWIR regions.

6.2.1 MIS to tailor photodetector performance

As discussed in the previous section, the introduction of an insulating layer can serve as a tuning mechanism to tailor the junction properties. If a barrier height is imposed by material constraints, a MIS architecture can be used instead to decrease the limiting effects of the dark current and extend the device sensitivity into the wavelength regions of interest. EQE and D^* are shown in Figure 6.7 for different insulator thicknesses, as a function of electron affinity, for a fixed ϕ_b of 0.3 eV. This would correspond to an average D^* of 10^{11} Jones as calculated in Figure 6.6. The EQE can be marginally increased towards lower energies upon the introduction of the insulating layer. This phenomena, *a priori* counter intuitive, can be attributed to a higher potential drop across the insulator, in exchange of a reduced band-bending in the semiconductor; as a result, a higher fraction of excited hot-electrons can be collected. Calculated detectivities are shown in the bottom row. The dark-current reduction allows for an extended sensitivity into the IR, especially for thin insulators, where up to 300-fold D^* enhancements can be expected. Insulating layers can thus also act as a leverage to increase the detectivity of MIS devices from otherwise low sensitivity MS photodetectors.

6.3 Novel materials

We have seen, throughout this thesis, that the most important limitations for hot-electron optoelectronic solar cells and photodetectors are: (i) a large-scale compatible fabrication method capable of exploiting plasmonic tunability and (ii) modest device

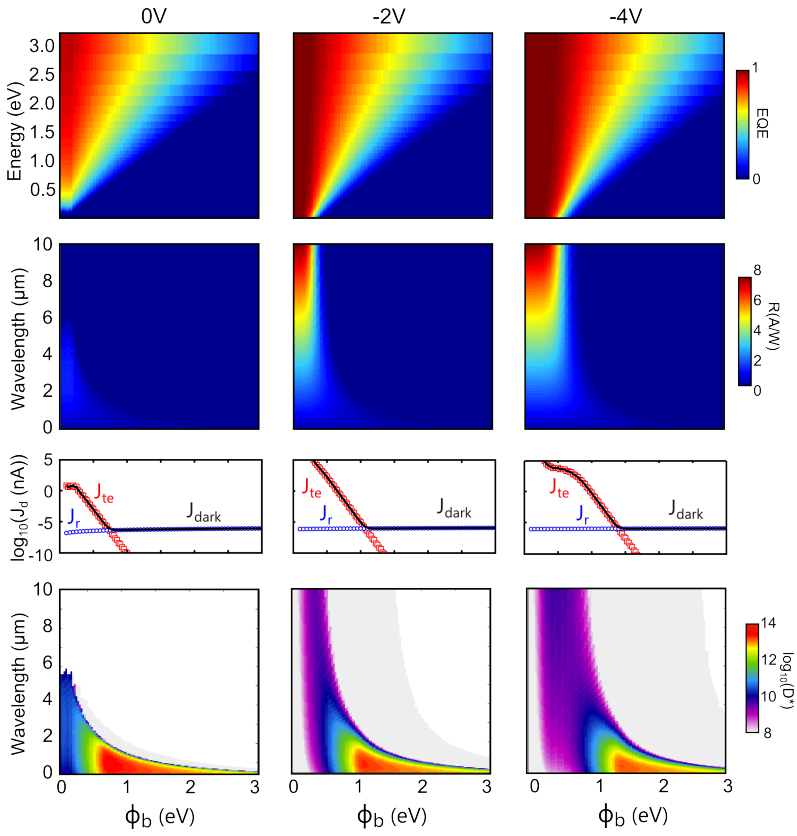

Figure 6.6: EQE, R and D^* as a function of Schottky barrier heigth ϕ_b and wavelength. From left to right, $V_a = 0V$, $V_a = -2V$ and $V_a = -4V$. The shot-noise limited specific detectivity is determined by the trade-off between R, which linearly increases with lower barriers, and dark current, that exponentially increases with barrier lowering.

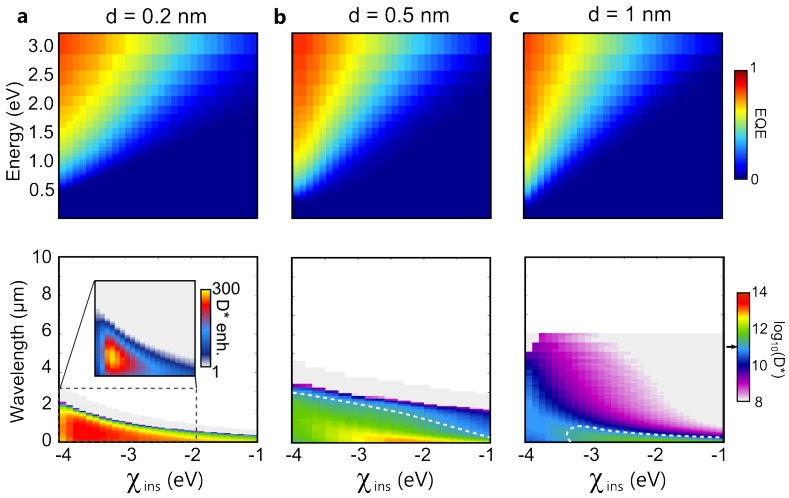

Figure 6.7: Insulating barrier to leverage photodetector performance. EQE and D^* (shot-noise-limited) for a given $E_f - \chi_{sc}$ difference of 0.3 eV (which would correspond to $\phi_b = 0.3$ eV in a MS configuration) and different insulator thicknesses and electron affinity. The presence of the insulator allows for increased D^* for a given metal and semiconductor, due to the associated dark current reduction. From left to right, $d = 0.2$ nm, $d = 0.5$ nm, and $d = 1$ nm. White dashed lines join the points with $D^* = 10^{11}$ Jones, corresponding to the MS reference.

performance due to the low injection yield. Both aspects were successfully tackled in chapter 5, where we presented a device platform capable of overcoming both aspects. In this section we will briefly discuss other alternatives which also have the potential of meeting those requirements. For an efficient photon-to-electron conversion, harvesting structures must favor Landau damping over radiative recombination and, as considered in section 6.1, be small enough to reduce escape-cone and material limitations—conveniently, Landau damping is more efficient for small particle sizes [58, 70, 163, 175, 176]. Metallic nanoparticles (NPs) are ideal candidates to match this conditions; they have been widely studied, their size can be tuned in a facile way and more important, are solution processable (up to a given, long diameter). The absorption spectrum of silver and gold nanoparticles is shown in Figure 6.8, with narrow resonances in the visible. A set of nanoparticles whose spectral response can be tuned across the VIS-NIR, are nanorods (NR) and nanotriangles (NTs). The absorption of Au NR and Ag NTs is also represented in the Figure for a particular aspect ratio. Another exotic way to harvest IR photons is to use degenerate semiconductors, such as copper-sulfide (Cu_2S) or ITO NPs. The plasmon resonance position, proportional to $\sqrt{N_d}$, can be precisely tuned by adjusting the carrier concentration. Given the combination of wide-tunability, appropriate size and solution processability, these materials are exciting candidates access spectral regimes that cannot be reached by traditional semi-

conductors or are based on toxic cadmium-mercury-telluride materials [177,178].

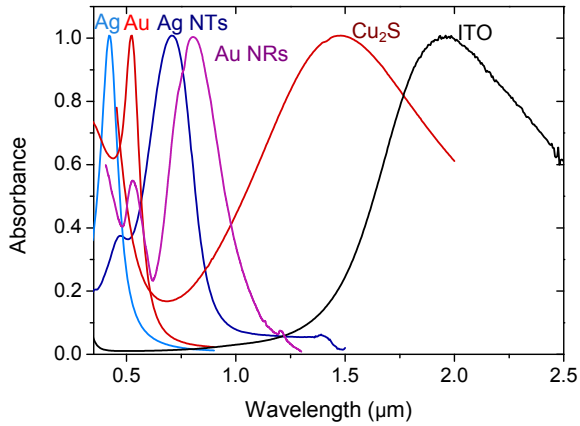

Figure 6.8: Solution-processable materials for VIS-NIR hot-electron harvesting. By either changing the metal (Ag vs. Au nanoparticles), the shape (Ag nanotriangles Ag NT and Au nanorods Au NR), or the doping in degenerate semiconductors, such as copper-sulfide (Cu_2S) or ITO nanoparticles, the plasmon resonance can be tuned from the visible to the short-wavelength infrared.)

6.4 Conclusions

In this chapter we have discussed the limitations of plasmonic-hot electron technology for solar energy harvesting and photodetection. We have showcased the importance of proper device design and nanostructuring for efficient hot-electron collection, with maximum PCE up to 8%. Despite being lower than the Schokley-Queisser limit for standard solar cells (33%), these kind of devices might find its niche for unconventional light-harvesting applications, where the exotic properties endowed by the plasmonic nature of photoelectric conversion would be advantageous. Given the stability of this platform, which solely relies on noble metals and oxide semiconductors [179], the presented devices are also great candidates for photocatalytic applications, such as H_2 or fuel production [85], and active photochemistry [180]. We have also theoretically evaluated the additional degrees of freedom in device design presented by MIS, that allowed us to overcome ϕ_b restrictions and, increasing the PCE by over a three-fold factor for a given choice of materials. The presence of the interface mainly served to reduce the dark current and redistribute the electrostatic potential distribution across the device. The performance of plasmonic hot-electron photodetectors was also examined. Despite the R-ϕ_b trade-off, the sensitivity of these devices can be extended well into the infrared, with maximum detectivities up to 10^{14} Jones.

Conclusion

The field of plasmonic hot-carrier optoelectronics has seen tremendous advances during the last years. The enticing light-matter interaction of plasmonic systems enables for a new class of devices where, unlike in semiconductors, optoelectronic functionalities are determined from metal nanostructuring. The combination of wide and facile tunability with high absorption is especially appealing for photovoltaic and sensing applications. The results presented in this thesis aim at representing an advance in the knowledge and performance of this technology.

Significant challenges existed nevertheless prior to this work, which posed severe restrictions to the potential of this optoelectronic platform, both from performance and implementability perspectives. In this thesis we have addressed the aforementioned issues leading to the next findings:

- **Demonstration of the first hot-electron plasmonic Schottky solar cell.**

  The most straightforward approach to harvest plasmonic hot-electrons is the Schottky metal-semiconductor junction. Prior to this work, proof-of-concept plasmonic Schottky diodes had been reported [107]. These devices however lacked of the ability of a photovoltaic response. In this thesis we identified the crucial role of the metal-semiconductor interface for photovoltaic applications. In chapter 3 we pinpointed surface interfacial states as the origin of open-circuit voltage suppression. While hot-electron injection was possible (with efficiencies above 4%), these states resulted in Fermi level pining thus hindering the photovoltaic response of this architecture. We found that, by introducing an ultrathin insulating alumina layer, interface states could be passivated, which enabled for the concurrent achievement of short-circuit current and open-circuit voltage, a requisite for energy conversion. In doing so, we also found that hot-electron injection

processes were affected: energetic electrons had to traverse this interfacial layer, lowering the injection yield and the optoelectronic performance. By optimizing the device architecture, power conversion efficiencies of 0.03% were reported. Different types of electron injection mechanisms were also identified depending on the choice of materials: for Ag-based MIS devices the majority of hot-carriers undergo Schottky-like emission or trap-assisted tunnelling, whereas in Au-based MIS devices the dominant transport mechanisms Fowler-Nordheim tunnelling.

- **Tailoring the photovoltaic response by interface molecular control.**

  The utilization of an inorganic insulating layer allowed for a photovoltaic response at the cost of limited injection. In chapter 4 we explored the use of self-assembled monolayers (SAMs) to concurrently control open-circuit voltage and short-circuit current. On top of the ability to passivate surfaces, the plurality of parameters, such as structure or chemical composition that could be tuned, allowed for the tailoring of the interface properties. We have shown that, by adjusting SAM molecule's length, the injection efficiency could be increased, resulting in higher external quantum efficiencies (up to 5%) and power conversion efficiencies (up to 0.1%). We have also showcased the ability of SAMs to control the open-circuit voltage in these devices, depending on the dipole moment of their constituent molecules'. This enabled for the achievement of open-circuit voltages from 0.2 V to above 0.5 V. Interestingly, we found that the depending on the electronegativity of the moiety exposed to the metal electrode, injection yields could be modified. Record power conversion efficiencies of 0.11% were achieved by SAM optimization.

- **A large-scale, spectrally-tuneable and efficient, sensing platform.**

  Prior to this thesis, one of the major roadblocks to make hot-electron optoelectronic devices deployable, was the lack of a platform that, while being compatible with large-scale manufacturing processes, would give access to the high degree of spectral tunabillity endowed by plasmonic nanostructures. In chapter 5 we introduced a quasi-3D plasmonic crystal photodetector, where the spectral response can be finely tuned across the visible-near infrared spectrum by modifying the crystal's structural parameters. Unlike other tunable hot-electron devices reported to-date, whose fabrication relied on costly and low-throughput fabrication processes, we employ soft-nanoimprinting lithography: a technique already compatible with industrial standardized roll-to-roll manufacturing. We found that the spectral response in these plasmonic crystal detectors, is determined by the interplay between localized and surface plasmon modes. Design routes to tailor it has been also presented. The use of this architecture is not only advantageous

fabrication-wise, but also resulted in a significant leap in performance: under the proper operating conditions, PC devices showed record responsivities for this technology up to 70 mA/W.

To conclude, we expect the work presented here to mean a significant step forward towards a new generation of devices that, with enhanced functionalities beyond classical semiconductors, will be useful for optoelectronic applications.

Appendices

A

Materials and methods

Inorganically passivated hot-electron devices

Flat references: flat reference samples were built in order to minimize surface roughness that would give rise to plasmonic coupling. ITO-coated glass substrates were purchased from Stuttgart University and cleaned before use with acetone, ethanol, and DI water, each in sequence sonicating for 10 min. Flat devices were fabricated by the ALD of 50 nm of TiO_2 over the as-prepared ITO substrates.TiO_2 coatings were fabricated from water and titanium isopropoxide; valves were set to 0.015 and 0.065s, respectively, followed by 10 s pump time (0.025Åper cycle). The deposition chamber temperature was held at 200 °.

Textured samples: FTO-coated glass substrates were purchased from Xop Fisica and cleaned manually with DI-water and soap, and subsequently in acetone, ethanol and DI water baths under sonication. TiO_2 films were deposited on top of FTO substrates: briefly, a solution of a commercial TiO_2 paste (90T-Dyesol) was prepared in ethanol by diluting it at a 1:2.5 w/w concentration. The mixture was sonicated for 1h before use

to improve phase uniformity. Films were spin casted at 3000 rpm. by fully covering the substrate prior to rotation. Samples were gradually heated from 120°to 200°(30 min) and left at 500°for 1 hour. Once the substrates cooled down they were inmersed in a span of 20mM solution of $TiCl_4$-DI water at 75°for 30 min for densification. Samples were cleaned with DI water and heated up to 500°for 1h. Substrates were stored in ambient conditions before use.

Alumina deposition: Al_2O_3 was deposited by atomic layer deposition (Savannah 200, Cambridge Nanotech). Water and trimethylaluminium were used as precursors of Al_2O_3 with open valve times of 0.05 and 0.10 s, respectively, followed by 65 s pump time (1.1Åper cycle). The chamber was kept at 150°during the deposition process. All TiO_2 substrates were heated at 120°for 30 min to remove moisture traces prior to ALD.

Electrode deposition: 300 nm of metal were deposited on a Kurt J. Lesker Nano 36 system at a rate of 0.5Å/s for the first 30 nm, and 1.5Å/s for the remaining 250 nm, at a base pressure lower than $2 \cdot 10^6$ mbar. Metal thickness was controlled together with the deposition rate with a quartz crystal. A 200 nm thick ITO film was deposited by DC magnetron sputtering (AJA International Orion 8) at room temperature. The sputtering was carried out at 60W DC-power and at a working pressure of 2 mTorr in a 5% oxygen-argon atmosphere. A shadow mask with 2 mm diameter circles was used to define the are of the contact pads.

Hot-electron devices with SAM interfaces

TiO_2 substrates: textured and flat substrates were fabricated in a fashion already described for alumina passivated devices in the previous section.

SAM functionalization: TiO_2 substrates were incubated for 24h in solutions of the different molecules in toluene. All substrates were annealed at 200°for 30 minutes prior to incubation to remove traces of moisture. The concentration was kept constant for all molecules at 0.2M when possible, otherwise limited by the saturation solubility of each compound. Incubation baths were stirred periodically before sample cleaning. TiO_2 functionalized substrates were cleaned by vigorously rinsing them in toluene to remove ungrafted molecules. Reincubation and cleaning processes were repeated for 3 times to ensure monolayer coverage.

SAM characterization: after incubation, the presence of the SAMs was assessed by FTIR spectroscopy (Agilent FTIR spectrometer 660 attached to an optical microscope and through a 15X Cassegrain objective). Prior to that, samples were kept in a vacuum chamber for 30' at a $1 \cdot 10^{-6}$ mbar base pressure to reproduce pre-electrode deposition conditions. After electrode deposition the vibrational signatures of the SAM were acquired with a Renishaw inVia Raman microscope. Samples were illuminated with a 532-nm laser excitation from the FTO side and confocally focused on the TiO_2-metal interface; the measured Raman spectrum had a range from 100 to 5000 cm^1, with a resolution of 0.6 cm^1. The integrity of the SAM after metal deposition was also corroborated with ATR-FTIR measurements over a thin, 3 nm Ag layer

Electrode deposition: 200-300 nm of silver were deposited on a Kurt J. Lesker Nano 36 system. The evaporation conditions were critical so as to avoid junction damage, which would lead to short-circuited or unpassivated devices. The chamber base pressure was kept lower than $1 \cdot 10^{-6}$ mbar for all evaporations. A low evaporation rate was required for at least the first 40 nm (always bellow 0.3 Å/s) after which it could be increased up to 1Å/s for the remaining thickness. The chamber temperature was monitored and kept always bellow 50°as otherwise device performance started to deteriorate. The final thickness and deposition rates were controlled with a quartz crystal sensor. A shadow mask with 2 mm diameter circles was used to define the contact pads area.

Molecule modelling and dipole moment calculations: all molecules coordinates were retrieved from the HIC-Up online database (Uppsala University, `http://xray.bmc.uu.se/hicup/`). Their geometries were subsequently optimized with a Broyden-Fletcher-Goldfarb-Shanno algorithm and dipole moments calculated theoretically using AM1 parametrization with the semi-empirical quantum chemistry program Arguslab (`http://www.arguslab.com/`).

Hot-Carrier Plasmonic Crystal Photodetectors

NIL procedure: nanostructured electrodes were fabricated by nano-imprinting lithography. A polydimethylsiloxane mold (PDMS, 10:1 Sylgard 184), replicating a square array pattern from a silicon wafer (AMO gratings), was used as "printing stamp". A UV photocurable epoxy (SU8, Microchem), was spin-cast on top of ITO-coated substrates (Stuttgart University) to make 500 nm thick films. Samples were ethanol-wetted and imprinted with the PDMS stamp. Patterned resists were UV cured after imprinting to

improve its mechanical stability ($\lambda = 360$ nm, 15 min), through a spatial mask defining squared imprinted regions of 9 mm^2. Once the resists are exposed and developed, 40 nm of ITO are sputtered onto the substrates using an AJA sputtering system without masking, so the sputtered ITO is electrically connected to the commercial ITO coated substrate. Finally, a 90 min annealing step at 200°Cis carried out under inert atmosphere to improve the conductivity of ITO. 60-80 nm of TiO_2 and 0.5 nm of Al_2O_3 were deposited by atomic layer deposition as previously described. 200 nm of gold were deposited on a Kurt J. Lesker Nano 36 Systemat a rate of 0.5 $Å s^{-1}$ for the first 30 nm and 1.5 $Å s^{-1}$ for the remaining 250 nm. The base pressure was lower than $2 \cdot 10^6$ mbar. The whole fabrication process is sketched for clarity in Figure 5.1.

FDTD simulations

Material modelling: the optical properties of the different materials used in the simulations were described as follows:

- Glass substrate: dielectric medium with constant $n = 1.425$
- SU8 resist was modelled by a dielectric medium with constant $n = 1.6$
- ITO (non absorbing): constant $n = 1.8$
- ITO (absorbing): the complex refractive index was extracted from the total absorption (as measured with a Cary-Varian spectrometer with an integrating sphere attachment). The absorption coefficient allows for the straightforward calculation of the refractive index imaginary part ($\alpha = 4\pi\kappa/\lambda$). Since the complex function $n = n_r + i\kappa$ is analytical, it has to satisfy Kramers-Kronig equations. This allows for the determination of the ITO complex refractive index used along the simulations. The obtained values were fitted accordingly with Lumerical built-in multi-coefficient model.
- The ALD deposited TiO_2 was was modelled by a dielectric medium with constant n = 2.1.
- Au complex refractive index was taken from Lumerical database, corresponding to Johnson and Christy [181]. The experimental data was then fitted accordingly with Lumerical built-in multi-coefficient model.

Simulation parameters: The structure was simulated by using symmetric and anti-symmetric boundary conditions in the $x - y$ directions, and perfectly matching layers in the z-direction in such a way a unit cell of the plasmonic crystal was reproduced.

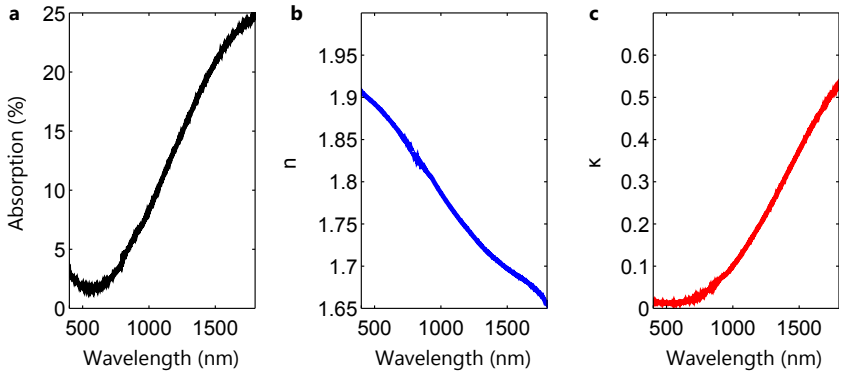

Figure A.1: ITO absorption and optical properties. (a) Absorption, (b) real part and (c) imaginary part of the complex refractive index.

A x-polarized plane wave source was employed to excite the structure. 3D monitors were used to record both the electric field and complex index of refraction at every coordinate of interest; these data were later used to calculate the absorbed power within the Au structure. Auto shut-off conditions guaranteed that the energy in the unit cell decreased 50 dB from initial excitation state. An override mesh of 1 nm was forced within the Au metal. Conformal-variant 2 solver was employed for FDTD calculations. Angle dependent illumination was achieved by the modification of the angle of the incident plane wave in conjunction with Bloch boundary conditions with at least 128 PML layers to avoid artificial back-reflections.

Material characterization

Atomic-Force-Microscopy: atomic force microscopy (AFM) studies were carried out using a Vecco Dimension 3100 system in tapping mode.

Absorption Measurements: total absorption of the films was measured using a Cary 5000 UVVISNIR spectrophotometer with an integrating sphere attachment. The size of the samples was 1 in. $\times$ 1 in. to match reflection and transmission ports. For samples in chapter 5, absorption for non-transmitting samples was calculated from measured reflectance as $A = 1 - R$, and the Reflectance measured using an Agilent 660 FTIR system attached to a microscope with a 4X objective (NA 0.1) and a spatial mask.

Optoelectric characterization

Photovoltaic performance: all device characterization was performed in ambient conditions. Current-voltage characteristics were recorded using a Keithley 2400 source meter. Illumination intensity of AM 1.5 was accomplished using a solar simulator (Newport Oriel Sol3A class AAA). A shadow mask was placed before illuminated devices so that incident light area matches with the device area.

Capacitance-voltage spectroscopy: capacitance-voltage characteristics were measured using an Agilent E4980A LCR meter, with an AC signal modulation of 1 kHz and 50 mV amplitude.

External-Quantum-Efficiency: for the spectral characterization, devices were illuminated by a Newport Cornerstone 260 monochromator modulated with a 20 Hz chopper and the short circuit current was measured with a Stanford Research System SR830 Lock-In amplifier. This was done by either (*i*) monitoring the voltage drop through an in series resistor of 500Ω while fixing the operating conditions with a Keithley 2400, or (*ii*) directly measuring in current mode when possible. Lock-in integration time and filter slope rate were set respectively to 1s and 24dB/oct. To avoid impedance mismatches, the obtained spectra were normalized to the responsivities measured under 406 nm laser illumination with a frequency of 50-100 mHz and a power density of 2 mW/cm^2 (Keithley 2636 source meter). For devices in chapter 5, a more sophisticated method in order to discard noise traces was used. At every wavelength 200 consecutive measurements were recorded, and obtained the average and standard deviation. A threshold was set to the standard deviation of the monitored phase, so that deviations in excess of 2°were considered out-of-phase and attributed to noise.

Responsivity as a function of bias (chapter 5): responsivity measurements with respect to bias were taken under a 635 nm laser illumination with a frequency of 100 mHz and a power density of 3 mW/cm^2. The current was measured with a Keithley 2636 source meter. Short-pulsed illumination was achieved with a 4-channel Thorlabs laser controlled by an Agilent 33220A waveform generator, or alternatively with a NKT Photonics supercontinuum laser source and recorded with an Agilent B1500A semiconductor parameter analizer.

Responsivity as a function of irradiance (chapter 5): the photocurrent-power dependence was acquired at short-circuit conditions with a Stanford Research System SR830 under 635 nm diode laser illumination from Newport (LQA635-08C) controlled by an Agilent 33220A waveform generator.

B

Tunnelling Mechanisms in MIS Junctions

In this appendix we present the analytic dependence of the main tunnelling currents in MIS systems, previously introduced in chapter 3 and depicted in Figure 3.11.

Fowler-Nordheim tunnelling

Fowler-Nordheim (FN) tunnelling, also referred to as field emission, is the electron tunnelling through a potential barrier under the presence of an intense electric field (typically on the order of 10 MeV/cm). It is characterized by a triangular barrier shape in the region where electrons tunnel (see Figure 3.11). The current density is given by [171],

$$J_{FN} = \frac{q^3 m_0}{4 m_\perp \hbar \phi_0} |\mathbf{E_b}|^2 \exp\left(-\frac{4\sqrt{2 m_\perp \phi_0^3}}{3q\hbar|\mathbf{E_b}|}\right) \tag{B.1}$$

where $m_\perp$ is the electron (hole) mass in the oxide (in the direction of propagation), m_0 the free electron mass, $\hbar$ the modified Plank constant, q the elementary charge, ϕ_0 the potential barrier height carriers need to tunnel through and $\mathbf{E_b}$ the electric field across the barrier. Taking into account that $|\mathbf{E_b}| \simeq V/d$, plots of $\ln J/V^2$ vs. $1/V$ (the so-called Fowler-Nordheim plot) and $\ln J$ vs. d should be linear.

Direct tunnelling

This case corresponds to the tunnelling of carriers through the energy interval below the triangular region. Different models exist to account for the complex trapezoidal barrier when there is a significant field through the insulator. In the case of a pure rectangular barrier expressions are highly simplified,

$$J_{DT} = \frac{4\pi q m_\perp}{h^3} \int_0^\infty \exp\left(-2d\sqrt{\frac{2m_\perp(E - q\phi_0)}{\hbar^2}}\right) dE \tag{B.2}$$

In all cases the dependence with $-d$ is exponential.

Trap-assisted tunneling

Trap-assisted tunnelling (TAT) consists of trap-mediated carrier injection through the insulator. TAT is a two-step process where electrons tunnel first into a trap state, and subsequently to another trap to eventually reach the conduction band of the insulator or the semiconductor. TAT processes can be elastic or inelastic depending on whether or not they undergo energy loss by phonon interaction. Different TAT models exist that account for different barrier profiles and trap-to-trap injection.

Hopping conduction

This conduction mechanism describes thermally activated electron transport between one or more sites. It is an incoherent process and follows the Arrhenius relation with temperature,

$$J_H \propto |\mathbf{E_b}| \prod_i \exp\left(-\Delta E_{a,i}/kT\right) \tag{B.3}$$

where $E_{a,i}$ the activation energy of a particular site i. This tunnelling mechanism is usually related to inelastic TAT through a series of trap sites within the insulator barrier.

Poole-Frenkel tunnelling

Is a TAT process relying on interstitial hopping between insulator traps. In this picture, traps behave as potential wells with an electric field dependent depth. Injected carriers undergo field-enhanced thermal motion until they reach the conduction band of the semiconductor. It can be described by a drift current with a carrier density that depends on the depth of the traps as,

$$J_{PF} = qn_0\mu\mathbf{E} \exp\left\{(-\frac{q}{kT})\left(\phi_a - \sqrt{\frac{qV}{d\pi\epsilon}}\right)\right\} \tag{B.4}$$

A $\ln J_{PF}$ vs. $1/T$, $\ln J_{PF}/V$ vs. $V^{1/2}$ and $\ln J_{PF}$ vs. $d^{1/2}$ should be linear.

Schottky-like emission

In a similar way electrons are emitted in metal-semiconductor junctions (the so called thermionic emission), thermally excited electrons can be emitted across the metal-insulator barrier contributing to carrier transport (Figure 3.11). The general theory for thermionic emission was developed by Bethe [182]. In this model, the barrier profile does not affect injection, which is solely determined by the barrier height. The associated thermionic current can be derived as,

$$J = A^* T^2 \exp\left(-\frac{q\phi}{kT}\right) \tag{B.5}$$

where A^* is the material dependent Richardson constant. If image-field effects are included:

$$\Delta\phi_b = \sqrt{\frac{q|\mathbf{E}|}{4\pi\epsilon}} \tag{B.6}$$

where $\mathbf{E}$ is the applied field, and ϵ the permittivity of the insulator layer. By taking into account that $V = |\mathbf{E}|/d$,

$$J = A^* T^2 \exp\left(-\frac{q\phi}{kT}\right) \exp\left(\frac{V^{1/2} q^{3/2}}{2kT\epsilon^{1/2} d^{1/2}}\right) \tag{B.7}$$

Therefore, plots of $\ln J/T^2$ vs. $1/T$, $\ln J$ vs. $V^{1/2}$ and $\ln J$ vs. $d^{1/2}$ should be linear.

C

Analytical Model for Hot-Electron Injection

In this appendix we develop an analytical model to describe plasmonic hot electron injection as a function of plasmonic excitation and barrier configuration. The description of the junction is shown in Figure C.1 together with the main model parameters.

Before electrical contact

Prior to electrical contact the relevant material properties are:

- Metal: Fermi energy (E_F).
- Insulator: electron affinity (χ_{ins}) and thickness (d).
- Semiconductor: electron affinity (χ_{sc}), Fermi level ($E_{F,sc}$), bandgap E_g, carrier concentration (N_d), permittivity (ϵ_s) and thickness (t_s). Surface trap states are henceforth omitted.

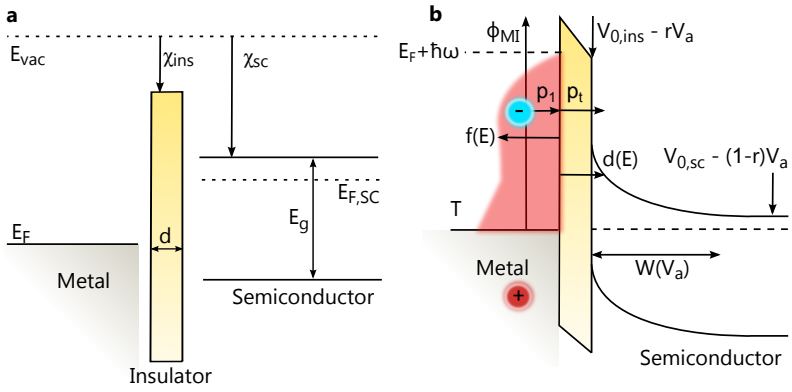

Figure C.1: Barrier modelling and hot electron injection. (a) Before contact materials can be characterized by their bulk electronic and geometric properties. (b) Situation after contact, once in thermal equilibrium.

After electrical contact

Once in contact, charges redistribute until equilibrium is reached (panel b). The resulting MIS junction is characterized by the next parameters:

- Barrier height (ϕ_{MI}), dictated by the difference in χ_{ins} and E_F.
- Voltage drop across the insulator ($V_{0,ins} - rV_a$). It corresponds to the drop at thermal equilibrium minus the drop with applied voltage. The factor r is calculated from the relative resistance of the insulator and semiconductor.
- Voltage drop across the semiconductor ($V_{0,sc} - (1-r)V_a$), it corresponds to the drop at thermal equilibrium minus the drop with applied voltage, which is complementary to the one falling at the insulator.
- Depletion width (W) in the semiconductor. It can be calculated as,

$$W = \sqrt{\frac{q\epsilon_0\epsilon_s(V_{0,sc} - (1-r)V_a)}{2N_d}}. \tag{C.1}$$

  It is a function of the aforementioned parameters and applied bias.
- Barrier profile ($d(E)$). It determines the distance from the metal-insulator plane to a conduction band state in the semiconductor. It also depends on the applied bias.

Hot-electron population

Once illuminated, light impinging into the metal can be absorbed, transmitted or reflected. As described in chapter 2, metal absorption can take place via interband or intraband transitions, or through plasmon excitation. Excited plasmons can loss their energy by promoting electrons within the conduction band. The generated hot-electron population has a complex functional density $f(E,t,r)$ that depends on time, energy, geometry and position. Calculations for f have been reported through quantum density functional theory calculations (QDFT) or semi-classical descriptions for simplified geometries [65,170,176]; for more complex structures it is instead often approximated by more manageable analytical expressions:

- Dirac-like: in this approximation all electrons are concentrated at $\hbar\omega$ above the metal Fermi level. This assumption has been considered in some theoretical models [118]. The probability function is defined here as,

$$f(E) = \delta(E - \hbar\omega_p) \tag{C.2}$$

- Uniform: the excited hot-electron population will span across E_F and $E_F + \hbar\omega_p$. Other models rely on this assumption [101]. Its analytical expression,

$$f(E) = \begin{cases} 1/\hbar\omega & \text{if } E \in [E_F, E_F + \hbar\omega_p] \\ 0 & \text{elsewhere} \end{cases} \tag{C.3}$$

Although overlooking some aspects of plasmonic hot-electron generation, such as the influence of metal topology [163], they can be used to qualitatively describe the main physics behind hot-electron generation and help describe its collection [101]. We have therefore relied on this approximation. The total density of generated electrons is obtained by combining the occupation probability $f(E)$ with the density of available states $g(E)$:

$$n(E) = g(E)f(E) \tag{C.4}$$

The hot-electron injection mechanism is typically described in a three-steps process [67]:

Step 1: from the metal to the interface

As discussed in chapter 6, different approaches exist to describe electron transport from the metal bulk to the interface. The energy-loss travelling electrons might undergo during that process, is reflected by an emission cone that effectively limits the amount of electrons with enough energy to abandon the metal. For this step we consider an emission cone defined by the mean-free-path and decay length that we have introduced in chapter 6.

Step 2: tunnelling probability

The transmission probability ($p_2(E)$) can be calculated by solving the Schrödinger equation for a given barrier profile $d(E, V_a)$. Solutions are often obtained by employing the Wentzel-Kramers-Brillouin (WKB) approximation. The tunnelling for an arbitrary shaped barrier can be solved as,

$$p_2(E, V) = \exp -2\sqrt{\frac{8\pi^2 m}{h^2}} \int_0^{d(E,V)} \sqrt{E - E(x)}dx \tag{C.5}$$

where m is the electron mass and E_i the energy of a particular tunneling state. In the case of a triangular barrier it can be solved as,

$$p_2(E, V) = \exp -\frac{4}{3}\frac{\sqrt{2m}}{\hbar}\frac{(E - \phi_{MI})^{3/2}}{qF} \tag{C.6}$$

where F is the electric field across the insulator, that can be calculated as,

$$F = \frac{V_{0,ins} - rV_a}{d} \tag{C.7}$$

Fitting

The model introduced along this appendix has been used to fit the experimental responsivity of the plasmonic crystal photodetector shown in section 5.4. Obtained injection values approach unity under reverse bias conditions. Curves have been scaled according to the responsivity in saturation. Fitting values have been taken from the employed materials and device configuration, as listed in table C.1. Hot-electron population, barrier profile, tunnelling probability and injected carriers are illustrated in Figure C.2 for single point calculations (λ = 640 nm) under 0V, -2V, and -4V reverse bias. A 2D-sweep along wavelength and bias is shown in Figure C.3, where the shift in onset and saturation voltages can be clearly appreciated.

Table C.1: Fitting parameters to model hot-electron injection.

Material parameters	
E_F	-5.1 eV
χ_{ins}	-2.6 eV
d_{ins}	0.6 nm
χ_{sc}	-4.1 eV
$E_{F,sc}$	-4.3 eV
E_g	3.2 eV
N_d	$7 \cdot 10^{14}$ cm^{-3}
ϵ_s	30
t_s	60 nm
T	293 K

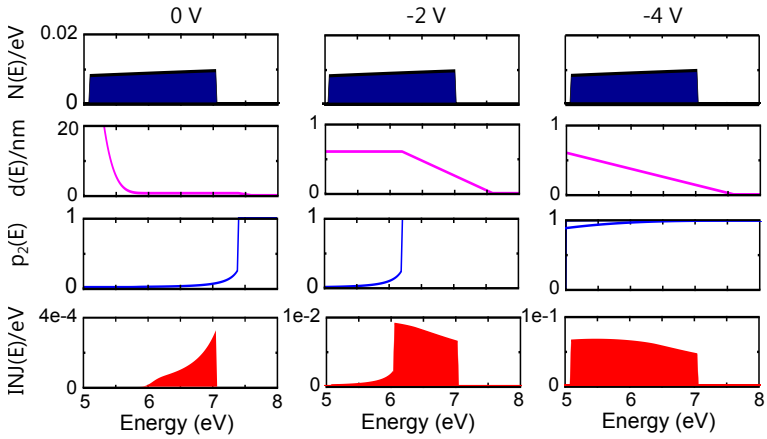

Figure C.2: Calculation of hot-electron injection for different biases. From top to bottom: hot-electron population, barrier profile, tunnelling probability and density of injected electrons. From left to right: 0V, -2V and -4V.

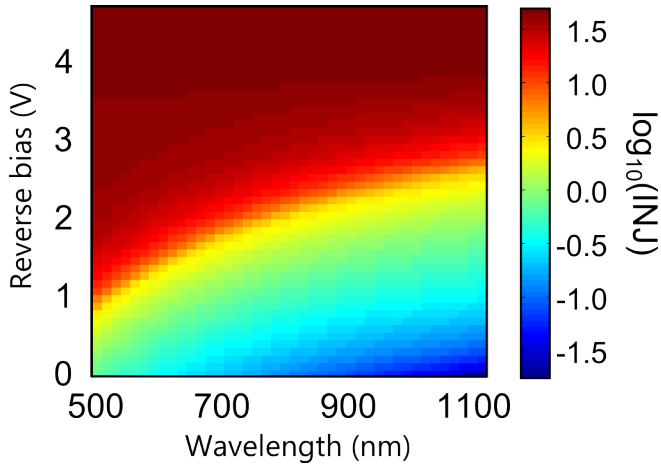

Figure C.3: 2D map of hot-electron injection as a function of wavelength and reverse bias.

Bibliography

[1] J. Henzie, J. Lee, M. H. Lee, W. Hasan, and T. W. Odom, "Nanofabrication of plasmonic structures," *Annual review of physical chemistry*, vol. 60, pp. 147–65, Jan. 2009. (see p. 2)

[2] N. Liu, M. Mesch, T. Weiss, M. Hentschel, and H. Giessen, "Infrared perfect absorber and its application as plasmonic sensor.," *Nano letters*, vol. 10, pp. 2342–8, July 2010. (see p. 2)

[3] M. K. Hedayati, M. Javaherirahim, B. Mozooni, R. Abdelaziz, A. Tavassolizadeh, V. S. K. Chakravadhanula, V. Zaporojtchenko, T. Strunkus, F. Faupel, and M. Elbahri, "Perfect Plasmonic Absorber: Design of a Perfect Black Absorber at Visible Frequencies Using Plasmonic Metamaterials (Adv. Mater. 45/2011)," *Advanced Materials*, vol. 23, pp. 5409–5409, Dec. 2011. (see pp. 2 and 9)

[4] A. Tittl, P. Mai, R. Taubert, D. Dregely, N. Liu, and H. Giessen, "Palladium-based plasmonic perfect absorber in the visible wavelength range and its application to hydrogen sensing.," *Nano letters*, vol. 11, pp. 4366–9, Oct. 2011. (see pp. 2 and 9)

[5] Z. Fang, Y.-R. Zhen, L. Fan, X. Zhu, and P. Nordlander, "Tunable wide-angle plasmonic perfect absorber at visible frequencies," *Physical Review B*, vol. 85, June 2012. (see pp. 2 and 9)

[6] W. Li and J. Valentine, "Metamaterial Perfect Absorber Based Hot Electron Photodetection.," *Nano letters*, vol. 14, pp. 3510–3514, May 2014. (see pp. 2 and 16)

[7] A. G. Brolo, "Plasmonics for future biosensors," *Nature Photonics*, vol. 6, pp. 709–713, Nov. 2012. (see p. 2)

[8] M. Xiao, R. Jiang, F. Wang, C. Fang, J. Wang, and J. C. Yu, "Plasmon-enhanced chemical reactions," *Journal of Materials Chemistry A*, vol. 1, p. 5790, Apr. 2013. (see p. 2)

[9] G. Baffou and R. Quidant, "Nanoplasmonics for chemistry.," *Chemical Society reviews*, vol. 43, pp. 3898–907, June 2014. (see pp. 2 and 12)

[10] Y. B. Zheng, B. Kiraly, P. S. Weiss, and T. J. Huang, "Molecular plasmonics for biology and nanomedicine.," *Nanomedicine (London, England)*, vol. 7, pp. 751–70, May 2012. (see p. 2)

[11] O. Tokel, F. Inci, and U. Demirci, "Advances in plasmonic technologies for point of care applications.," *Chemical reviews*, vol. 114, pp. 5728–52, June 2014. (see p. 2)

[12] D. O'Connor and A. V. Zayats, "Data storage: The third plasmonic revolution.," *Nature nanotechnology*, vol. 5, pp. 482–3, July 2010. (see p. 3)

[13] M. Kauranen and A. V. Zayats, "Nonlinear plasmonics," *Nature Photonics*, vol. 6, pp. 737–748, Nov. 2012. (see pp. 3 and 66)

[14] M. Geiselmann, M. L. Juan, J. Renger, J. M. Say, L. J. Brown, F. J. G. de Abajo, F. Koppens, and R. Quidant, "Three-dimensional optical manipulation of a single electron spin.," *Nature nanotechnology*, vol. 8, pp. 175–9, Mar. 2013. (see p. 3)

[15] H. A. Atwater and A. Polman, "Plasmonics for improved photovoltaic devices," *Nature Materials*, vol. 9, no. 3, pp. 205–213, 2010. (see pp. 3 and 9)

[16] W. Hou and S. B. Cronin, "A Review of Surface Plasmon Resonance-Enhanced Photocatalysis," *Advanced Functional Materials*, vol. 23, pp. 1612–1619, Apr. 2013. (see p. 3)

[17] L. Tong, H. Wei, S. Zhang, and H. Xu, "Recent advances in plasmonic sensors.," *Sensors (Basel, Switzerland)*, vol. 14, pp. 7959–73, Jan. 2014. (see p. 3)

[18] G. Konstantatos and E. H. Sargent, "Nanostructured materials for photon detection.," *Nature nanotechnology*, vol. 5, pp. 391–400, June 2010. (see pp. 3 and 20)

[19] K. R. Catchpole, S. Mokkapati, F. Beck, E.-C. Wang, A. McKinley, A. Basch, and J. Lee, "Plasmonics and nanophotonics for photovoltaics," *MRS Bulletin*, vol. 36, pp. 461–467, June 2011. (see pp. 3 and 9)

[20] C. Fei Guo, T. Sun, F. Cao, Q. Liu, and Z. Ren, "Metallic nanostructures for light trapping in energy-harvesting devices," *Light: Science & Applications*, vol. 3, p. e161, Apr. 2014. (see pp. 3 and 9)

[21] D. Derkacs, S. H. Lim, P. Matheu, W. Mar, and E. T. Yu, "Improved performance of amorphous silicon solar cells via scattering from surface plasmon polaritons in nearby metallic nanoparticles," *Applied Physics Letters*, vol. 89, p. 093103, Aug. 2006. (see p. 4)

[22] S. Pillai, K. R. Catchpole, T. Trupke, and M. A. Green, "Surface plasmon enhanced silicon solar cells," *Journal of Applied Physics*, vol. 101, p. 093105, May 2007. (see p. 4)

[23] P. Matheu, S. H. Lim, D. Derkacs, C. McPheeters, and E. T. Yu, "Metal and dielectric nanoparticle scattering for improved optical absorption in photovoltaic devices," *Applied Physics Letters*, vol. 93, p. 113108, Sept. 2008. (see p. 4)

[24] D. Derkacs, W. V. Chen, P. M. Matheu, S. H. Lim, P. K. L. Yu, and E. T. Yu, "Nanoparticle-induced light scattering for improved performance of quantum-well solar cells," *Applied Physics Letters*, vol. 93, p. 091107, Sept. 2008. (see p. 4)

[25] K. Nakayama, K. Tanabe, and H. Atwater, "Plasmonic nanoparticle enhanced light absorption in GaAs solar cells," *Applied Physics Letters*, vol. 93, p. 121904, 2008. (see p. 4)

[26] K. R. Catchpole and A. Polman, "Plasmonic solar cells," *Optics Express*, vol. 16, no. 26, pp. 21793–21800, 2008. (see p. 4)

[27] F. J. Beck, A. Polman, and K. R. Catchpole, "Tunable light trapping for solar cells using localized surface plasmons," *Journal of Applied Physics*, vol. 105, p. 114310(7), 2009. (see p. 4)

[28] R. A. Pala, J. White, E. Barnard, J. Liu, and M. L. Brongersma, "Design of Plasmonic Thin-Film Solar Cells with Broadband Absorption Enhancements," *Advanced Materials*, vol. 21, pp. 3504–3509, Sept. 2009. (see p. 4)

[29] H. Tan, R. Santbergen, A. H. M. Smets, and M. Zeman, "Plasmonic light trapping in thin-film silicon solar cells with improved self-assembled silver nanoparticles.," *Nano letters*, vol. 12, pp. 4070–6, Aug. 2012. (see p. 4)

[30] P. Spinelli, V. E. Ferry, J. van de Groep, M. van Lare, M. A. Verschuuren, R. E. I. Schropp, H. A. Atwater, and A. Polman, "Plasmonic light trapping in thin-film Si solar cells," *Journal of Optics*, vol. 14, p. 024002, Feb. 2012. (see p. 4)

[31] M. J. Mendes, S. Morawiec, F. Simone, F. Priolo, and I. Crupi, "Colloidal plasmonic back reflectors for light trapping in solar cells.," *Nanoscale*, vol. 6, pp. 4796–805, May 2014. (see p. 4)

[32] F. J. Beck, T. Lasanta, and G. Konstantatos, "Plasmonic Schottky Nanojunctions for Tailoring the Photogeneration Profile in Thin Film Solar Cells," *Advanced Optical Materials*, vol. 2, pp. 493–500, May 2014. (see p. 4)

[33] H. R. Stuart and D. G. Hall, "Absorption enhancement in silicon-on-insulator waveguides using metal island films," *Applied Physics Letters*, vol. 69, no. June, pp. 2327–2329, 1996. (see p. 4)

[34] H. R. Stuart and D. G. Hall, "Island size effects in nanoparticle-enhanced photodetectors," *Applied Physics Letters*, vol. 73, p. 3815, Dec. 1998. (see p. 4)

[35] D. M. Schaadt, B. Feng, and E. T. Yu, "Enhanced semiconductor optical absorption via surface plasmon excitation in metal nanoparticles," *Applied Physics Letters*, vol. 86, no. 6, p. 063106, 2005. (see p. 4)

[36] F. Pelayo Garcia de Arquer, F. J. Beck, M. Bernechea, and G. Konstantatos, "Plasmonic light trapping leads to responsivity increase in colloidal quantum dot photodetectors," *Applied Physics Letters*, vol. 100, p. 043101, Jan. 2012. (see p. 4)

[37] F. J. Beck, F. P. Garcia de Arquer, M. Bernechea, and G. Konstantatos, "Electrical effects of metal nanoparticles embedded in ultra-thin colloidal quantum dot films," *Applied Physics Letters*, vol. 101, p. 041103, July 2012. (see p. 4)

[38] F. J. Beck, A. Stavrinadis, S. L. Diedenhofen, T. Lasanta, and G. Konstantatos, "Surface Plasmon Polariton Couplers for Light Trapping in Thin-Film Absorbers and Their Application to Colloidal Quantum Dot Optoelectronics," *ACS Photonics*, p. 141007152154008, Oct. 2014. (see p. 4)

[39] L.-B. Luo, L.-H. Zeng, C. Xie, Y.-Q. Yu, F.-X. Liang, C.-Y. Wu, L. Wang, and J.-G. Hu, "Light trapping and surface plasmon enhanced high-performance NIR photodetector.," *Scientific reports*, vol. 4, p. 3914, Jan. 2014. (see p. 4)

[40] M. D. Brown, T. Suteewong, R. S. S. Kumar, V. D'Innocenzo, A. Petrozza, M. M. Lee, U. Wiesner, and H. J. Snaith, "Plasmonic dye-sensitized solar cells using core-shell metal-insulator nanoparticles.," *Nano letters*, vol. 11, pp. 438–45, Feb. 2011. (see p. 4)

[41] D. Zhang, W. C. H. Choy, F. Xie, W. E. I. Sha, X. Li, B. Ding, K. Zhang, F. Huang, and Y. Cao, "Plasmonic Electrically Functionalized TiO2 for High-Performance

Organic Solar Cells," *Advanced Functional Materials*, vol. 23, pp. 4255–4261, Sept. 2013. (see pp. 4 and 12)

[42] D. Paz-Soldan, A. Lee, S. M. Thon, M. M. Adachi, H. Dong, P. Maraghechi, M. Yuan, A. J. Labelle, S. Hoogland, K. Liu, E. Kumacheva, and E. H. Sargent, "Jointly tuned plasmonic-excitonic photovoltaics using nanoshells.," *Nano letters*, vol. 13, pp. 1502–8, Apr. 2013. (see p. 4)

[43] Q. Gan, F. J. Bartoli, and Z. H. Kafafi, "Plasmonic-enhanced organic photovoltaics: breaking the 10% efficiency barrier.," *Advanced materials (Deerfield Beach, Fla.)*, vol. 25, pp. 2385–96, May 2013. (see p. 4)

[44] H. Choi, S.-J. Ko, Y. Choi, P. Joo, T. Kim, B. R. Lee, J.-W. Jung, H. J. Choi, M. Cha, J.-R. Jeong, I.-W. Hwang, M. H. Song, B.-S. Kim, and J. Y. Kim, "Versatile surface plasmon resonance of carbon-dot-supported silver nanoparticles in polymer optoelectronic devices," *Nature Photonics*, vol. 7, pp. 732–738, July 2013. (see p. 4)

[45] V. E. Ferry, L. A. Sweatlock, D. Pacifici, and H. A. Atwater, "Plasmonic Nanostructure Design for Efficient Light Coupling into Solar Cells," *Nano Letters*, vol. 8, no. 12, pp. 4391–4397, 2008. (see p. 4)

[46] T. Ishi, J. Fujikata, K. Makita, T. Baba, and K. Ohashi, "Si Nano-Photodiode with a Surface Plasmon Antenna," *Japanese Journal of Applied Physics*, vol. 44, no. No. 12, pp. L364–L366, 2005. (see p. 4)

[47] L. Tang, S. E. Kocabas, S. Latif, A. K. Okyay, D.-S. Ly-Gagnon, K. C. Saraswat, and D. A. B. Miller, "Nanometre-scale germanium photodetector enhanced by a near-infrared dipole antenna," *Nature Photonics*, vol. 2, pp. 226–229, Mar. 2008. (see p. 4)

[48] F.-F. Ren, K.-W. Ang, J. Ye, M. Yu, G.-Q. Lo, and D.-L. Kwong, "Split Bull's eye shaped aluminum antenna for plasmon-enhanced nanometer scale germanium photodetector.," *Nano letters*, vol. 11, pp. 1289–93, Mar. 2011. (see p. 4)

[49] J. Liu, Y. Wang, and D. Sun, "Enhancing the performance of dye-sensitized solar cells by benzoic acid modified TiO2 nanorod electrode," *Renewable Energy*, vol. 38, pp. 214–218, Feb. 2012. (see p. 4)

[50] R. Fowler, "The Analysis of Photoelectric Sensitivity Curves for Clean Metals at Various Temperatures," *Physical Review*, vol. 38, pp. 45–56, July 1931. (see pp. 5 and 10)

[51] G. Zhao, H. Kozuka, and T. Yoko, "Sol-gel preparation and photoelectrochemical properties of TiO2 films containing Au and Ag metal particles," *Thin Solid Films*, vol. 277, pp. 147–154, May 1996. (see pp. 6 and 12)

[52] Y. Tian and T. Tatsuma, "Plasmon-induced photoelectrochemistry at metal nanoparticles supported on nanoporous TiO2.," *Chemical communications (Cambridge, England)*, pp. 1810–1, Aug. 2004. (see pp. 6, 12, 16, and 19)

[53] C. Clavero, "Plasmon-induced hot-electron generation at nanoparticle/metal-oxide interfaces for photovoltaic and photocatalytic devices," *Nature Photonics*, vol. 8, pp. 95–103, Jan. 2014. (see pp. 6, 12, and 66)

[54] K. Marchuk and K. A. Willets, "Localized surface plasmons and hot electrons," *Chemical Physics*, vol. 445, pp. 95–104, Oct. 2014. (see p. 6)

[55] D. Liu, S. J. Clark, and J. Robertson, "Oxygen vacancy levels and electron transport in Al2O3," *Applied Physics Letters*, vol. 96, p. 032905, Jan. 2010. (see p. 9)

[56] S. Link and M. A. El-Sayed, "Shape and size dependence of radiative, non-radiative and photothermal properties of gold nanocrystals," *International Reviews in Physical Chemistry*, vol. 19, pp. 409–453, July 2000. (see p. 10)

[57] G. V. Hartland, "Optical studies of dynamics in noble metal nanostructures.," *Chemical reviews*, vol. 111, pp. 3858–87, June 2011. (see pp. 10 and 11)

[58] K. Kolwas and A. Derkachova, "Damping rates of surface plasmons for particles of size from nano- to micrometers; reduction of the nonradiative decay," *Journal of Quantitative Spectroscopy and Radiative Transfer*, vol. 114, pp. 45–55, Jan. 2013. (see pp. 10 and 79)

[59] K. O. Aruda, M. Tagliazucchi, C. M. Sweeney, D. C. Hannah, and E. A. Weiss, "The role of interfacial charge transfer-type interactions in the decay of plasmon excitations in metal nanoparticles.," *Physical chemistry chemical physics : PCCP*, vol. 15, pp. 7441–9, May 2013. (see p. 10)

[60] M. Aeschlimann, M. Bauer, and S. Pawlik, "Competing nonradiative channels for hot electron induced surface photochemistry," *Chemical Physics*, vol. 205, pp. 127–141, Apr. 1996. (see p. 10)

[61] L. DuBridge, "Theory of the Energy Distribution of Photoelectrons," *Physical Review*, vol. 43, pp. 727–741, May 1933. (see p. 10)

[62] G. Mahan, "Theory of Photoemission in Simple Metals," *Physical Review B*, vol. 2, pp. 4334–4350, Dec. 1970. (see p. 10)

[63] G. Herink, D. R. Solli, M. Gulde, and C. Ropers, "Field-driven photoemission from nanostructures quenches the quiver motion.," *Nature*, vol. 483, pp. 190–3, Mar. 2012. (see p. 10)

[64] M. W. Knight, Y. Wang, A. S. Urban, A. Sobhani, B. Y. Zheng, P. Nordlander, and N. J. Halas, "Embedding plasmonic nanostructure diodes enhances hot electron emission.," *Nano letters*, vol. 13, pp. 1687–92, Apr. 2013. (see pp. 10, 14, 16, and 70)

[65] A. Manjavacas, J. G. Liu, V. Kulkarni, and P. Nordlander, "Plasmon-Induced Hot Carriers in Metallic Nanoparticles.," *ACS nano*, July 2014. (see pp. 10 and 99)

[66] H. Kanter, "Slow-Electron Mean Free Paths in Aluminum, Silver, and Gold," *Physical Review B*, vol. 1, pp. 522–536, Jan. 1970. (see p. 12)

[67] W. E. Spicer and A. Herrera-Gomez, "Modern theory and applications of photocathodes," in *SPIE's 1993 International Symposium on Optics, Imaging, and Instrumentation* (K. J. Kaufmann, ed.), pp. 18–35, International Society for Optics and Photonics, Oct. 1993. (see pp. 12 and 100)

[68] Y. Tian and T. Tatsuma, "Mechanisms and applications of plasmon-induced charge separation at TiO2 films loaded with gold nanoparticles.," *Journal of the American Chemical Society*, vol. 127, pp. 7632–7, May 2005. (see p. 12)

[69] T. Lana-Villarreal and R. Gómez, "Tuning the photoelectrochemistry of nanoporous anatase electrodes by modification with gold nanoparticles: Development of cathodic photocurrents," *Chemical Physics Letters*, vol. 414, pp. 489–494, Oct. 2005. (see p. 12)

[70] K. Yu, Y. Tian, and T. Tatsuma, "Size effects of gold nanaoparticles on plasmon-induced photocurrents of gold-TiO2 nanocomposites.," *Physical chemistry chemical physics : PCCP*, vol. 8, pp. 5417–20, Dec. 2006. (see pp. 12, 16, and 79)

[71] N. Sakai, Y. Fujiwara, Y. Takahashi, and T. Tatsuma, "Plasmon-resonance-based generation of cathodic photocurrent at electrodeposited gold nanoparticles coated with TiO2 films.," *Chemphyschem : a European journal of chemical physics and physical chemistry*, vol. 10, pp. 766–9, Mar. 2009. (see pp. 12 and 16)

[72] E. Kowalska, R. Abe, and B. Ohtani, "Visible light-induced photocatalytic reaction of gold-modified titanium(IV) oxide particles: action spectrum analysis.,"

Chemical communications (Cambridge, England), pp. 241–3, Jan. 2009. (see pp. 12 and 16)

[73] T. Toyoda, S. Tsugawa, and Q. Shen, "Photoacoustic spectra of Au quantum dots adsorbed on nanostructured TiO2 electrodes together with the photoelectrochemical current characteristics," *Journal of Applied Physics*, vol. 105, p. 034314, Feb. 2009. (see pp. 12 and 16)

[74] C. G. Silva, R. Juárez, T. Marino, R. Molinari, and H. García, "Influence of excitation wavelength (UV or visible light) on the photocatalytic activity of titania containing gold nanoparticles for the generation of hydrogen or oxygen from water.," *Journal of the American Chemical Society*, vol. 133, pp. 595–602, Jan. 2011. (see p. 12)

[75] E. Kowalska, O. O. P. Mahaney, R. Abe, and B. Ohtani, "Visible-light-induced photocatalysis through surface plasmon excitation of gold on titania surfaces.," *Physical chemistry chemical physics : PCCP*, vol. 12, pp. 2344–55, Mar. 2010. (see p. 12)

[76] Y. Ide, M. Matsuoka, and M. Ogawa, "Efficient visible-light-induced photocatalytic activity on gold-nanoparticle-supported layered titanate.," *Journal of the American Chemical Society*, vol. 132, pp. 16762–4, Dec. 2010. (see p. 12)

[77] N. Sakai, T. Sasaki, K. Matsubara, and T. Tatsuma, "Layer-by-layer assembly of gold nanoparticles with titania nanosheets: control of plasmon resonance and photovoltaic properties," *Journal of Materials Chemistry*, vol. 20, p. 4371, May 2010. (see p. 12)

[78] X. Tian, J. Xu, and W. Xie, "Controllable Modulation of the Electronic Structure of ZnO (10\={1}0) Surface by Carboxylic Acids," pp. 3973–3980, 2010. (see p. 12)

[79] A. Tanaka, A. Ogino, M. Iwaki, K. Hashimoto, A. Ohnuma, F. Amano, B. Ohtani, and H. Kominami, "Gold-titanium(IV) oxide plasmonic photocatalysts prepared by a colloid-photodeposition method: correlation between physical properties and photocatalytic activities.," *Langmuir : the ACS journal of surfaces and colloids*, vol. 28, pp. 13105–11, Sept. 2012. (see pp. 12 and 16)

[80] H. M. Chen, C. K. Chen, C.-J. Chen, L.-C. Cheng, P. C. Wu, B. H. Cheng, Y. Z. Ho, M. L. Tseng, Y.-Y. Hsu, T.-S. Chan, J.-F. Lee, R.-S. Liu, and D. P. Tsai, "Plasmon inducing effects for enhanced photoelectrochemical water splitting: X-ray absorption approach to electronic structures.," *ACS nano*, vol. 6, pp. 7362–72, Aug. 2012. (see p. 12)

[81] J. Lee, S. Mubeen, X. Ji, G. D. Stucky, and M. Moskovits, "Plasmonic photoanodes for solar water splitting with visible light.," *Nano letters*, vol. 12, pp. 5014–9, Oct. 2012. (see pp. 12 and 16)

[82] P. Christopher, H. Xin, A. Marimuthu, and S. Linic, "Singular characteristics and unique chemical bond activation mechanisms of photocatalytic reactions on plasmonic nanostructures.," *Nature materials*, vol. 11, pp. 1044–50, Dec. 2012. (see p. 12)

[83] X. Shi, K. Ueno, N. Takabayashi, and H. Misawa, "Plasmon-Enhanced Photocurrent Generation and Water Oxidation with a Gold Nanoisland-Loaded Titanium Dioxide Photoelectrode," *The Journal of Physical Chemistry C*, vol. 117, pp. 2494–2499, Feb. 2013. (see p. 12)

[84] Z. Han, L. Wei, Z. Zhang, X. Zhang, H. Pan, and J. Chen, "Visible-Light Photocatalytic Application of Hierarchical Au-ZnO Flower-Rod Heterostructures via Surface Plasmon Resonance," *Plasmonics*, vol. 8, pp. 1193–1202, Mar. 2013. (see p. 12)

[85] S. Mubeen, J. Lee, N. Singh, S. Krämer, G. D. Stucky, and M. Moskovits, "An autonomous photosynthetic device in which all charge carriers derive from surface plasmons.," *Nature nanotechnology*, vol. 8, pp. 247–51, Apr. 2013. (see pp. 12, 16, 49, 66, and 80)

[86] W. Chen, D. C. Abeysinghe, R. L. Nelson, and Q. Zhan, "Plasmonic Lens Made of Multiple Concentric Metallic Rings under Radially Polarized Illumination," *Nano Letters*, 2009. (see pp. 12 and 37)

[87] P. Reineck, G. P. Lee, D. Brick, M. Karg, P. Mulvaney, and U. Bach, "A Solid-State Plasmonic Solar Cell via Metal Nanoparticle Self-Assembly.," *Advanced Materials*, vol. 24, pp. 4750–4755, June 2012. (see pp. 13, 16, and 49)

[88] F. Wang and N. A. Melosh, "Plasmonic energy collection through hot carrier extraction.," *Nano letters*, vol. 11, pp. 5426–30, Dec. 2011. (see p. 13)

[89] C. Scales and P. Berini, "Thin-Film Schottky Barrier Photodetector Models," *IEEE Journal of Quantum Electronics*, vol. 46, pp. 633–643, May 2010. (see p. 13)

[90] A. L. Falk, F. H. L. Koppens, C. L. Yu, K. Kang, N. de Leon Snapp, A. V. Akimov, M.-H. Jo, M. D. Lukin, and H. Park, "Near-field electrical detection of optical plasmons and single-plasmon sources," *Nature Physics*, vol. 5, pp. 475–479, May 2009. (see pp. 14 and 19)

[91] P. Neutens, P. Van Dorpe, I. De Vlaminck, L. Lagae, and G. Borghs, "Electrical detection of confined gap plasmons in metalinsulatormetal waveguides," *Nature Photonics*, vol. 3, pp. 283–286, Apr. 2009. (see pp. 14 and 19)

[92] I. Goykhman, B. Desiatov, J. Khurgin, J. Shappir, and U. Levy, "Locally oxidized silicon surface-plasmon Schottky detector for telecom regime.," *Nano letters*, vol. 11, pp. 2219–24, June 2011. (see pp. 14 and 16)

[93] M. W. Knight, H. Sobhani, P. Nordlander, and N. J. Halas, "Photodetection with active optical antennas.," *Science (New York, N.Y.)*, vol. 332, pp. 702–4, May 2011. (see p. 14)

[94] J.-S. Lee, M. V. Kovalenko, J. Huang, D. S. Chung, and D. V. Talapin, "Band-like transport, high electron mobility and high photoconductivity in all-inorganic nanocrystal arrays.," *Nature nanotechnology*, vol. 6, pp. 348–52, June 2011. (see pp. 14, 16, and 49)

[95] H. Lee, Y. Keun Lee, T. Nghia Van, and J. Young Park, "Nanoscale Schottky behavior of Au islands on TiO2 probed with conductive atomic force microscopy," *Applied Physics Letters*, vol. 103, p. 173103, Oct. 2013. (see p. 14)

[96] Y. Keun Lee, J. Lee, H. Lee, J.-Y. Lee, and J. Young Park, "Probing polarization modes of Ag nanowires with hot electron detection on Au/TiO2 nanodiodes," *Applied Physics Letters*, vol. 102, p. 123112, Mar. 2013. (see p. 14)

[97] A. Sobhani, M. W. Knight, Y. Wang, B. Zheng, N. S. King, L. V. Brown, Z. Fang, P. Nordlander, and N. J. Halas, "Narrowband photodetection in the near-infrared with a plasmon-induced hot electron device.," *Nature communications*, vol. 4, p. 1643, Jan. 2013. (see p. 14)

[98] A. Giugni, B. Torre, A. Toma, M. Francardi, M. Malerba, A. Alabastri, R. Proietti Zaccaria, M. I. Stockman, and E. Di Fabrizio, "Hot-electron nanoscopy using adiabatic compression of surface plasmons.," *Nature nanotechnology*, vol. 8, pp. 845–52, Nov. 2013. (see pp. 14 and 16)

[99] X. Wang, G. I. Koleilat, J. Tang, H. Liu, I. J. Kramer, R. Debnath, L. Brzozowski, D. A. R. Barkhouse, L. Levina, S. Hoogland, and E. H. Sargent, "Tandem colloidal quantum dot solar cells employing a graded recombination layer," *Nature Photonics*, vol. 5, pp. 480–484, June 2011. (see pp. 14 and 49)

[100] F. Wang and N. A. Melosh, "Power-independent wavelength determination by hot carrier collection in metal-insulator-metal devices.," *Nature communications*, vol. 4, p. 1711, Jan. 2013. (see p. 14)

[101] H. Chalabi, D. Schoen, and M. L. Brongersma, "Hot-Electron Photodetection with a Plasmonic Nanostripe Antenna.," *Nano letters*, vol. 14, pp. 1374–1380, Feb. 2014. (see pp. 14, 16, 34, 49, 62, and 99)

[102] B. P. Motjolopane and R. van Zyl, "A review of rectenna models for electromagnetic energy harvesting," Apr. 2013. (see p. 14)

[103] N. C. Lindquist, P. Nagpal, A. Lesuffleur, D. J. Norris, and S.-h. Oh, "Three-Dimensional Plasmonic Nanofocusing," *Nano Letters*, vol. 10, pp. 1369–1373, 2010. (see p. 15)

[104] C. D. Bain and G. M. Whitesides, "Modeling Organic Surfaces with Self-Assembled Monolayers," *Angewandte Chemie International Edition in English*, vol. 28, pp. 506–512, Apr. 1989. (see p. 15)

[105] A. Pimpin and W. Srituravanich, "Review on Micro- and Nanolithography Techniques and their Applications," *Engineering Journal*, vol. 16, pp. 37–56, Jan. 2012. (see pp. 15, 16, and 50)

[106] Y. Nishijima, K. Ueno, Y. Yokota, K. Murakoshi, and H. Misawa, "Plasmon-Assisted Photocurrent Generation from Visible to Near-Infrared Wavelength Using a Au-Nanorods/TiO 2 Electrode," *The Journal of Physical Chemistry Letters*, vol. 1, pp. 2031–2036, July 2010. (see pp. 16, 19, and 49)

[107] M. W. Knight, H. Sobhani, P. Nordlander, and N. J. Halas, "Photodetection with active optical antennas.," *Science (New York, N.Y.)*, vol. 332, pp. 702–4, May 2011. (see pp. 16, 19, 34, 49, 53, and 81)

[108] A. Sobhani, M. W. Knight, Y. Wang, B. Zheng, N. S. King, L. V. Brown, Z. Fang, P. Nordlander, and N. J. Halas, "Narrowband photodetection in the near-infrared with a plasmon-induced hot electron device.," *Nature communications*, vol. 4, p. 1643, Jan. 2013. (see pp. 16, 48, and 49)

[109] S. Linic, P. Christopher, and D. B. Ingram, "Plasmonic-metal nanostructures for efficient conversion of solar to chemical energy.," *Nature materials*, vol. 10, pp. 911–21, Dec. 2011. (see p. 19)

[110] T. Rauch, M. Böberl, S. F. Tedde, J. Fürst, M. V. Kovalenko, G. Hesser, U. Lemmer, W. Heiss, and O. Hayden, "Near-infrared imaging with quantum-dot-sensitized organic photodiodes," *Nature Photonics*, vol. 3, pp. 332–336, May 2009. (see p. 20)

[111] J. Michel, J. Liu, and L. C. Kimerling, "High-performance Ge-on-Si photodetectors," *Nature Photonics*, vol. 4, pp. 527–534, July 2010. (see p. 20)

[112] B. C. O'Regan, S. Scully, A. C. Mayer, E. Palomares, and J. Durrant, "The effect of Al2O3 barrier layers in TiO2/dye/CuSCN photovoltaic cells explored by recombination and DOS characterization using transient photovoltage measurements.," *The journal of physical chemistry. B*, vol. 109, pp. 4616–23, Mar. 2005. (see p. 25)

[113] C. Lin, F.-Y. Tsai, M.-H. Lee, C.-H. Lee, T.-C. Tien, L.-P. Wang, and S.-Y. Tsai, "Enhanced performance of dye-sensitized solar cells by an Al2O3 charge-recombination barrier formed by low-temperature atomic layer deposition," *Journal of Materials Chemistry*, vol. 19, no. 19, p. 2999, 2009. (see p. 25)

[114] M. Vasilopoulou, D. G. Georgiadou, A. Soultati, N. Boukos, S. Gardelis, L. C. Palilis, M. Fakis, G. Skoulatakis, S. Kennou, M. Botzakaki, S. Georga, C. A. Krontiras, F. Auras, D. Fattakhova-Rohlfing, T. Bein, T. A. Papadopoulos, D. Davazoglou, and P. Argitis, "Atomic-Layer-Deposited Aluminum and Zirconium Oxides for Surface Passivation of TiO 2 in High-Efficiency Organic Photovoltaics," *Advanced Energy Materials*, pp. n/a–n/a, June 2014. (see p. 25)

[115] G. Dingemans and W. M. M. Kessels, "Status and prospects of Al2O3-based surface passivation schemes for silicon solar cells," *Journal of Vacuum Science & Technology A: Vacuum, Surfaces, and Films*, vol. 30, p. 040802, July 2012. (see p. 25)

[116] S. M. George, "Atomic layer deposition: an overview.," *Chemical reviews*, vol. 110, pp. 111–31, Jan. 2010. (see pp. 25 and 34)

[117] J. Shewchun, A. Waxman, and G. Warfield, "Tunneling in MIS structuresI," *Solid-State Electronics*, vol. 10, pp. 1165–1186, Dec. 1967. (see p. 28)

[118] A. J. White, B. D. Fainberg, and M. Galperin, "Collective Plasmon-Molecule Excitations in Nanojunctions: Quantum Consideration," *The Journal of Physical Chemistry Letters*, vol. 3, pp. 2738–2743, Oct. 2012. (see pp. 34, 48, 68, 69, 72, and 99)

[119] A. J. Leenheer, P. Narang, N. S. Lewis, and H. A. Atwater, "Solar energy conversion via hot electron internal photoemission in metallic nanostructures: Efficiency estimates," *Journal of Applied Physics*, vol. 115, p. 134301, Apr. 2014. (see pp. 34, 67, 68, 69, 70, 71, and 72)

[120] N. Kopidakis, K. Benkstein, J. van de Lagemaat, A. Frank, Q. Yuan, and E. Schiff, "Temperature dependence of the electron diffusion coefficient in electrolyte-filled TiO2 nanoparticle films: Evidence against multiple trapping in exponential

conduction-band tails," *Physical Review B*, vol. 73, p. 045326, Jan. 2006. (see p. 35)

[121] M. Shanmugam and M. F. Baroughi, "Characterization of Nanoporous TiO2 Surface Defects by Temperature Dependent Electron Transport Studies on Dye Sensitized Solar Cells," *MRS Proceedings*, vol. 1363, pp. mrss11–1363–rr05–09, Aug. 2011. (see p. 35)

[122] A. Vilan, A. Shanzer, and D. Cahen, "Molecular control over Au/GaAs diodes," *Nature*, vol. 404, pp. 166–8, Mar. 2000. (see p. 37)

[123] A. Vilan, J. Ghabboun, and D. Cahen, "Molecule - Metal Polarization at Rectifying GaAs Interfaces," pp. 6360–6376, 2003. (see pp. 37 and 39)

[124] O. Yaffe, L. Scheres, S. R. Puniredd, N. Stein, A. Biller, R. H. Lavan, H. Shpaisman, H. Zuilhof, H. Haick, D. Cahen, and A. Vilan, "Molecular electronics at metal/semiconductor junctions. Si inversion by sub-nanometer molecular films.," *Nano letters*, vol. 9, pp. 2390–4, June 2009. (see p. 37)

[125] J. Krüger, U. Bach, and M. Grätzel, "Modification of TiO2 Heterojunctions with Benzoic Acid Derivatives in Hybrid Molecular Solid-State Devices," *Advanced Materials*, vol. 12, pp. 447–451, Mar. 2000. (see pp. 37 and 38)

[126] Z. He, C. Zhong, X. Huang, W.-Y. Wong, H. Wu, L. Chen, S. Su, and Y. Cao, "Simultaneous enhancement of open-circuit voltage, short-circuit current density, and fill factor in polymer solar cells.," *Advanced materials (Deerfield Beach, Fla.)*, vol. 23, pp. 4636–43, Oct. 2011. (see p. 37)

[127] A. Tada, Y. Geng, Q. Wei, K. Hashimoto, and K. Tajima, "Tailoring organic heterojunction interfaces in bilayer polymer photovoltaic devices.," *Nature materials*, vol. 10, pp. 450–5, June 2011. (see p. 37)

[128] A. S. Erickson, N. K. Kedem, A. E. Haj-Yahia, and D. Cahen, "Aluminum oxide-Si field effect inversion layer solar cells with organic top contact," *Applied Physics Letters*, vol. 101, p. 233901, Dec. 2012. (see p. 37)

[129] L. Barnea-Nehoshtan, P. K. Nayak, A. Shu, T. Bendikov, A. Kahn, and D. Cahen, "Enhancing the tunability of the open-circuit voltage of hybrid photovoltaics with mixed molecular monolayers.," *ACS applied materials & interfaces*, vol. 6, pp. 2317–24, Mar. 2014. (see p. 37)

[130] F. P. García de Arquer, A. Mihi, D. Kufer, and G. Konstantatos, "Photoelectric energy conversion of plasmon-generated hot carriers in metal-insulator-

semiconductor structures.," *ACS nano*, vol. 7, pp. 3581–8, Apr. 2013. (see pp. 38, 42, 47, 49, and 62)

[131] B. A. Gregg, F. Pichot, S. Ferrere, and C. L. Fields, "Interfacial Recombination Processes in Dye-Sensitized Solar Cells and Methods To Passivate the Interfaces," *The Journal of Physical Chemistry B*, vol. 105, pp. 1422–1429, Feb. 2001. (see p. 38)

[132] M. Graetzel, R. A. J. Janssen, D. B. Mitzi, and E. H. Sargent, "Materials interface engineering for solution-processed photovoltaics.," *Nature*, vol. 488, pp. 304–12, Aug. 2012. (see p. 38)

[133] Q. Qu, H. Geng, R. Peng, Q. Cui, X. Gu, F. Li, and M. Wang, "Chemically binding carboxylic acids onto TiO2 nanoparticles with adjustable coverage by solvothermal strategy.," *Langmuir : the ACS journal of surfaces and colloids*, vol. 26, pp. 9539–46, June 2010. (see pp. 38 and 40)

[134] C. O'Rourke and D. R. Bowler, "DSSC anchoring groups: a surface dependent decision.," *Journal of physics. Condensed matter : an Institute of Physics journal*, vol. 26, p. 195302, May 2014. (see p. 38)

[135] M. J. Tillotson, P. M. Brett, R. A. Bennett, and R. Grau-Crespo, "Adsorption of organic molecules at the TiO2(110) surface: The effect of van der Waals interactions," *Surface Science*, vol. 632, pp. 142–153, Feb. 2015. (see p. 38)

[136] A. Vilan and D. Cahen, "Soft Contact Deposition onto Molecularly Modified GaAs. Thin Metal Film Flotation: Principles and Electrical Effects," *Advanced Functional Materials*, vol. 12, pp. 795–807, Dec. 2002. (see p. 39)

[137] B. de Boer, M. M. Frank, Y. J. Chabal, W. Jiang, E. Garfunkel, and Z. Bao, "Metallic Contact Formation for Molecular Electronics: Interactions between Vapor-Deposited Metals and Self-Assembled Monolayers of Conjugated Mono- and Dithiols," *Langmuir*, vol. 20, pp. 1539–1542, Mar. 2004. (see p. 39)

[138] H. Haick and D. Cahen, "Making contact: Connecting molecules electrically to the macroscopic world," *Progress in Surface Science*, vol. 83, pp. 217–261, June 2008. (see p. 39)

[139] Y. Jin, N. Friedman, M. Sheves, and D. Cahen, "Effect of metal-molecule contact roughness on electronic transport: bacteriorhodopsin-based, metal-insulator-metal planar junctions.," *Langmuir : the ACS journal of surfaces and colloids*, vol. 24, pp. 5622–6, May 2008. (see p. 39)

[140] S. Rühle, M. Greenshtein, S.-G. Chen, A. Merson, H. Pizem, C. S. Sukenik, D. Cahen, and A. Zaban, "Molecular adjustment of the electronic properties of nanoporous electrodes in dye-sensitized solar cells.," *The journal of physical chemistry. B*, vol. 109, pp. 18907–13, Oct. 2005. (see p. 45)

[141] C. Goh, S. R. Scully, and M. D. McGehee, "Effects of molecular interface modification in hybrid organic-inorganic photovoltaic cells," *Journal of Applied Physics*, vol. 101, p. 114503, June 2007. (see p. 45)

[142] D. B. Kokh, R. J. Buenker, and J. L. Whitten, "Trends in adsorption of open-shell atoms and small molecular fragments on the Ag(111) surface," *Surface Science*, vol. 600, pp. 5104–5113, Dec. 2006. (see p. 45)

[143] D. R. Jung, "Interactions and penetration at metal/self-assembled organic monolayer interfaces," *Journal of Vacuum Science & Technology A: Vacuum, Surfaces, and Films*, vol. 14, p. 1779, May 1996. (see p. 47)

[144] A. V. Walker, T. B. Tighe, O. M. Cabarcos, M. D. Reinard, B. C. Haynie, S. Uppili, N. Winograd, and D. L. Allara, "The dynamics of noble metal atom penetration through methoxy-terminated alkanethiolate monolayers.," *Journal of the American Chemical Society*, vol. 126, pp. 3954–63, Mar. 2004. (see p. 47)

[145] Q. Sun, A. Selloni, and G. Scoles, "Electronic structure of metal/molecule//metal junctions: a density functional theory study of the influence of the molecular terminal group.," *The journal of physical chemistry. B*, vol. 110, pp. 3493–8, Mar. 2006. (see p. 47)

[146] F. Chen, X. Li, J. Hihath, Z. Huang, and N. Tao, "Effect of anchoring groups on single-molecule conductance: comparative study of thiol-, amine-, and carboxylic-acid-terminated molecules.," *Journal of the American Chemical Society*, vol. 128, pp. 15874–81, Dec. 2006. (see p. 47)

[147] A. Salomon, T. Böcking, J. J. Gooding, and D. Cahen, "How important is the interfacial chemical bond for electron transport through alkyl chain monolayers?," *Nano letters*, vol. 6, pp. 2873–6, Dec. 2006. (see p. 47)

[148] S. Mubeen, J. Lee, W.-R. Lee, N. Singh, G. D. Stucky, and M. Moskovits, "On the plasmonic photovoltaic.," *ACS nano*, vol. 8, pp. 6066–73, June 2014. (see p. 48)

[149] P. Banerjee, D. Conklin, S. Nanayakkara, T.-H. Park, M. J. Therien, and D. a. Bonnell, "Plasmon-induced electrical conduction in molecular devices.," *ACS nano*, vol. 4, pp. 1019–25, Feb. 2010. (see p. 48)

[150] S. C. Warren, D. A. Walker, and B. A. Grzybowski, "Plasmoelectronics : coupling plasmonic excitation with electron flow Plasmoelectronics : coupling plasmonic excitation with electron flow," 2012. (see p. 48)

[151] T. Lutz, C. Grosse, C. Dette, A. Kabakchiev, F. Schramm, M. Ruben, R. Gutzler, K. Kuhnke, U. Schlickum, and K. Kern, "Molecular orbital gates for plasmon excitation.," *Nano letters*, vol. 13, pp. 2846–50, June 2013. (see p. 48)

[152] S. V. Aradhya and L. Venkataraman, "Single-molecule junctions beyond electronic transport.," *Nature nanotechnology*, vol. 8, pp. 399–410, June 2013. (see p. 48)

[153] Y. Takahashi and T. Tatsuma, "Solid state photovoltaic cells based on localized surface plasmon-induced charge separation," *Applied Physics Letters*, vol. 99, p. 182110, Nov. 2011. (see p. 49)

[154] S. Mubeen, G. Hernandez-Sosa, D. Moses, J. Lee, and M. Moskovits, "Plasmonic photosensitization of a wide band gap semiconductor: converting plasmons to charge carriers.," *Nano letters*, vol. 11, pp. 5548–52, Dec. 2011. (see p. 49)

[155] Y. Xia and G. M. Whitesides, "Soft Lithography," *Annual Review of Materials Science*, vol. 28, pp. 153–184, Aug. 1998. (see p. 50)

[156] W. L. Barnes, A. Dereux, and T. W. Ebbesen, "Surface plasmon subwavelength optics," *Nature*, vol. 424, no. August, pp. 824–830, 2003. (see p. 50)

[157] F. J. García de Abajo, "Colloquium: Light scattering by particle and hole arrays," *Reviews of Modern Physics*, vol. 79, pp. 1267–1290, Oct. 2007. (see pp. 50 and 60)

[158] T. López-Rios, D. Mendoza, F. García-Vidal, J. Sánchez-Dehesa, and B. Pannetier, "Surface Shape Resonances in Lamellar Metallic Gratings," *Physical Review Letters*, vol. 81, pp. 665–668, July 1998. (see p. 50)

[159] M. E. Stewart, N. H. Mack, V. Malyarchuk, J. A. N. T. Soares, T.-W. Lee, S. K. Gray, R. G. Nuzzo, and J. A. Rogers, "Quantitative multispectral biosensing and 1D imaging using quasi-3D plasmonic crystals.," *Proceedings of the National Academy of Sciences of the United States of America*, vol. 103, pp. 17143–8, Nov. 2006. (see p. 50)

[160] T. V. Teperik, V. V. Popov, F. J. García de Abajo, M. Abdelsalam, P. N. Bartlett, T. A. Kelf, Y. Sugawara, and J. J. Baumberg, "Strong coupling of light to flat metals via a buried nanovoid lattice: the interplay of localized and free plasmons," *Optics Express*, vol. 14, no. 5, p. 1965, 2006. (see pp. 50 and 57)

[161] T. Kelf, Y. Sugawara, R. Cole, J. Baumberg, M. Abdelsalam, S. Cintra, S. Mahajan, A. Russell, and P. Bartlett, "Localized and delocalized plasmons in metallic nanovoids," *Physical Review B*, vol. 74, p. 245415, Dec. 2006. (see pp. 50, 56, and 57)

[162] H. Zhang and A. O. Govorov, "Optical Generation of Hot Plasmonic Carriers in Metal Nanocrystals: The Effects of Shape and Field Enhancement," *The Journal of Physical Chemistry C*, vol. 118, pp. 7606–7614, Apr. 2014. (see pp. 56 and 62)

[163] A. O. Govorov, H. Zhang, and Y. K. Gunko, "Theory of Photoinjection of Hot Plasmonic Carriers from Metal Nanostructures into Semiconductors and Surface Molecules," *The Journal of Physical Chemistry C*, vol. 117, pp. 16616–16631, Aug. 2013. (see pp. 56, 59, 79, and 99)

[164] C. Berglund and W. Spicer, "Photoemission Studies of Copper and Silver: Theory," *Physical Review*, vol. 136, pp. A1030–A1044, Nov. 1964. (see p. 56)

[165] E. Hendry, F. Garcia-Vidal, L. Martin-Moreno, J. Rivas, M. Bonn, A. Hibbins, and M. Lockyear, "Optical control over surface-plasmon-polariton-assisted THz transmission through a slit aperture," *Physical review letters*, vol. 100, no. 12, p. 123901, 2008. (see p. 57)

[166] G. Vecchi, V. Giannini, and J. Gómez Rivas, "Surface modes in plasmonic crystals induced by diffractive coupling of nanoantennas," *Physical Review B*, vol. 80, p. 201401, Nov. 2009. (see p. 57)

[167] J. Lehmann, M. Merschdorf, W. Pfeiffer, A. Thon, S. Voll, and G. Gerber, "Surface Plasmon Dynamics in Silver Nanoparticles Studied by Femtosecond Time-Resolved Photoemission," *Physical Review Letters*, vol. 85, pp. 2921–2924, Oct. 2000. (see p. 66)

[168] M. A. Green, *Solar cells: operating principles, technology, and system applications*. 1982. (see pp. 69 and 74)

[169] E. Chan, H. Card, and M. Teich, "Internal photoemission mechanisms at interfaces between germanium and thin metal films," *IEEE Journal of Quantum Electronics*, vol. 16, pp. 373–381, Mar. 1980. (see p. 70)

[170] A. O. Govorov, H. Zhang, H. V. Demir, and Y. K. Gunko, "Photogeneration of hot plasmonic electrons with metal nanocrystals: Quantum description and potential applications," *Nano Today*, vol. 9, pp. 85–101, Feb. 2014. (see pp. 70 and 99)

[171] S. M. Sze, *Physics of Semiconductor Devices*. John Wiley & Sons, 2nd ed., 1981. (see pp. 74 and 93)

[172] M. T. Greiner, M. G. Helander, W.-M. Tang, Z.-B. Wang, J. Qiu, and Z.-H. Lu, "Universal energy-level alignment of molecules on metal oxides.," *Nature materials*, vol. 11, pp. 76–81, Jan. 2012. (see p. 76)

[173] G. Konstantatos, I. Howard, A. Fischer, S. Hoogland, J. Clifford, E. Klem, L. Levina, and E. H. Sargent, "Ultrasensitive solution-cast quantum dot photodetectors.," *Nature*, vol. 442, pp. 180–3, July 2006. (see p. 77)

[174] *Handbook of Optoelectronics (Two-Volume Set)*. CRC Press, 2010. (see p. 77)

[175] L. Du, A. Furube, K. Yamamoto, K. Hara, R. Katoh, and M. Tachiya, "Plasmon-Induced Charge Separation and Recombination Dynamics in GoldTiO 2 Nanoparticle Systems: Dependence on TiO 2 Particle Size," *The Journal of Physical Chemistry C*, vol. 113, pp. 6454–6462, Apr. 2009. (see p. 79)

[176] A. V. Uskov, I. E. Protsenko, R. S. Ikhsanov, V. E. Babicheva, S. V. Zhukovsky, A. V. Lavrinenko, E. P. OReilly, and H. Xu, "Photoelectron emission from plasmonic nanoparticles: Comparison between surface and volume photoelectric effects," p. 13, Dec. 2013. (see pp. 79 and 99)

[177] A. Rogalski, "HgCdTe infrared detector material: history, status and outlook," *Reports on Progress in Physics*, vol. 68, pp. 2267–2336, Oct. 2005. (see p. 80)

[178] P. Babula, V. Adam, R. Opatrilova, J. Zehnalek, L. Havel, and R. Kizek, "Uncommon heavy metals, metalloids and their plant toxicity: a review," *Environmental Chemistry Letters*, vol. 6, pp. 189–213, June 2008. (see p. 80)

[179] V. E. Henrich and P. A. Cox, *The Surface Science of Metal Oxides*. 1996. (see p. 80)

[180] S. T. Kochuveedu, Y. H. Jang, and D. H. Kim, "A study on the mechanism for the interaction of light with noble metal-metal oxide semiconductor nanostructures for various photophysical applications.," *Chemical Society reviews*, vol. 42, pp. 8467–93, Nov. 2013. (see p. 80)

[181] P. B. Johnson and R. W. Christy, "Optical Constants of the Noble Metals," *Physical Review B*, vol. 6, pp. 4370–4379, Dec. 1972. (see p. 88)

[182] H. A. Bethe and M. I. o. T. R. Laboratory, *Theory of the Boundary Layer of Crystal Rectifiers*. 1942. (see p. 95)